Measuring di-electron Dalitz decays of baryon resonances with HADES and PANDA

Author: Mgr Inż. Jacek Biernat

Promotor: Prof. Piotr Salabura

Co-promotor: Dr Witold Przygoda

A doctoral dissertation written in the Nuclear Physics Institute, Jagiellonian University Cracow

JAGIELLONIAN UNIVERSITY IN CRACOW
Marian Smoluchowski Institute of Physics

Abstract

Dielectron production in nucleon-nucleon collisions at kinetic beam energies below the η meson production threshold offers a unique possibility to study the bremsstrahlung radiation with time-like virtual photons. The relevant final state is the NN $\gamma*(e^+e^-)$ resulting from the interaction between the nucleons or/and their excited states (for example Δ) formed in the collisions. The production amplitude of virtual photon depends on a structure of electromagnetic form-factors of a nucleons and excited baryon resonances, which for energies 1-2 GeV is strongly influenced by the light vector mesons. In general, a virtual photon radiation is described by a coherent sum of two types of amplitudes with or without a resonance excitation. Excited resonances undergo further decays, in particular via the Dalitz decay ($R \rightarrow Ne^+e^-$) process. It is complementary to the studies of nucleon electromagnetic form-factor in a positron-electron annihilation and the Δ transition form-factor studied by means of pion photo-production. The first part of the thesis is devoted to the investigation of a di-electron pair production in quasi-free np interactions using deuterium beam on proton target at a kinetic energy of 1.25 GeV/u. Detection of a spectator proton from the deuterium break-up at forward angles ($0.3^\circ < \theta < 7^\circ$) and an electron-positron pairs and a proton in the High Acceptance Dielectron Spectrometer (HADES) allows for a detailed analysis of the e^+e^- pair production in the $np \rightarrow npe^+e^-$ reaction. A discussion on the available model predictions, in particular interpretations of a striking excess of the e^+e^- pair production in comparison to pp data is given.

In the second part a proposal of measurement of the electromagnetic hyperon decays (Hyperon $\rightarrow \Lambda e^+e^-$) for the future experiment PANDA@GSI is discussed on the example of the Λ(1520) Dalitz decay into $\Lambda^0 e^+e^-$. Studying the signal from this channel gives a possibility of probing the eTFF (electromagnetic transistion form-factors) which carry information about the hadron structure. The main focus of the analysis is to present details of a simulation of the Λ(1520) Dalitz decay produced in $\bar{p} - p$ collision at the beam momentum 4 GeV/c, its reconstruction and detection in the PANDA detector and finally an estimation of the production rate and signal to background rate. The results are compared with the Monte-Carlo simulations done for the future measurements of pp collisions by means of HADES. Last but not least, the performance of the planned Forward Tracker (FT) emphasizing its role in the future measurements of the states above the open charm threshold and hyperon spectroscopy is presented.

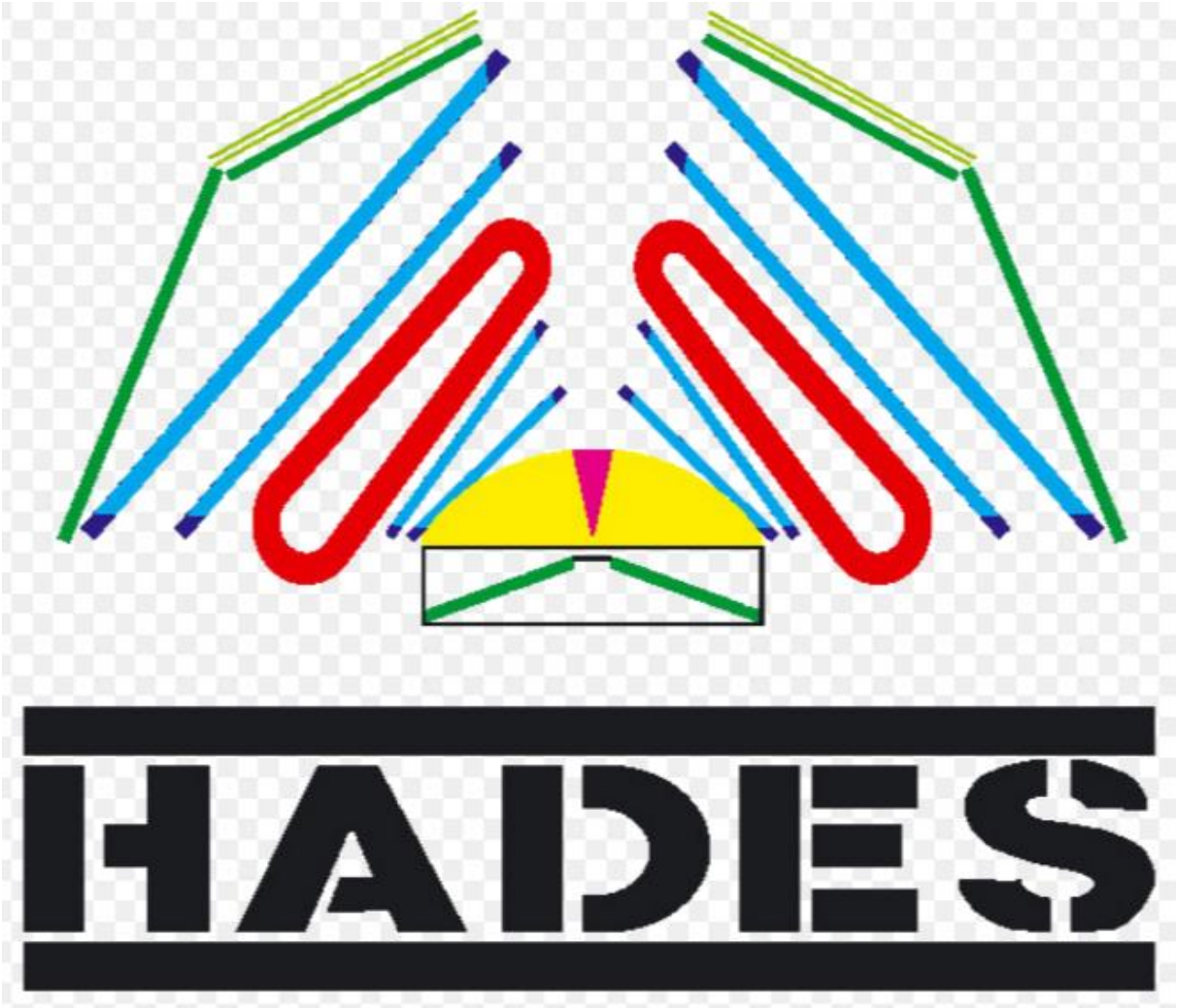
HADES

1. Introduction

1.1 Electromagnetic decays of hadrons and sources of e^+ e^- pairs in nucleon-nucleon reactions

In the last years there is an increased interest in electromagnetic decays of hadrons, which play an important role in modern hadron physics. The progress in experimental techniques has made possible to carry out experiments that were proposed long time ago but could not be carried out due to a low probability of the process and difficulties associated with a high hadronic background level. The progress in theoretical description of Quantum Chromo Dynamics (QCD) on lattice and the fundamental question of the origin of confinement have turned the physics of hard and soft processes, probing the hadron structure at small and large distances, into an interesting point of discussion. It became obvious that the first task is to find a number of important phenomenological characteristics of hadrons such as: magnetic moments, electromagnetic transition form-factors (a point addressed in this thesis), structure of the mass spectrum and the existence of exotic states outside the naive quark model, like hybrid states containing quark and gluon combinations in their wave functions and so on. Particularly interesting are electromagnetic processes like meson production in positron-electron annihilation, meson decays into leptons and/or photons probing hadron- photon interactions hence revealing the distribution of charge in hadron.

The recent measurements of g-2 for a muon indicate a significant deviations from the predictions of perturbative QED which might indicate some physics beyond the standard model. Higher order hadronic corrections, like vacuum polarization and "so called" light-by-light, call for more precise data on meson production in positron-electron annihilation and on meson transition form-factors (for recent review see [1, 2]) .

Dielectron decays of hadrons are also an essential reference for studies of the virtual photon radiation from hot and dense nuclear matter produced in heavy ion (HI) collisions. Unlike the hadron spectra dileptons are not affected by the strong final state interactions and hence carry undisturbed information from the hot and dense collisions zone. In a similar manner, as a black body radiation a thermalized fireball created in the HI collisions radiates photons, real and a virtual ones, where the latter convert to dileptons. As shown by several experiments, [3] a slope of the invariant mass spectrum of dileptons at high masses (> 1.5 GeV/c^2) is a measure of the temperature reached in collisions while the low mass spectrum (<1 GeV/c^2) is dominated by decays of the ρ meson with a mass distribution significantly modified by a surrounding medium. In order to extract the precise shape of the latter one a subtraction of the hadron decays from the late stage of the collision (so called freeze-out) is required. It appears that the most important sources of such decays are Dalitz decays of baryons and mesons which will be described in more details below.

1.2 Electromagnetic form-factors

A typical approach of probing the electromagnetic structure of composite objects was performed by Rutherford in which the structure of atoms was analyzed and the atomic nucleus was discovered. The method is based on the scattering of a charged particle, "so called probe", in the electromagnetic field of the target. In modern day experiments a good example of such an approach are experiments measuring scattering of electrons and muons on a nucleon.

The differential cross-section as a function of the four momentum transfer (q^2) for the scattering of an electron on a particle with an internal structure can be described in general form as given below:

$$\frac{d\sigma}{dq^2} = [\frac{d\sigma}{dq^2}]_{point\ like}[F(q^2)]^2 \qquad (1)$$

The point like term stands for a description of an point-like object with a given spin and parity, the term $[F(q^2)]^2$ represents a form-factor, which in general can be a complex quantity, also depending on the spin and the parity. The function represents the structure of a given object (charge distribution etc.) and can be obtained by comparing data to theoretical predictions for a "point-like" object. Fourier transformation of the $F(q^2)$ gives charge distribution inside the particle and the first derivate at $q^2 = 0$, the radius of particle.

A more general concept of the form-factor is presented in **Fig 1.1** by means of Feynman diagrams for the case of charged pion. There are two kinematical regimes defined by the sign of the q^2 of the virtual photon exchanged in a reaction: a space-like (negative) (left) and a time like (positive)(right). The reactions inducing photon exchange of the respective type are electro-scattering and annihilation.

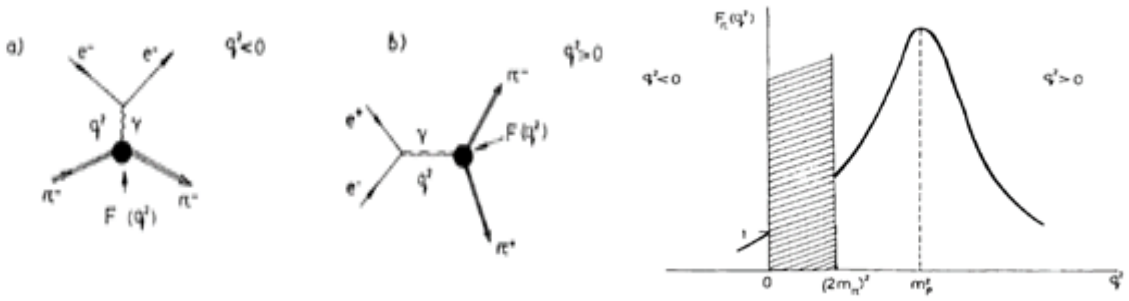

Fig 1.1 a) Diagram showing e^- scattering on a pion , the process is dominated by one photon exchange in the space like region (four momentum transfer $q^2 < 0$) the differential cross section of the scattering is modified by the pion form-factor. b) $e^+e^- \rightarrow \pi^+\pi^-$ annihilation is mediated by one photon in the time like region ($q^2 < 0$), again the differential cross section is modified by the pion form-factor. c) Distribution of the form-factor $F(q^2)$ in the whole physical accessible region of q^2. The dashed area represents a domain which is kinematically forbidden. Figure taken from [4].

Another famous example of the above studies in the space–like region is an electron (or muon) scattering by the proton or the neutron. It appears that important are not only the

involved charges but also the spins and the (related to it) magnetic moments of the interacting particles. At large values of the four momentum transfer the respective degrees of freedom are quarks but al lower ($q^2 < 1$ GeV/c^2) besides quark core also meson cloud surrounding nucleon plays a role [5]. A general description of the electromagnetic structure of protons or neutrons requires two different form-factors, electric and magnetic. It is important to state that form-factors contain, a complete information on the electromagnetic structure of a particle.

Electron- hadron scattering is not the only source of the virtual photon used for probing of the hadron structure. Another possibility, already mentioned above and presented in **Fig 1.1** b), is the annihilation of a e^+e^- pair. It produces a virtual massive photon decaying mainly into an even or odd number of $\pi^+ \pi^-$ pairs (for the proton form-factor the respective simplest final state would be proton-antiproton pair). The virtual photon transfers energy, hence has $q^2 > 0$. In this region one encounters yet another interesting effect: interaction between photons and hadrons is strongly influenced by a presence of hadron resonances having same quantum numbers as photon, vector mesons. This phenomenon also referred as Vector-Meson Dominance (VMD) [6] states that short lived neutral mesons, with the same quantum numbers as a photon, carry the interaction between hadron and the photon, as shown in **Fig 1.2** for the case of the charged pion production. The lightest are ρ^0 (769 MeV/c^2) , ω (783 MeV/c^2) and φ (1020 MeV/c^2). This effect is especially visible in the time like region when the q^2 reaches the squared mas of the vector meson. The meson becomes "real" and decays afterwards. **Fig 1.2** shows the respective form-factor for the charged pion which is dominated by the ρ meson.

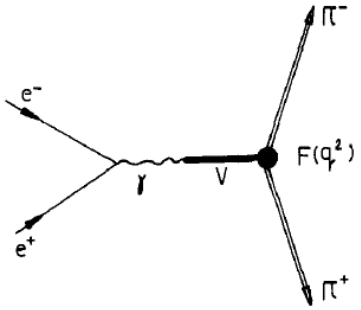

Fig 1.2 One photon exchange represented in the VMD approach. Figure taken from [4].

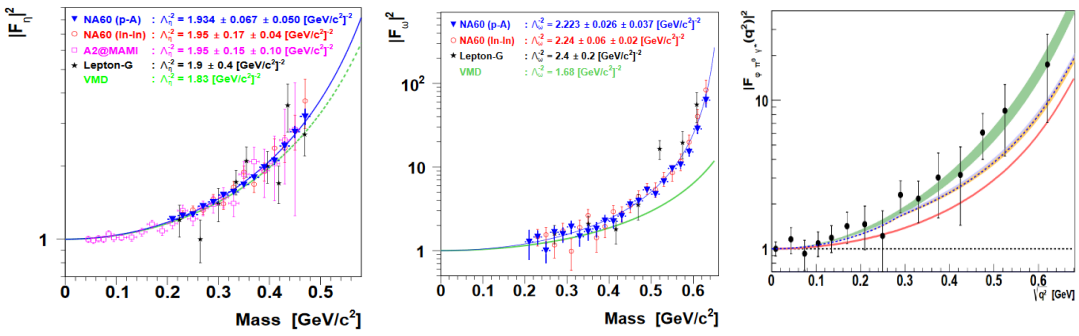

Fig 1.3 The dots represent the experimental data for $\eta \rightarrow \gamma e^+e^-$ (left), $\omega \rightarrow \pi^0 e^+e^-$ (middle) and $\varphi \rightarrow \pi^0 e^+e^-$ (right) transition form-factor compared to one pole VMD approach (green curvess in the left, middle plots and red solid in the right panel). In the right plot also calculations, with chiral theory approach (green curve) and dispersive analysis (orange, cyan bands and blue dashed) are shown. Plots are taken from [1, 2].

Yet, there is another process where electromagnetic form-factors play an essential role. This is so called Dalitz decay, with general scheme $A \rightarrow B\ l^+\ l^-$, where the hadron (A) radiates a virtual massive photon converting to a lepton pair (l^+, l^-) and a real photon or another hadron (B). A very well know example of such decay are for example $\pi^0, \eta \rightarrow \gamma e^+ e^-$.

The "l" denotes in general electron or muon decays and the respective differential decay width can be written in analogy to (1) as follows:

$$\frac{d\Gamma}{dq^2} = [\frac{d\Gamma}{dq^2}]_{point\ like}[F(q^2)]^2 \qquad (2)$$

where the $[\frac{d\Gamma}{dq^2}]_{point-like}$ can be calculated precisely from QED (see for example [7]) and $F(q^2)$ is in this case electromagnetic transition form-factor. Such decays have been measured over last years with excellent precision for some light mesons, as shown in **Fig 1.3**. In the range of small momentum transfer the transition form-factor (A → B) can be written as presented below, the expression comes from [4]:

$$F_{AB}(q^2) \cong 1 + q^2 \left[\frac{dF_{AB}}{dq^2}\right]_{q^2=0} = 1 + q^{AB} b_{AB} = 1 + \frac{1}{6} q^2 < r_{AB}^2 > \qquad (3)$$

r_{AB} – characteristic size depended on the region of A to B transition.
b_{AB} – slope parameter of a transition form-factor.

where the slope parameter is connected to the corresponding meson and its value can be obtained from a fit to experimental data.

In general the form-factor can be parametrized as a so called pole approximation.

$$F_{AB}(q^2) = [\ 1 - \ q^2/\Lambda^2\ ]^{-1} \qquad (4)$$

where Λ is the characteristic mass $\Lambda \cong (\Lambda^{-2} = b_{AB})$ and is given in [4] for various mesons. The experimentally obtained effective mass values are presented below in **Table 1** for π^0,ω,η, ϕ [1, 2, 4] and η` Dalitz decay. **Fig 1.3** shows results from the respective fits with formula 4 to the data together with predictions of VDM assuming only one pole. For the η meson the obtained parameter is very close to the VDM with a single pole but in the case of ω is quite far from the data points. This has been addressed in [2] as a possible ρ/ω interference due to the common production mechanism, the authors state that the analysis has "ruled out interference scenarios other than completely constructive or destructive".

Meson	$F(q^2)$	$b = \Lambda^{-2}$
η	$F(q^2; 0; m_\eta^2) = (1 - \ q^2 b_\eta\ )^{-1}$	1.934(0.067) GeV^{-2}
η`	Similar	1.7(0.4) GeV^{-2}
ω	Similar	2.22(0.02) GeV^{-2}
π^0	$F(q^2; 0; m_\pi^2) = 1 + b_{\pi^0} q^2$	1.63(0.01) GeV^{-2}
φ	$F(q^2) = 1/(1 - q^2 b^{-1/2})$	2.02(0.11) GeV^{-2}

Table 1. Selected calculations obtained from experimental results [1, 2, 4, 94].

1.2 Baryon electromagnetic decays

The investigation of baryon resonances (R) decays into a nucleon and a massive "virtual" photon (γ*) via Dalitz gives a chance to study the structure of the resonance in the time-like region. However, in contrast to the mesons no data on the electromagnetic transition Form-Factors in this kinematical region exist so far. However, due to large width of the resonances separation of the individual contributions is difficult [8]. More advantageous are recently investigated pion induced reactions where resonance excitation can be controlled by the available energy in the pion-nucleon system.

The schematic picture illustrating expected behavior of electromagnetic transition form-factor (eTFF) for baryon resonances in various kinematical regions is presented in **Fig 1.4**

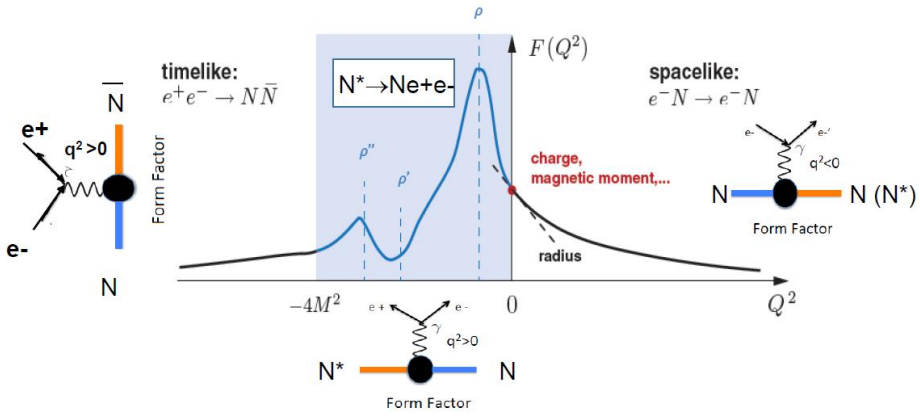

Fig 1.4 A schematic dependence of the form-factor in a function of Q^2 (= $-q^2$) for the space like and time like regions for a nucleon excited state (N*). [9]

Let's take as an example the case of Δ (1232). In $q^2 < 0$ eTFF have been obtained in the space-like region in measurements of the pion production on nucleon using electron and photon beams. In this case ($\Delta(3/2^+) \to N(1/2^+)$) the process is dominated by magnetic transitions and at $q^2 = 0$ the magnetic eTFF (G_M) can be fixed from the real photon decay of the resonance. Comparison of the data to different calculations allows to estimate contributions originating from a quark core and a pion cloud and explains in more details nature of the resonances [13]. For example **Fig 1.5** shows the q^2 dependence of the G_M for the Δ(1232) , normalized to 3 G_M ($q^2 = 0$), obtained from world data [10, 11]. As one can see, at low q^2 around 30% of the G_M is due to the pion cloud and the quark core (dotted curve) contribution dominates at $q^2 > 1$ GeV/c.

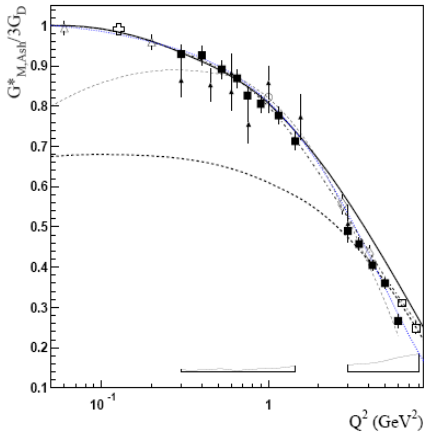

Fig 1.5 Experimental points representing the N → Δ transition displayed in Ash convention, normalized to dipole form. The solid and the dotted curves represent the quark and combined quark core and meson baryon cloud contribution. Figure taken from [12].

The Dalitz decays of baryonic resonances are basically unknown though many theoretical calculations predict a sensitivity of the dilepton invariant mass distributions to the resonance properties, particularly resonance-vector meson couplings [14]. The figure of merit is the differential decay width given as a function of the dielectron invariant mass, shown in **Fig 1.7**. It is given by:

$$\frac{d\Gamma^{\Delta\to Ne^+e^-}_{m_\Delta}}{dm_{ee}}(m_{ee}) = \frac{2\alpha}{3\pi m_{ee}}\Gamma^{\Delta\to N\gamma^*}_{m_\Delta}(m_{\gamma^*}\equiv m_{ee}).$$

$$\begin{aligned}\Gamma^{\Delta\to N\gamma^*}_{m_\Delta}(m_{\gamma^*}) &= \left(G^{\Delta\to N\gamma^*}_{m_\Delta}(m_{\gamma^*})\right)^2 \\ &\quad\times\frac{\alpha}{16}\frac{(m_\Delta+m_N)^2}{m_\Delta^3 m_N^2}\sqrt{y_+ y_-^3}, \\ y_\pm &= (m_\Delta \pm m_N)^2 - m_{ee}^2, \end{aligned} \qquad (5)$$

$$\begin{aligned}\left(G^{\Delta\to N\gamma^*}_{m_\Delta}(m_{\gamma^*})\right)^2 &= \left|G_M^2(m_{\gamma^*})\right| + 3\left|G_E^2(m_{\gamma^*})\right| \\ &\quad+\frac{m_{\gamma^*}^2}{2m_\Delta^2}\left|G_C^2(m_{\gamma^*})\right|\end{aligned}$$

where:
m_{ee} - lepton pair invariant mass.
m_Δ - static resonant mass at its pole.
α - fine structure constant.
G_M, G_E, G_C - are magnetic, electric and Coulomb transition form-factors for the Δ →N.

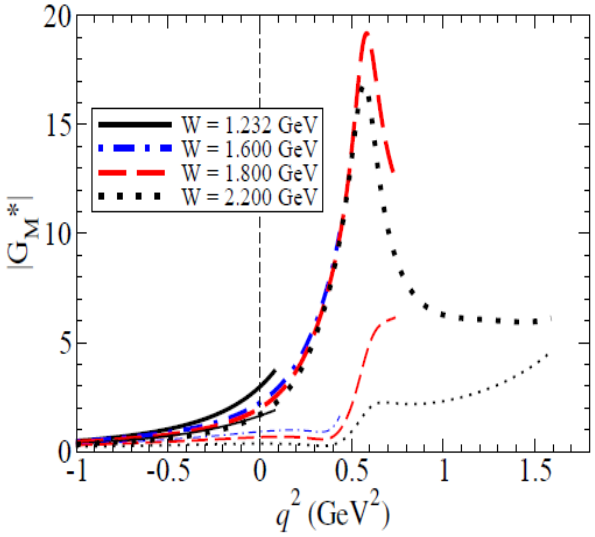

Fig 1.6 Calculations of $G_{M^*}(W)$, for different W (resonance mass) values, thick curves stand for the total result, thin curves denotes the core contributions for the respective resonance [14].

According to the Vector Meson Dominance (VMD), introduced in 60'es by Sakurai [6], the virtual photon coupling to a hadron is mediated entirely by intermediate vector mesons ρ/ω/φ. It is therefore expected that the contribution of the intermediate mesons state to the interaction modifies the q^2 dependence of the respective eTFF and produces enhancement close the vector meson poles (as shown schematically in **Fig 1.4**). Indeed, model calculations corroborates such picture.

Fig 1.6 shows the results of the covariant spectator quark model with and added pion cloud contribution. The various curves show the magnetic eTFF (G_M) dependence on the q^2 for different masses of the resonance. The pion cloud contribution is displayed separately (see figure caption) and shows enhancement around the ρ-meson pole.

Only very recently HADES has measured the decay in the proton-proton reactions at various energies. **Fig 1.7** (left) presents differential cross section of dielectron production in a function of the lepton invariant mass for experimental data obtained from $pp \rightarrow e^+e^-X$ inclusive channel (black dots) overlapped with calculations including mesonic and baryonic sources [14]. The latter are dominated by the Δ Dalitz contribution which has been calculated for two cases: "QED" (a point-like transition) and eTFF calculated with the spectator covariant model [14]("Δ Ramalho"). In **Fig 1.7** right the data from the same experiment but for the exclusive $pp \rightarrow pp e^+e^-$ channel are plotted (black dots) in comparison to the calculations: the blue curve is the sum of π^0 and Δ Dalitz with the eTFF discussed above. The non-resonant component of bremsstrahlung is shown by green curve, while the cyan curve is the Δ QED Dalitz decay. The black and red dashed curve show the quark core and the pion cloud contributions normalized to the same total yield. The inset shows the pe^+e^- missing mass and black horizontal lines represent the window chosen to select the exclusive final state. The data are well described by the calculations confirming (for the first time) experimental sensitivity to the baryon resonance Dalitz decay. As one can see the effect of the mass dependence of eTFF is rather small at this energy since the invariant mass of a virtual photon is far away from the pole of the vector meson. Higher energy data are needed to populate the region of higher invariant mass. This will be presented in the next section.

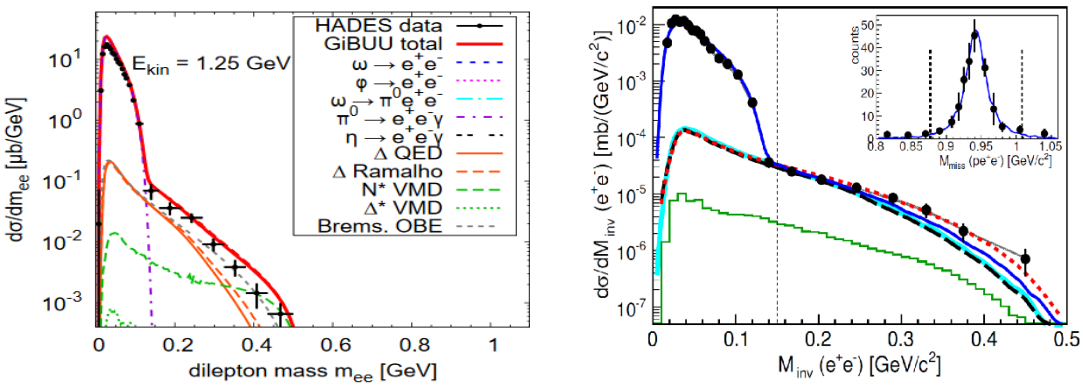

Fig 1.7 (left) Inclusive differential cross section for pp→ e^+ e^- X measured at 1.25 GeV compared to dielectron cocktail accounting for meson and baryon decays [14] (right). The same but for the exclusive pp→ ppe^+e^- compared to various sources: blue curve is the sum of π^0 and Δ Dalitz decay [14] and nucleon-nucleon bremsstrahlung (denoted as green). The cyan curve accounts for the Δ Dalitz decay assuming a point-like source; the black and red dashed curves show the quark core and the pion cloud contributions, respectively. The inset shows the pe^+e^- missing mass and black horizontal lines represent the selection window.

1.3 Dielectron production in pp collisions at beam energies above the vector meson production threshold

Two experiments focused on vector mesons production in proton-proton collisions were performed by HADES with the kinetic beam energy of 2.2 GeV and 3.5 GeV [18, 15]. Analysis of the data shows (see **Fig 1.8**) that the sources of e^+ e^- pairs mostly relate to the Dalitz decays of mesons π^0 →e^+e^- γ, η →e^+e^- γ, a two body vector meson (ρ/ω) decays at higher invariant masses. The contribution of Δ Dalitz (Ne^+e^-) decay, assuming a point-like transition vertex ("QED"-like), is expected to be small.

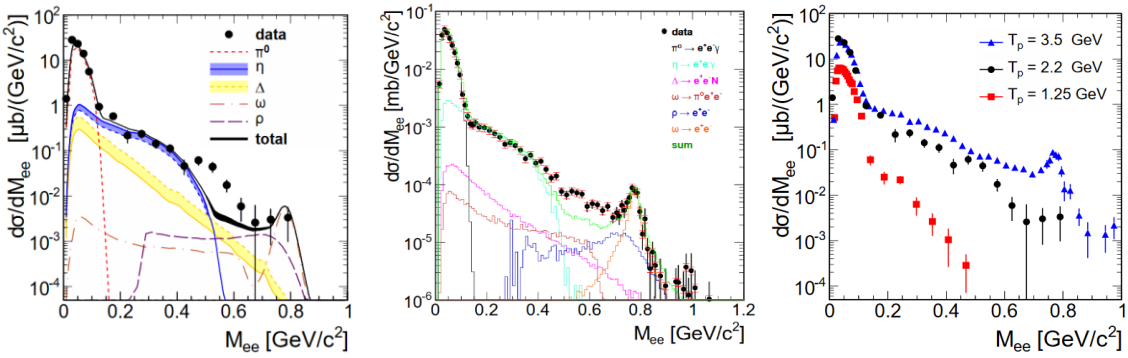

Fig 1.8 Differential cross section in a function of the invariant mass of lepton pairs, data points are presented with black dots. Starting from the left, data for 2.2 GeV compared with calculations of pair sources (decays of π^0, η, Δ, ω, ρ represented with color curves) the black curve is the incoherent sum of all contributions, second plot is the data set for the 3.5 GeV overplayed with simulated predictions, third plot (right) is a set of experimental data obtained for different energies, red squares represent data collected at 1.25 GeV, black dots correspond to 2.2 GeV data set, blue triangles stand for 3.5 GeV data [18, 15]. One should note that calculations were based on the know cross sections of the hadron production and take into account known decay branches for the meson decays.

The spectra show excess of e^+ e^- pair yield above the calculations below the vector meson pole for both energies (left and the middle panel). Comparison to the lowest beam energy (1.25 GeV-the right panel) shows very strong increase of the dielectron production in the vector meson mass region signaling importance of the vector meson contribution.

More detailed studies were done for the exclusive channel ppe^+e^- and the exclusive one pion production. The pion data allowed for more precise estimate of the baryon resonance contributions [19]. It appears that, besides Δ(1232), also higher mass resonance, particularly N(1520) contributes strongly to the pair production and may explain the excess visible in **Fig 1.9** if strong coupling to the ρ meson is taken into account.

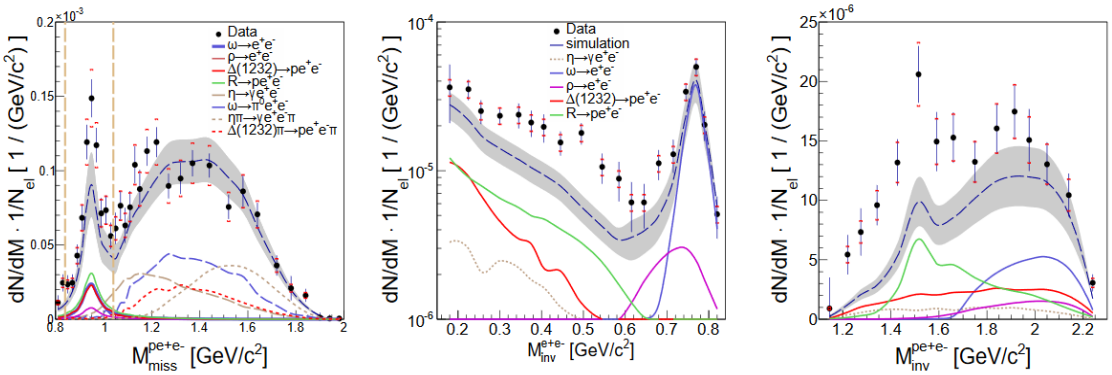

Fig 1.9 ppe^+e^- final state for pp @ 3.5 GeV. Starting from the left pe^+e^- missing mass, e^+e^- invariant mass and pe^+e^- invariant mass spectra compared with model predictions. Contributions of mesonic and baryonic decays into leptons are included. R stands for the resonance decay with a point-like $RN\gamma^*$ coupling (see section 5.1 in [19]).

Important point which has to be addressed here is that decay processes such as $R \rightarrow Ne^+e^-$ (Dalitz decay) and $R \rightarrow N\,\rho(\rightarrow e^+e^-)$ (assuming decay through the intermediate vector meson) should not in principle be treated as a two separate decay channels but treated in a coherent way. A natural connection should be established by a structure of the eTFF and particularly its dependence on the virtual photon (or e^+e^-) mass. However, in the calculations discussed above the Δ resonance was treated as decay of a point-like object, while the decays of N(1520) (and also other contributing higher mass resonances) were factorized as the two-step process, because of lack of precise predictions. Calculations performed within the framework of the extended Vector Meson Dominance (eVMD) model [6] show the contribution of the vector mesons in such transitions for some resonances. New precise data from proton and in especially pion induced reactions, as recently provide by HADES [8] are crucial to provide more constraints for calculations.

1.3.1 Dielectron production in NN collisions below vector meson production threshold

Production of e^+e^- at this energy region is related to the contribution of baryonic decays [20]: Dalitz decays of nucleon resonances $R \rightarrow Ne^+e^-$ (mainly $\Delta(1232)$), nucleon-nucleon bremsstrahlung, and extensively rising excitation function of the η meson production [21]. The baryonic sources completely saturate the e^+e^- invariant mass distribution above the π^0 mass at beam energies below η meson production threshold ($E_{thr\ beam}$= 1.257 GeV). The vector meson production is small because of the high production threshold ($E_{thr\ beam}$ = 1.88 GeV for ω) and adds some contribution, mainly from ρ, to the invariant mass at $M_{e+e-} > 0.6$ GeV/c^2. While the exclusive ω and η production in pp reactions close to the threshold is very well known, the data on ρ are scarce. It is important to notice that in contrast to the ω production a strong coupling of the ρ meson to the baryonic resonances is known , as discussed above, and has to be taken into account [22]). Moreover, since the ρ meson has a broad distribution (Γ≅150 MeV) its mass distribution is significantly modified by the resonance couplings as compared to a Breit-Wigner distribution.

Yet another interesting feature of the di-electron production in NN reactions in this energy range is a strong isospin dependence. This was already proven by the DLS experiment [24] measuring excitation functions of the pair production in pp and dp collisions in the beam energy range E_{beam} = 1 - 4 GeV and indicating very different pair production in np as compared to pp reactions at $E_{beam} < 2$ GeV. This point is addressed in more details below.

1.3.2 Inclusive dielectron production in quasi free np reactions

Studying the $n - p \rightarrow X\ e^+\ e^-$ reactions presents a challenge, since there is no capability to produce a pure neutron beam at SIS synchrotron in GSI. To solve this problem a deuteron beam et E_{kin} = 2.5 GeV was used. A forward going proton form deuterium break-up was tagged in the Froward Wall detector [25]. The deuterium itself consist of one neutron and one proton bound by the nuclear force. Even if deuterium is at rest both of the components move inside, with opposite momentum vectors, and continuously changing its directions. The distribution of the nucleon inside deuterium is known from the deuteron wave function and is presented in **Fig 1.10**.

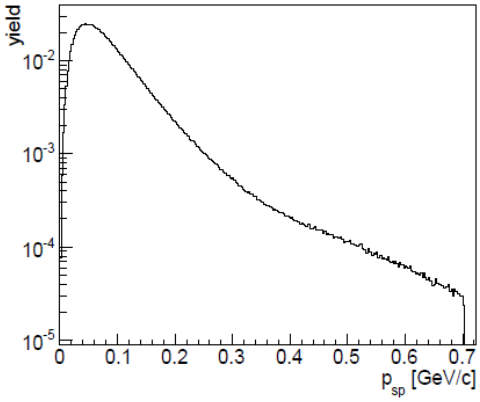

Fig 1.10 Momentum distribution of the nucleons in the deuterium according to the Paris potential [26].

Since the neutron in deuterium is not at rest, but moves with the relative momentum inside deuterium, the total energy $\sqrt{s}$ in the quasi-free proton-neutron reaction also varies from event to event. Due to small binding energy of the deuterium (binding energy = 2.2 MeV), neutron struck by the incoming proton may be treated as almost free particle in a very good approximation (in fact it is off-shell and its energy can be calculated from energy and momentum conservation). This is the assumption of spectator model which states that dp collisions can be approximated as a superposition of quasi-free pn and pp collisions, where the other nucleon in the deuterium is on its mass shell and does not take part in the reaction.

The spectator model was verified by several experiments. For example COSY-TOF confirmed the validity of this approach using $dp \rightarrow p_{spec}p\pi^-$ reaction at p_d = 1.85GeV/c [27] and COSY-11 or WASA@CELCIUS using $pd \rightarrow n_{spec}pp\eta$ [29]. In these experiments all charged particles were detected which allowed for the full event reconstruction. Therefore, the distribution of relative momentum of nucleon inside deuterium could be obtained and compared to the model expectations.

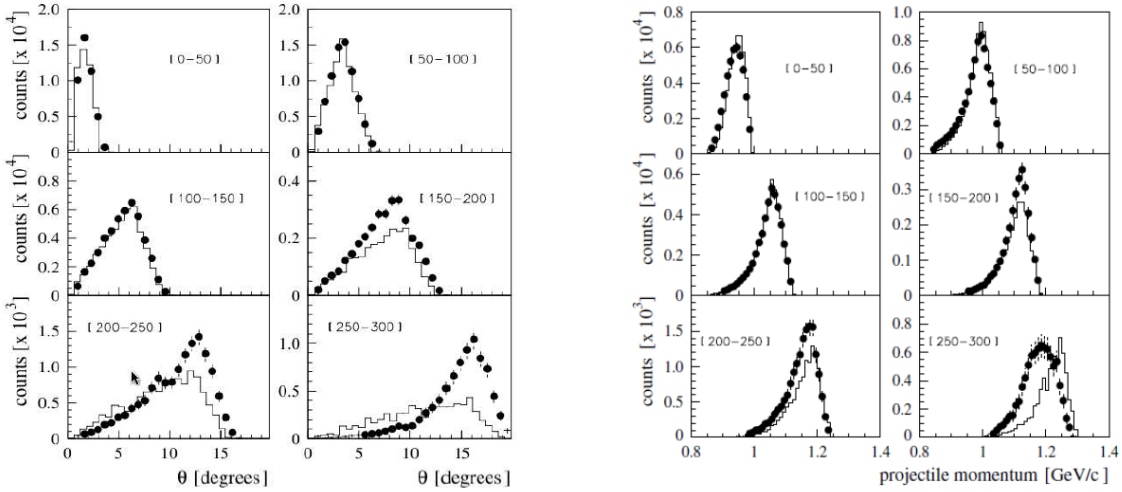

Fig 1.11 Experimentally obtained angular distribution of the spectator proton in the laboratory frame (left) and neutron momenta (right) for indicated relative momentum inside deuterium (given in MeV/c) in comparison with Monte-Carlo simulation [25].

Looking into details, the θ emission angle (left) and momentum of the projectile (right) for different invariant mass bins presented in **Fig 1.11** one can state that the spectator model describes the experimental data up to the spectator momentum of 200 MeV/c, enough to state that the model indeed works well within this momentum range.

Yet another example of validation of the model is measurement of the $p + d \rightarrow n_{spect}pp\eta$ performed by WASA/PROMICE experiment at the CELSIUS storage ring [28]. A proton beam with a kinetic energy of E_k = 1350 MeV was collided with deuterium target.
A η particle was identified by its decay into two photons, as presented in details in [29]. The total cross section for the quasi-free of $p + d \rightarrow n_{spect}pp\eta$ collisions agrees with the one measured in free pp, as presented in **Fig 1.12**.

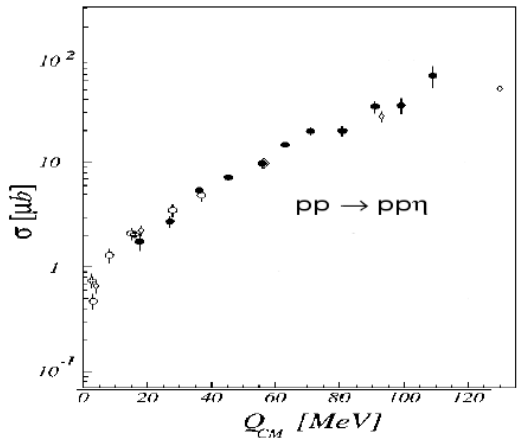

Fig 1.12 Total cross section for the quasi-free (filled circles) dp → n_{spect}ppη and free pp → ηpp (open circles) as a function of excess energy [29].

Presented above results confirm that it is possible to study neutron induced reaction with deuterium beams within the spectator model approach. This technique was applied in the HADES experiment and provided the first measurement of the inclusive dielectron production in quasi-free collisions, which we compare below to in the pp collisions.

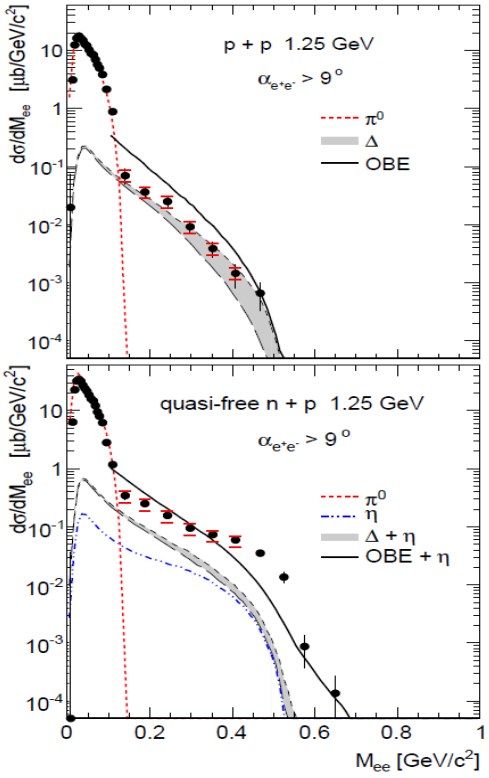

Fig 1.13 Distributions of differential cross section of e^+e^- pair in a function of the invariant mass at beam kinetic energy of 1.25 GeV. In the upper plot experimental data points for the pp collisions can be explained by a simple cocktail including π^0 and Δ Dalitz decays. Solid black curve represent contributions given by the One Boson Exchange model [30]. In the lower (np data) plot an additional contribution coming from η decay has been added.

Fig 1.13 shows inclusive invariant mass distribution of the dielectron pairs measured in pp collisions at beam kinetic energy of 1.25 GeV. The experimental points can be explained by a sum of two sources originating from the Δ(1232) and π^0 Dalitz decays assuming that the pion production is dominated by the resonance excitation. Other result has been obtained by the microscopic calculations [30] using One Boson Exchange (OBE) approach **Fig 1.13** (upper panel). In this calculations the dielectron yield above the pion mass is given as a coherent sum of various diagrams of nucleon-nucleon bremsstrahlung. In the calculations two classes of diagrams are considered: nucleon-nucleon bremsstrahlung and the graphs to intermediate Δ(1232) formation. The calculations of Kaptari and Kaempfer model overestimate measured cross sections. However, using the similar framework different, Shyam and Mosel calculations [31] predict smaller cross sections (see **Fig 1.14**, upper panel) and describe the data well. Though both works are based on the same effective Lagrangian, they differ in details and particularly implementation of the gauge invariance in diagrams with photon emission from internal exchange lines [31].

For the np case similar contributions are considered together with the η contribution which has been added due to the availability of additional energy emerging from the nucleon momentum distribution inside deuterium. However, in this case, as can be seen from **Fig 1.13** and **Fig 1.14**, both calculations do not describe the high mass region.

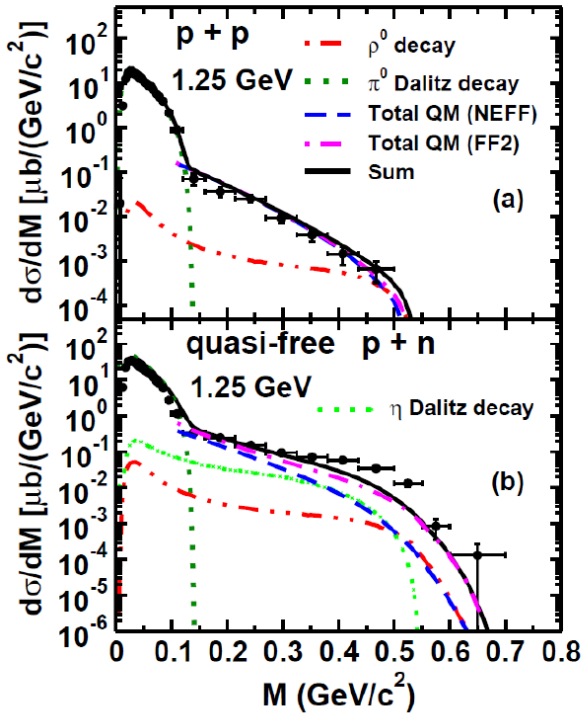

Fig 1.14 Experimental data points compared to the OBE model [31]. Results without (NEFF) and with (FF2) implementation of the electromagnetic form-factor of charged pions are shown. Solid curves show the sum of these contributions with the subthreshold ρ meson production.

One should however note that results of [31] (dashed dotted) comes closer to the HADES experimental data set. The very different shape of the np data is better explained due to the introduction of the electromagnetic form-factor of the charged pion enhancing contribution from the meson exchange line. This contribution is possible since, in contrast to the pp

reaction, diagrams with charged pion exchange contribute to the npe^+e^- final state. The calculations demonstrates a significant enhancement of the radiation in the high-mass region due to contributions from the charged internal pion line and inclusion of the respective electromagnetic pion form-factor) (see comparison to the result with no such form-factor-dashed curve). This mechanism modifies the quasi-elastic bremsstrahlung radiation pne^+e^- (with no Δ excitation). The other part of the bremsstrahlung, which is coherently added to the former one, corresponds to the Δ excitation and its subsequent Dalitz decay (Ne^+e^-). Though the latter dominates the total cross section below $M_{e+e} < 0.3$ GeV/c^2, the modified quasi-elastic contribution makes a strong effect at higher masses. However, one should add that the model does not provide a complete description of the inclusive n-p data.

Another explanation of the enhanced dielectron production has been suggested by Bashkanov and Clement [32] pointing that at this beam energy double Δ production plays an important role. Indeed, detailed studies of a two pion production performed by the WASA experiment [33] shows that the double Δ excitation is one of the dominant channels. Thus in addition to the excitation of one resonance only (situation studied in OBE calculations discussed above), one can expect graphs with two excited resonance states.

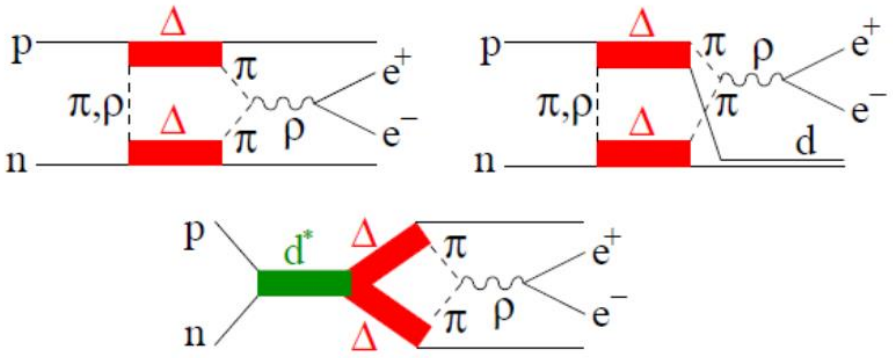

Fig 1.15 Graphs for the e^+e^- production via ρ^0 channel $\pi^+\pi^-$ production in pn collisions. Top: production via t-channel ΔΔ excitation leading to pn (left) and deuteron (right) final states. Bottom: production via s-channel d* formation and its subsequent decay into the ΔΔ system [32].

Furthermore, Bashkanov and Clement demonstrated [32] that in such a case a strong dielectron contribution originating from a subthreshold ρ production in np →ΔΔ→npρ channel can be expected. Such production via intermediate ΔΔ state can only be realized in np collisions due to non-vanishing 9j recoupling coefficient's for the intermediate ΔΔ and I = 1(ρ) dipion final state. Schematic diagrams for such process are shown in **Fig 1.15**. The authors had provided an estimate of the total cross section for the ρ meson production in np collisions to be 310 μb.

The channels included in the calculations [32] are as follows:

1. $np \rightarrow \Delta\Delta \rightarrow np\rho$ $\quad \sigma = 170\ \mu b$
2. $np \rightarrow \Delta\Delta \rightarrow d\rho$ $\quad \sigma = 100\ \mu b$
3. $np \rightarrow d^* \rightarrow np\rho$ $\quad \sigma = 40\ \mu b$

The d* [32] in the channel 3 stands for the recently discovered di-baryon resonance with $I(J^P) = 0(3^+)$, M = 2.37 GeV/c^2 and Γ= 70 MeV, which strongly contributes to two pion production at energies around 1.2 GeV.

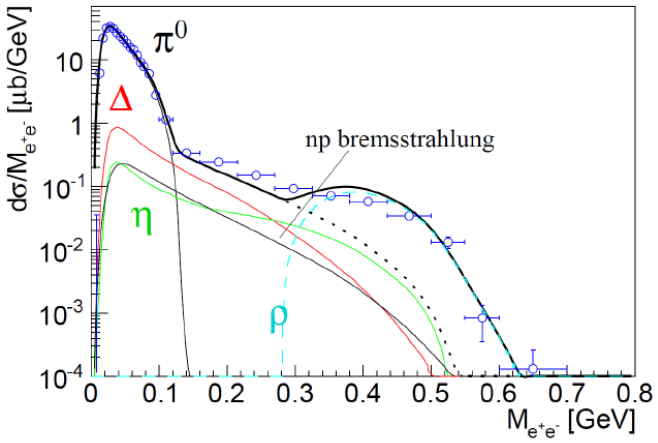

Fig 1.16 e^+e^- final state. e^+e^- invariant mass spectrum, the open circles present the HADES result [34]. The thin solid curves represent calculations for e^+e^- production originating from π^0 decay and bremsstrahlung (black), contributions form single Δ (red) and η (green). The dotted curve stands for the sum of these processes. The dashed (cyan) curve gives the contribution from the ρ^0-channel decay and the thick solid curve is the sum of all these processes. The plot is taken from [32].

The only sizeable way two-pion production may feed the electron-pair production is via $\pi^+\pi^- \to \rho \to e^+e^-$. To calculate the $e^+ e^-$ production it is assumed that the two pions produced in the ΔΔ process interact in the final state by forming a ρ^0, which decays into a $e^+ e^-$ pair.

$$pn \to \Delta\Delta \to pn[\pi^+\pi^-]_{I=L=1} \to pn\rho^0 \to pne^+e^-,$$

For the transition between $\pi^-\pi^+$ into $e^+ e^-$ system a Breit-Wigner formula has been used:

$$|\mathcal{M}(\pi^+\pi^- \to \rho^0 \to e^+e^-)|^2 = \frac{m_\rho^2 \Gamma_{\pi^+\pi^-}\Gamma_{e^+e^-}}{(s-m_\rho^2)^2 + m_\rho^2\Gamma_\rho^2}. \quad (6)$$

Fig 1.16 presents results of the calculations for the case of inclusive np data. The plot presents an incoherent sum of e^+e^- pair sources such as π^0, Δ, η Dalitz decays and the elastic bremsstrahlung contribution [30]. The contribution of the ρ decay has been added in the region M > 0.28 GeV/c^2 which improves agreement with the data. Nonetheless it opens an area of further discussion and analysis addressed in this thesis.

The apparent difference between dielectron production in np and pp reactions has a far reaching consequences for the interpretation of the results obtained with light collisions systems. As shown by the HADES [36] the dielectron production in C+C collisions can be explained by the superposition of the dielectron production in pp and np collisions hence resolving a long standing "DLS" puzzle (see **Fig 1.17**-left). For a long time no theoretical calculation was able to describe the invariant mass distribution measured in C+C collision by the DLS experiment at Bevelac[38].

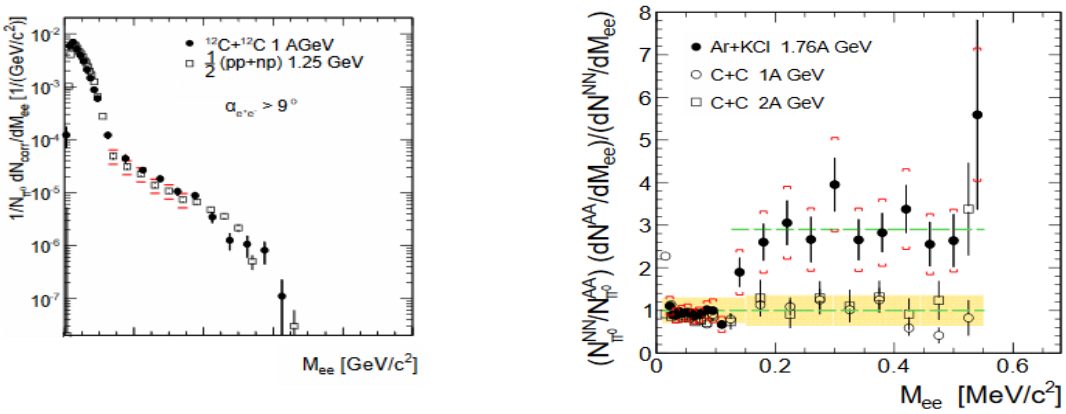

Fig 1.17 Figures showing the HADES measurement of C+C at 2 AGeV (black dots) overlapped with np + pp data. Second picture on the right shows ratios of different data sets to the reference ½(pp + np) data sets [35].

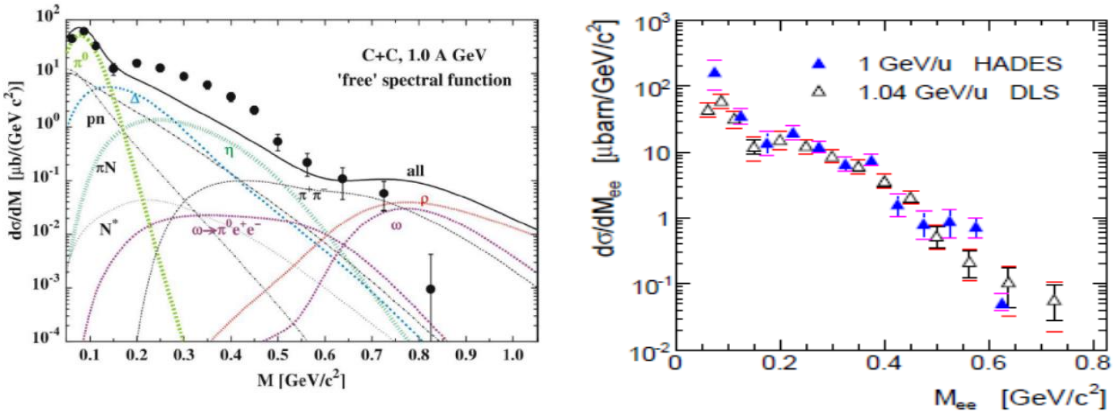

Fig 1.18 Differential cross section in a function of the invariant mass, left plot show C+C data obtained by the DLS (black dots) compared with a simulation (colored lines) [38], on the right canvas a plot showing a comparison of DLS data (empty symbols) with HADES results (blue symbols, HADES data scaled to the DLS acceptance) collected at 1 GeV/u [37,39].

Fig 1.18 (left) shows comparison of the DLS data with model calculations, the sum of all calculated lepton sources underestimated the data points and the main question for a long time was "What is really missing in the calculations? Is it some elementary process which is not correctly taken into account or a in medium effect ? ". The N-N HADES data strongly supports the first explanation (see **Fig 1.17**). The C+C data indeed overlaps with the average of ½(pp + pp) data scaled to the number of participants in the C+C collisions. However, this is not the case for heavier systems where contribution from high density zone shows up, as presented in the right plot in **Fig 1.17**. The figure displays the ratio of the dielectron production in Ar + KCl and C+C to the average of N+N, both scaled to the respective pion yields, as a function of the invariant mass. While for the C+C data the ratio is one for the Ar+KCl the ratio is clearly larger, showing onset of the "medium effect".

In this work the author will prove that the pair production in the exclusive $np \rightarrow npe^+e^-$ final state is very different from the one measured in $pp \rightarrow ppe^+e^-$ and will try to shed more light on the underlying production mechanism. Various differential distributions will be analyzed and compared to the model predictions introduced in this section.

2. HADES

2.1 The HADES spectrometer

The HADES (High Acceptance Di-Electron Spectrometer) spectrometer is located in GSI Darmstadt at the heavy ion synchrotron SIS 18. The system consists of many sub detectors providing the capability of charged particle detection, track reconstruction and momentum determination. It is designed to detect charged particles, mainly positron-electron pairs, coming from botch nucleon-nucleon, pion-nucleon and heavy ion collisions with a beam energy up to few GeV. A schematics sketch of the detector is presented below in **Fig 2.1**.

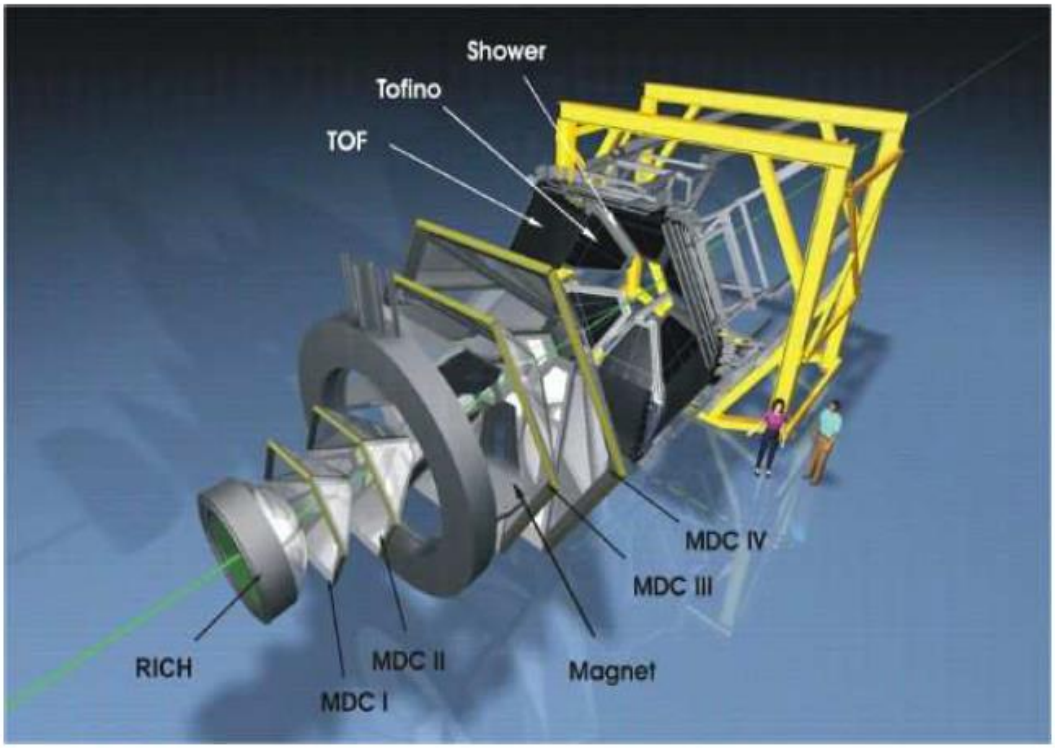

Fig 2.1 Three dimensional sketch of HADES spectrometer. The main components had been pointed out: RICH (Ring Imagine Cherenkov), Magnet, TOF and TOFino (Time of Flight), a set off MDC (Multi- wire drift chambers) and a Shower detector shortly discussed in the following paragraphs.

Due to the fact that the production rate of e^+ e^- pairs in such events is quite low (10^{-5}), the system must provide a high efficiency for electron reconstruction and a high signal purity. A detailed description of the system can be found in [40].

The main advantages of the HADES spectrometer are:

- high mass resolution, $\Delta M_{inv}/M_{inv} \simeq 2\%$ at the light vector meson region
- large geometrical acceptance for di-lepton pairs
- signal to combinatorial background ratio ~ 1 or better for the vector meson mass region ($M_{inv} \simeq 0.75 GeV/c^2$)
- high rate capability, up to 10^6 interactions per second, using multilevel trigger scheme

It is also important to notice that HADES is a low background experiment due to the reduced material budget ($d/X_0 < 1\%$) (d – material thickness, X_0 – radiation length) which is an essential factor for a high resolution electron detection. The detector consist of six sectors covering full azimuthal angle and polar angle acceptance $17^o < \theta < 86^o$. The main parts of the detector will be described in detail below.

2.2 The Start-Veto detector

The Start-Veto detector presented in **Fig 2.2** is a set of two diamond detectors, which size is 15 × 25 mm and thickness of 100 μm. First module, referred as Start is placed 75 cm upstream, second one - VETO, 75 cm downstream from the target. Each module consists of eight horizontal stripes of variable width ranging from 5.4 mm for the most outer strips to 1.55 mm for the inner strips. The thickness was chosen to minimize the effect of multiple scattering and secondary particle production. The main task of this system is to provide a reference start time for all detectors inside the HADES spectrometer and to trigger on reactions. A description of the detector can be found in [97].

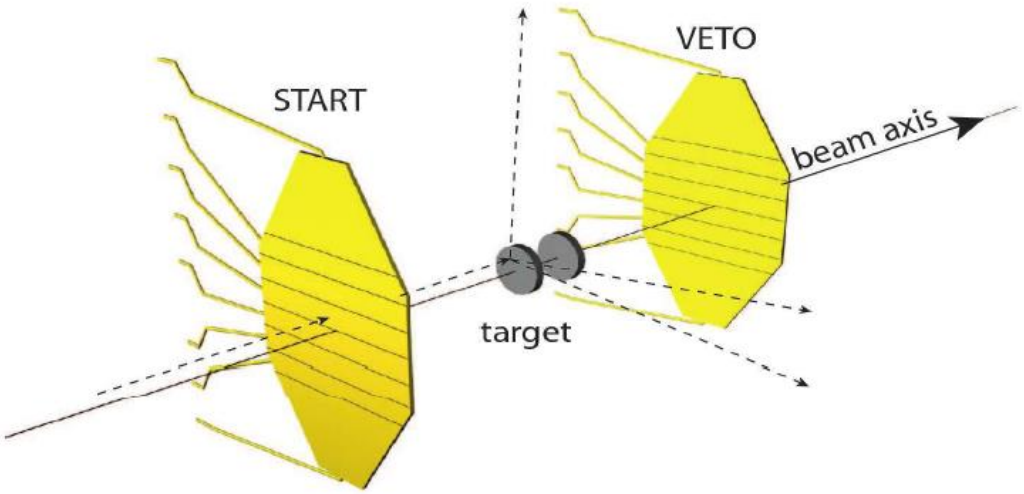

Fig 2.2 Graphics showing START and VETO detector modules in respect to the target.

In the experimental run discussed in this thesis the START detector was not installed, this subject will be evaluated in section **3.3**.

2.3 Ring Imagine Cherenkov (RICH)

The Ring Imaging Cherenkov detector [41], presented in **Fig 2.3**, is the most important part of the HADES detector system as far electron, positron identification is concerned. The focus of the designee is to identify electrons and positrons with momenta p > 0.1 GeV/c. The operation of this detector is based on the Cherenkov effect. When a charged particle traverses through a radiator at a velocity greater than the speed of light in that medium (v >c/n, n is the refraction index), it generates a quanta of light, this is referred as Cherenkov radiation. The opening angle between the emitted cone of light and the particle direction is given by:

$$\cos\theta = \frac{1}{n\beta} \quad where\ \beta = \frac{1}{\sqrt{1-\frac{1}{\gamma^2}}} \qquad (7)$$

where θ is the opening angle, β and γ are the velocity and Lorentz factor of the particle respectively. In the energy range of the experiment, i.e. typical kinetic energy of beams is in the range 1-2 GeV, electrons have velocities close to the speed of light, while most of the hadrons have much lower velocities. By choosing a dielectric medium (C_4F_{10}) with an appropriate refraction index (n=1.00151), hadrons do not emit photons and the detector becomes a reliable tool to discriminate leptons from hadrons.

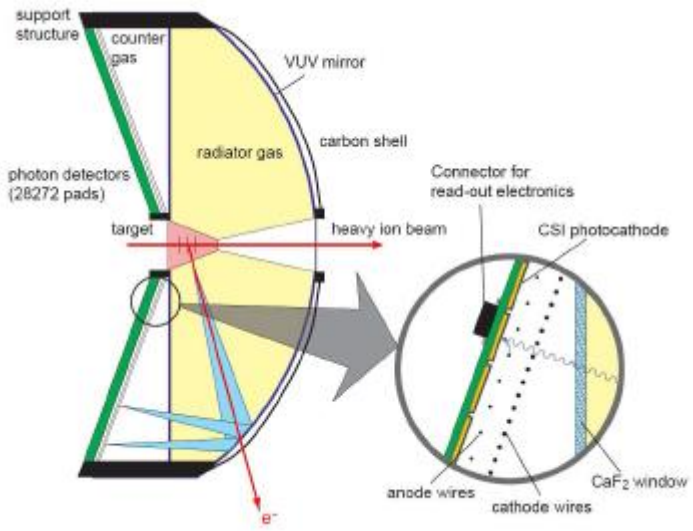

Fig 2.3 Schematic view of the RICH detector and its components: a carbon shell mirror, a CaF_2 window and a photon detector.

The specific refraction index of the RICH radiator (C_4F_{10}) corresponds to the Cherenkov threshold γ_{thresh}>18.2. It means that, to produce the Cherenkov light, the velocity β of a particle should be greater than 0.9985c, which corresponds to the momentum of: p = 0.009 GeV/c for an electron, p = 2.5 GeV/c for a pion and p = 17 GeV/c for a proton. In the HADES experiment energy range, the momentum of electrons is much higher than the 0.009 GeV/c threshold and most of the protons and pions have momenta significantly below the threshold what makes the detector hadron blind.

2.4 Tracking system

The HADES tracking system is designed to measure the deflection of a particle trajectory in the magnetic field. It consists of 24 trapezoidal Multi-wire Drift Chambers (MDCs) [42] symmetrically arranged in six identical sectors and forming four tracking planes, counted from I to IV. In each sector, two modules (I and II planes) are located at the front of and two (III and IV planes) behind the toroidal magnetic field generated by a superconducting magnet, as shown in **Fig 2.4** The Iron-Less Superconductive Electromagnet (ILSE) consists of six superconducting coils surrounding the beam axis and creates a toroidal, inhomogeneous field, which reaches a maximum field of 0.7 T within the acceptance region of the detector, it bends the particles mainly in the polar (θ) direction.

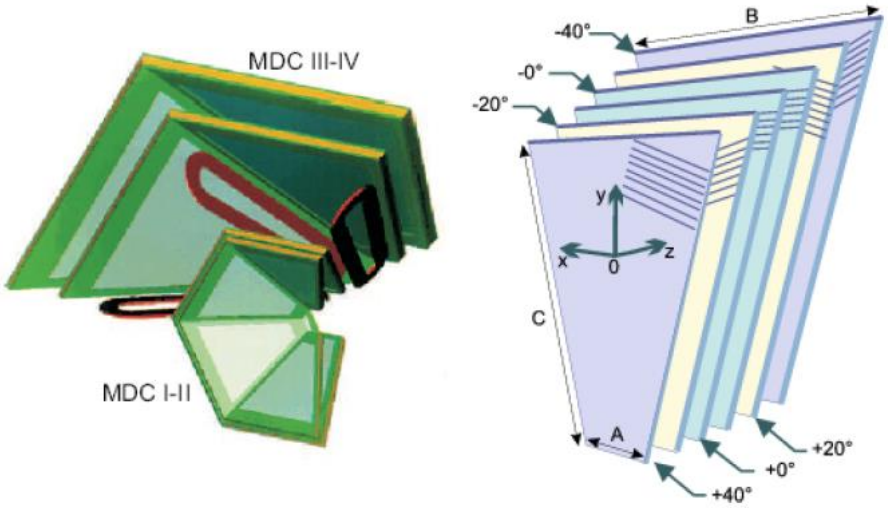

Fig 2.4 Schematic layout of the HADES tracking system. Left: Arrangement of the MDC chamber with respect to the magnetic coils. Right: View of the six anode wire frames inside a HADES MDC, with the respective wire angles.

What is important to underline is that a field free region is required (below $5 \cdot 10^{-3}$ T) at the position of the RICH and the TOF/TOFINO detectors, to avoid distortion of ring shapes and operation of photo-multipliers, respectively. This is assured by a configuration of the toroidal magnetic field.

The track reconstruction is performed by Mini-Drift Chambers(MDC). All the 24 chambers together provide a polar coverage between 14^o to 84^o and nearly full azimuthal coverage. Each chamber is composed of six sense/field wire layers (called anode planes) oriented in different stereo angles from the inner layer to the outer. All four chambers contain about 1100 drift cells each with a size in average varying from 5 x 5 to 14 x10 mm^2 from plane I to plane IV to achieve a constant detector occupancy. Every chamber, has a windows made of aluminized Mylar foils, filled with argon: isobutene (84:16) gas mixture which is circulated during operation with an overpressure below 1 mill bar. A new gas mixture based on CO_2, replacing isobutene, has been tested and was used in the experiments.

When a particle is crossing these drift cells, it ionizes the gas and produces electron/positron ion pairs along its trajectory. The electrons migrate towards the anode wires and produce further ionization especially close to the anode wire. The collected charges induce a signal on the anode wires. For each hit wire the corresponding drift times depend on the minimum distance of the particle trajectory from the wire. It is important to note that the drift time and the drift distances dependence is not linear due to the fact that the filed inside the cells is not constant. The momentum resolution for electrons (or positrons) in a function of momentum is shown in **Fig 2.5**.

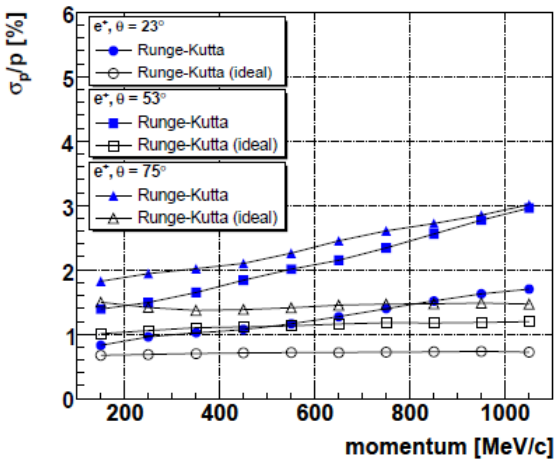

Fig 2.5 Simulation of the momentum resolution for e^+/e^- in a function of momentum. Calculations are done for 3 polar angles. Open circles represent the situation when the detector resolution is included, closed symbols on the other hand present results without the detector resolution [40].

In **Fig 2.5** the simulation results done under consideration of the integrated filed, show a very minimal change of the momentum resolution with the increase of the particle momentum. In this analysis the leptons will have in general low momentum (below 400 MeV/c mostly) as one can see the obtained resolutions in this momentum range are very close to ideal values, this is clearly visible for particles with lower polar angles.

2.5 META (Multiplicity Electron Trigger Array)

The Multiplicity Electron Trigger Array (META) is composed of three sub detector systems:

- large granularity Time Of Flight detector TOF covering polar angles (44° - 88°),
- small granularity Time Of Flight detector TOFino covering polar angles (18° - 45°),
- a Pre-Shower detector covering polar angles (18° - 45°).

The main role of the system is counting the charged particles in each event in order to provide particle multiplicity as a condition for the first level trigger selection.
The META measures the time of flight of each detected particle and electromagnetic showers, in order to provide particle identification. A fast determination of the impact position of each particle, spatially correlated to the position in the hadron-blind RICH detector, allows to perform a second-level trigger for electron tracks.

2.5.1 Time of Flight Detector

The Time of Flight Detector [43] covering polar angles from 44° up to 88° follows the six-sector symmetry of the whole system. Each sector has eight modules. Every module is built of a set of eight scintillator rods connected to photomultipliers on both sides of the rod.

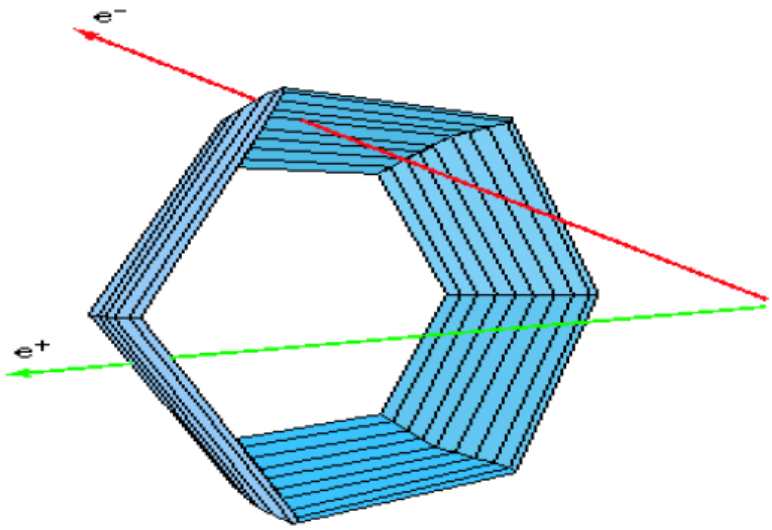

Fig 2.6 Graphical representation of the TOF detector.

A particle when traversing through a plastic scintillator, as shown in **Fig 2.6**, deposits its energy which is converted into a light signal. The signal reaches the pad edge and is

converted into a voltage signal by a photomultiplier. From the measured signals (t_{left} and t_{right}) the time of flight (t_{tof}) of particles, the hit position (marked as x) and the energy deposited in the rod by the passing particle (ΔE) can be extracted as shown below:

$$t_{TOF} = \frac{t_{right} + t_{left} - \frac{L}{v_{group}}}{2} \qquad (8)$$

$$x = \frac{t_{right} - t_{left}}{2} v_{group} \qquad (9)$$

$$\Delta E = k\sqrt{A_{left} A_{right}} e^{L/\lambda_{at}} \qquad (10)$$

where:
x – hit position on the rod
ΔE – energy loss
v_{group} – is the group velocity
λ – light attenuation length
k – constant
L – scintillator length

The estimated time resolution of the TOF system is 150 ns, it corresponds to 2.5 cm of the spatial resolution.

From the measured time of flight and known path length (from the track reconstruction) the velocity can be calculated and analyzed in a function of the momentum. **Fig 2.7** shows a typical two dimensional correlation which is used in the HADES for the particle identification. Well visible intensity structures can be identified with the indicated particle species.

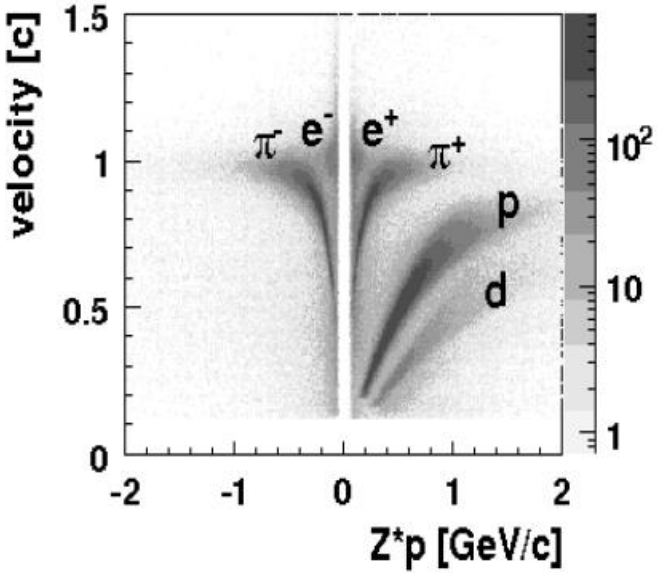

Fig 2.7 Velocity vs charge*momentum plot obtained from the C+C data. Different particle species are marked with the corresponding letters [40].

2.5.2 TOFino detector

The time of flight measurement at polar angles $\Theta < 45^{\circ}$ is performed with a TOFino detector. It consist of six sectors, each made of four scintillator paddles, arranged around the beam axis as presented on **Fig 2.8**. In order to calculate the time of flight, the following equation is used:

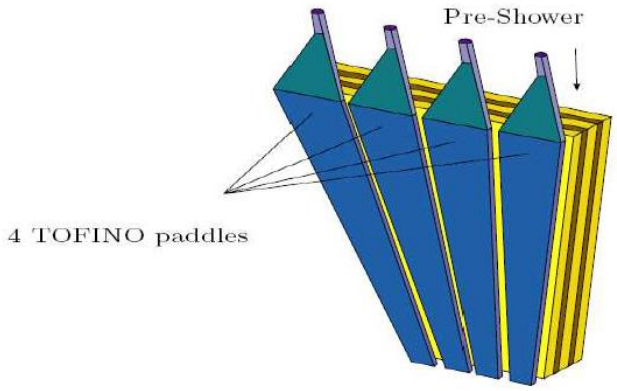

Fig 2.8 Sketch showing the TOFino detector. Blue objects represent TOFino paddles, the Pre-Shower detector is in the back side.

$$t_{TOFino} = t - \frac{x}{v_g} \qquad (11)$$

t – time interval between the reaction and the signal form the paddle
x – distance from the hit positon on the paddle
v_g - light group velocity in the paddle

Since only one edge is coupled to a photomultiplier, no information about the hit position is available. However, the TOFino detector is mounted directly in front of the Pre-Shower detector, which provides the particle hit coordinates on the paddle. The time resolution (420 *ps*) and double hit capability of the TOFino are worse than those of the TOF detector therefore its operation is limited to low multiplicity reactions.

2.5.3 Pre-Shower

The main purpose of the Pre-Shower detector is to identify electrons and positrons at low polar angles ($\theta < 45^{\circ}$) by the electromagnetic shower detection. In this region the separation of electrons from hadrons is more challenging than at large angles due to higher hadron momenta and large hit densities, particularly in case of heavy ion reactions. For this reason the Pre-Shower detector is located directly behind the TOFino and adds the possibility of estimating the position. The structure of the detection system is presented in a **Fig 2.9** below.

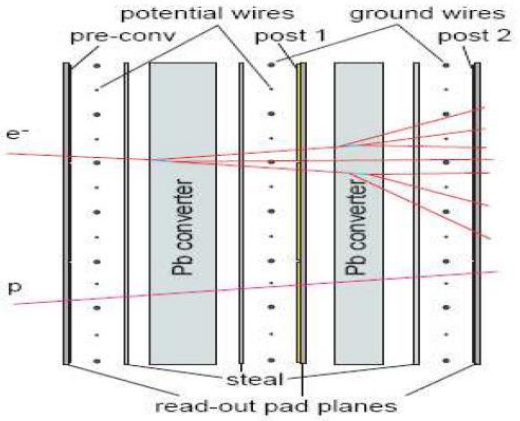

Fig 2.9 Side view of the Pre-shower detector.

Each sector module consists of three trapezoidal wire chambers (called pre-, post1- and post2-chamber), separated by two lead converter plates with the thickness of $x_0 = 2\times$ radiation lengths ($2 \times 0.56\ cm$). One of each cathode planes is subdivided into individual pads (32×32) array where the induced charge signal is taken from. A charged particle passing through the gas chambers produces an ionization avalanche, with electrons drifting towards the closest anode wire. This induces a positive charge on the nearby cathode pads connected to charge-sensitive preamplifiers. The wire chambers are filled with an isobutene-based gas mixture and are operated in the limited self-quenching streamer mode (SQS). In this mode the integrated charge is to some extant proportional to the number of particles traversing given chamber pad than to their energy loss. Comparison of the integrated charges from the different layers is the basis of the electromagnetic shower recognition and separation of the electrons/positrons from the hadrons.

Fig 2.10 shows the difference of integrated (on area of 3x3 pads) charges in the post and the pre-chambers for electrons (triangles) and hadrons (dots) measured in the HADES spectrometer. A clearly different pattern is observed and is used for the electron/hadron separation. The resulting pion/electron suppression in a function of particle momentum is shown on the right panel. For sufficiently high momenta ($p > 500$ MeV/c) more than 80% of pions are rejected.

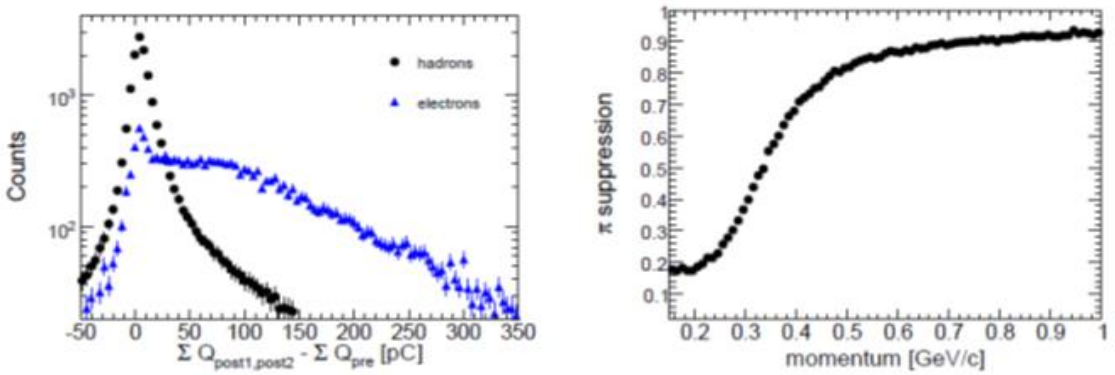

Fig 2.10 Left, plot showing the integrated charge from 3x3 pads, sums are taken form the post1 and the post2 chamber and a charge read from the pre-chamber is subtracted. Right plot shows the pion suppression in a function of the momentum.

2.6 Forward Wall

In order to distinguish pn from pp reaction in dp collisions, the Forward Wall (FW) has been added to the HADES setup. It detects charged particles at low polar angles ($0.33^\circ < \theta < 7^\circ$), thus can be used to tag the quasi-free pn reaction. FW is placed 7 m downstream form the target. The front view of the detector is presented in the **Fig 2.11** (front view) and **Fig 2.12** (side view of the detection system).

The angular and position resolution was achieved by a variable cell size selection: the central part was covered with cell sizes 4 x 4 cm^2 (**Fig 2.11**, red squares), increasing to cell sizes of 8 x 8 cm^2 (green squares) and the outer region was covered with 16 x 16 cm^2 cells (blue squares). The scintillating material used is BC408. The thickness of the cells is 2.54 cm. Each cell is equipped with an individual PMT (photomultiplier) readout. The high voltage of each PMT is individually set to achieve high detection efficiency for protons. The estimated time resolution of the FW is about 500 ps, this corresponds to a momentum resolution of 11% for protons.

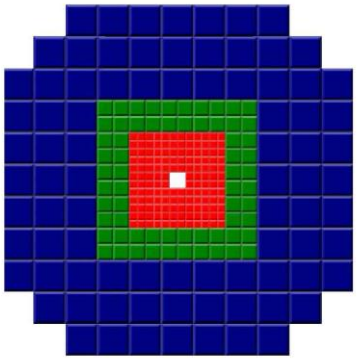

Fig 2.11 Forward Wall geometry. The size of the modules starts from 40 mm x 40 mm up to 160 mm x 160 mm on the border of the detector. There are 320 scintillator and photomultiplier modules. The thickness of the cells is 2.54 cm.

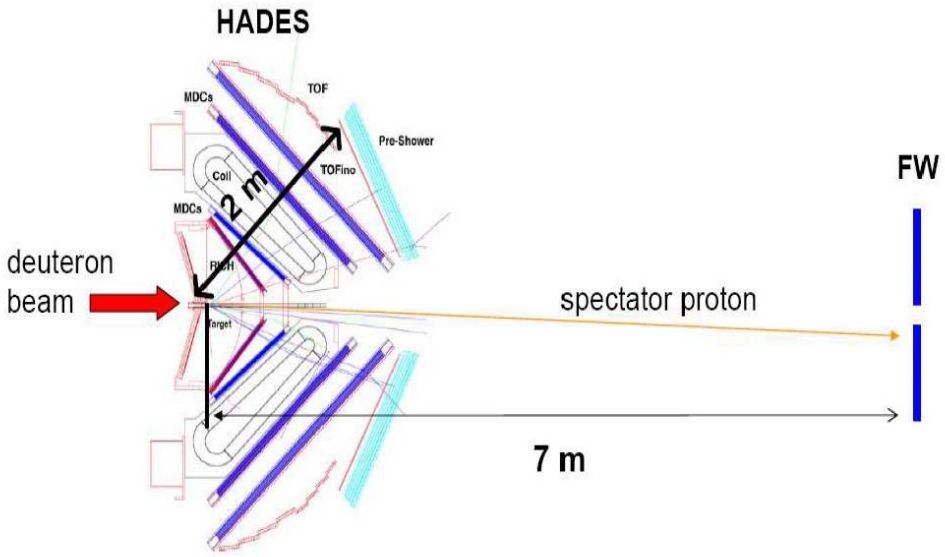

Fig 2.12 Side view of the HADES spectrometer and the Forward Wall (FW) detector, placed 7 meters form the target and dedicated for tagging spectator particles.

2.7 Trigger system

The deuterium beam intensity for the HADES was about 10^7 particles per second. This beam intensity corresponded to $\sim 2 \cdot 10^4$ /s first level (LVL1) trigger rate because of 1% interaction probability in the target and the specific LVL1 condition requiring 2 hits in the HADES and one hit in the Forward Wall. The number of events was, however, still too high to be recorded, therefore the second level trigger (LVL2) was introduced to select lepton events.

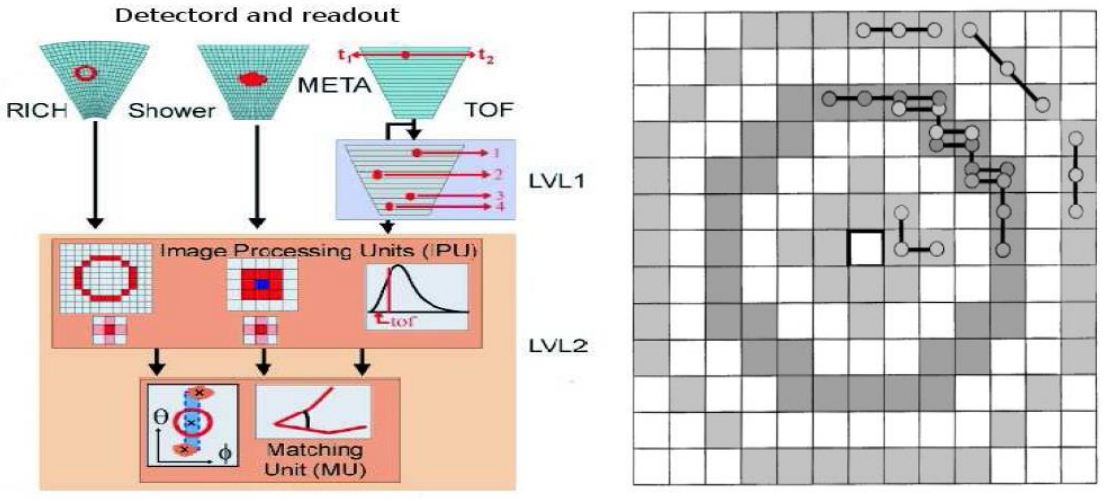

Fig 2.13 The schematic overview of the HADES trigger system. Right: the pattern mask for a hardware ring recognition algorithm with ring region (dark grey) and veto regions (light grey). The dots connected by lines indicate the groups of pads for one-quarter of the search area [44].

The second-level trigger (LVL2) uses the online electron pattern recognition. The main task of the LVL2 is to perform fast ($t < 10\ \mu s$) real-time electron identification in order to limit the amount of data written. In dp experiment LVL2 condition was to find at least one electron candidate. In more details electron identification performed by the LVL2 trigger is made in two steps (shown in **Fig 2.13**):

• electron pattern recognition in the dedicated processor units: Cherenkov rings in the RICH, fast particles in the TOF (inside pre-programmed time of flight window), electromagnetic shower in the Pre-Shower.

• spatial matching of the electron candidates via applying angular correlation (polar and azimuthal) in the Matching Unit

Only events with positive LVL2 decision, and some fraction (down-scaled) of un-triggered LVL2 events but with positive LVL1 were recorded. The downscaling purpose is to select and scale down events in a statistical fashion, regardless of whether they contain lepton pair or not, for hadronic analysis and normalization purposes.

This LVL2 trigger has an efficiency $\sim$85% for electron pairs, therefore, for evaluating the number of dilepton events in the data sample respective correction has to be taken into account. In further analysis a global factor 0.85 will be introduced, representing LVL2 trigger bias. More details of the trigger performance can be found in [44].

3. The exclusive pn→ pn e^+ e^- channel reconstruction

3.1 Introduction into the analysis

The review of the inclusive invariant mass spectra points to a substantial difference between pp and np data sets (see section **1.3.2**). The exclusive channel **npe$^+$e$^-$** can characterize better the production mechanism and can be compared to calculations, also done for such a final state. In addition to e^+e^- pair a proton must be identified in the HADES spectrometer, and as before, a forward going $p_{pectator}$ particle is detected in the Forward Wall. Since the spectrometer has no capability of detecting neutral particles the neutron will be selected via the one- dimensional cut applied on the pe^+e^- missing mass around the neutron mass. A condition on the opening angle between the e^+e^-: $\alpha_{ee} > 9^o$ will be applied to reduce contribution form the $\gamma \rightarrow e^+e^-$ conversion. In the next section consecutive steps of the analysis are presented.

3.2 Proton spectator selection in the Forward Wall

Proton spectator identification is based on a momentum cut. The momentum in FW is obtained from the time of fight and the known distance to the selected detector cell. In the analysis it is assumed that a spectator particle carries the mass of a proton. In most cases there was only one hit in FW, when two or three particles were recorded it was assumed that the spectator particles is the fastest one (because it carries momentum of the beam). The momentum is calculated assuming the known proton mass as presented below:

$$\beta = \frac{L}{T_c}$$

$$p = M * \sqrt{\frac{1}{\frac{1}{\beta^2} - 1}} \tag{12}$$

where:

β - velocity
L - distance from the target to FW cell
T_c - time of fight measured in FW detector
p - momentum
M - mass

In order to account for the finite time of flight resolution of FW (around 800 ps) the respective momentum uncertainty has been calculated. Finally, the selection window starts from 1.6 GeV/c up to 2.6 GeV/c and is centered around nominal value of the beam momentum p = 1.98 GeV/c. The window is very broad and its width is equivalent to ± 4σ.

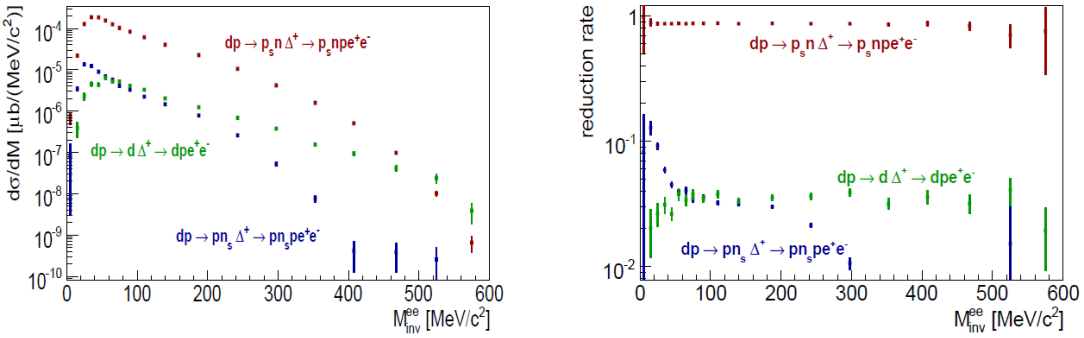

Fig 3.1 Left: Inclusive invariant mass distribution of e^+e^- in HADES acceptance with spectator conditions. Right: Reduction rate of survived dielectron pairs after additional spectator conditions as a function of e^+e^- invariant mass for various reaction channels. The procedure is described in [45].

From the results of the simulation [45] shown in **Fig 3.1** one can conclude that FW acceptance amounts to at least 84% for the reactions of the type dp →$p_{spec}npe^+e^-$. Therefore a factor of 0.84 will be used in the analysis to correct for the Forward Wall acceptance and efficiency.

3.3 Proton identification inside HADES.

As discussed above the particle identification of charged particles in the HADES spectrometer is provided by the RICH, the tracking and the META system.

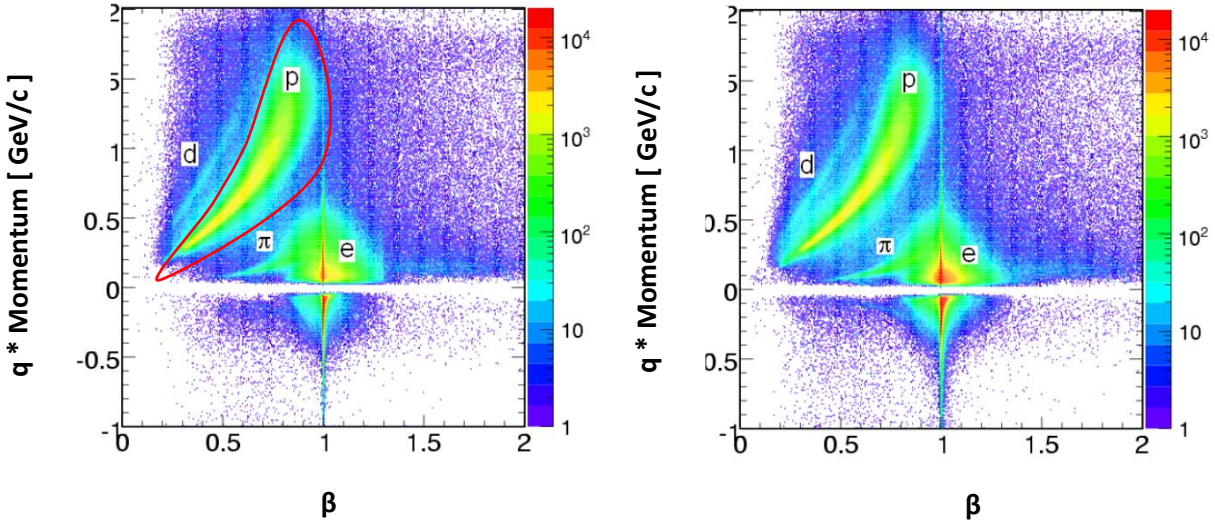

Fig 3.2 Particle velocity vs charged * momentum, clear pattern visible for the reconstructed hadrons (proton, π etc.) Plots are made for TOFino (right) and TOF (left), the statistics corresponds to data obtained in one day.

Hadrons (in the reaction of interest mainly protons and π) are identified by combining the momentum of a particle, and its time of flight in the TOF/TOFino systems. It is important to state that in case of the deuterium beams of relatively high intensity (few times 10^6 /s) it was not possible to use the Start detector. It was due to a background obscuring stable RICH performance and also low efficiency of the diamond detector for deuterium detection (the detector at this time was operated only for HI beams). For that reason a reaction time (t_0) has been calculated from each event from the measured time of flight and the momentum of the identified particle, called a reference particle. For the events without electron or positron (called later electrons) a particle with the negative charge was assumed to be π^-, as the most abundant particle species at this energy. In the events with identified electrons in the RICH, as described in next section, either electron or positron was taken as the reference particle. This assumption is almost 100% correct since the RICH is hadron blind detector and for a low multiplicity events there is very small chance of random track correlations. Knowing the electron path length from the trajectory reconstruction the respective TOF was calculated.

In the events with di-electron pairs, which are of relevance for this analysis, one of either electron tracks was used as the reference for calculation of the reaction time (t_o). For such events one can reconstruct, event by event, the reaction time and use it as the reference for all other particles in the event:

$$t_{offset} = t_{exp} - t_o \qquad (13)$$

where:
t_{exp} - is the measured time for identified electron.
t_o – theoretical value calculated from known momentum.
t_{offset} is added to the time of flight of all other particles in the same event

Finally, the protons were then reconstructed via two-dimensional cuts imposed on the velocity vs the momentum correlations, as shown in **Fig 3.2** for the electron events (red shape in left plot). The very narrow correlation lines visible for the electrons are just consequence of the applied method assuming electron tracks as the reference particles. More details on the procedure can be found in [45].

3.4 Di-lepton identification

Lepton identification is a crucial part of this analysis, and has been carried out as described in the following steps:

- track and momentum reconstruction of a particle
- Cherenkov rings reconstruction in the RICH detector
- Time of flight calculation
- application of the momentum dependent condition on particle velocity β measured in the TOF and TOFino detectors
- spatial correlation of the track passing the velocity condition with the track providing ring in the RICH detector

The momentum of each track in the event is obtained from the deflection of its trajectory in the magnetic field as it was described in section **2.4**.

The Cherenkov rings in the RICH detector have a constant diameter. This feature simplifies a reconstruction algorithm which in this analysis was based on a pattern matrix method described in [48]. The structure of 13×13 pads with the appropriate weights reflecting the ring image properties, presented schematically in **Fig 3.3**, was overlapped with the RICH sector pad plane. For each pad the measured charge is multiplied with weight from the mask. The sum of obtained values produces a quantity defined as a ring quality. This procedure is done for all pads to find local maxima which are selected to be ring candidates.

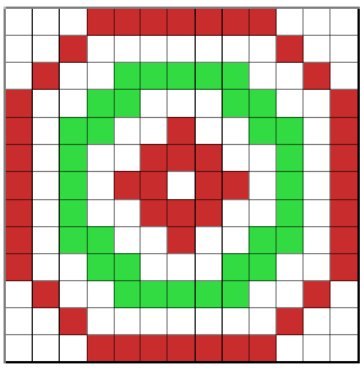

Fig 3.3 Pattern mask for the ring recognition procedure. Green and red regions show the positive and negative weights.

The ring quality can be characterized by:

- pattern matrix quality parameter
- Ring centroid - the difference between the center of gravity of charge as deduced from the pulse heights and the fitted geometrical center of the ring.

The observables had been calculated from the experimental data and compared with the simulation. The results are presented below in **Fig 3.4** and show fair agreement with the simulation results, except some shift in the distributions of the number of active pads.

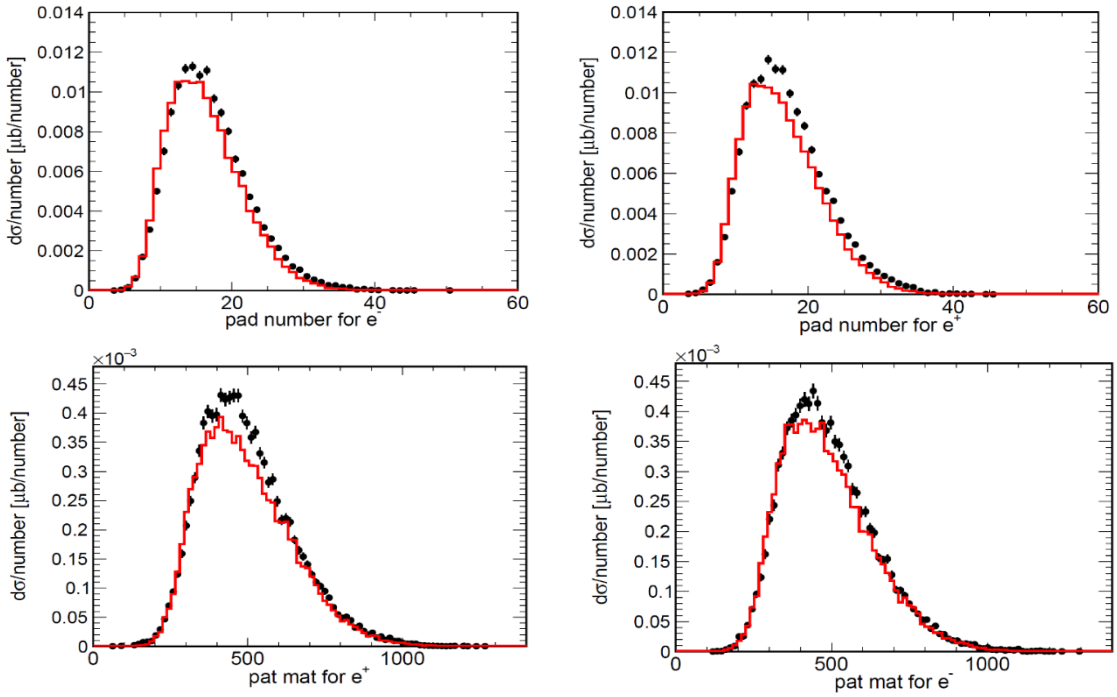

Fig 3.4 Pad number (upper plots) and patter matrix amplitudes obtained from experimental data set compared with simulation. The simulation follows the data shape at a reasonable level.

Further, the time of flight calculation is carried out. In the first stage, the time calibration of TOF/TOF$_{INO}$ is done using lepton pairs identified by the RICH emitted in the same event. Knowing the path lengths from the trajectory reconstruction and correcting the respective TOF for the differences in the lengths one can calibrate all TOF modules.

Finally events with at least two electron candidates found in the RICH was taken for the further processing. The final step of the dilepton identification procedure was a cut on the time of flight. Knowing that leptons move with high velocity $\beta \sim 1$ a condition of $\beta > 0.8$ was introduced, resulting in a two-dimensional condition imposed on the track velocity and the momentum, as presented in **Fig 3.5**. One can see clear enhancement for the electrons. Narrow lines at $\beta = 1$ are those tracks which have been used as the reference tracks. A more narrow distribution for electrons is due to the pre-defined priority to use TOF hits (with a better resolution) as reference tracks. Because of the given magnetic field polarity low momentum electrons preferentially hit TOF.

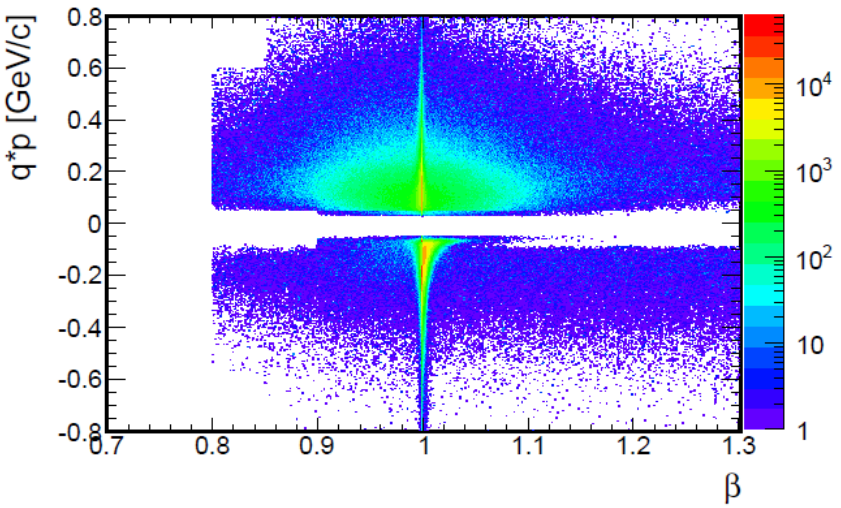

Fig 3.5 Experimental data: distribution of polarity × momentum vs beta for e^+e^- with a time of flight cut.

3.5 Combinatorial background calculation and dielectron signal extraction

The main source of the background are pairs produced by a photon conversion in the detector material. The conversion background originates from an external pair conversion of photons mainly coming from single or multiple π^0 decays. It is the source of a combinatorial background (CB) arising when di-lepton pairs are created from all possible e^+e^- combinations inside the same event, not necessarily originating from the same decay vertex.

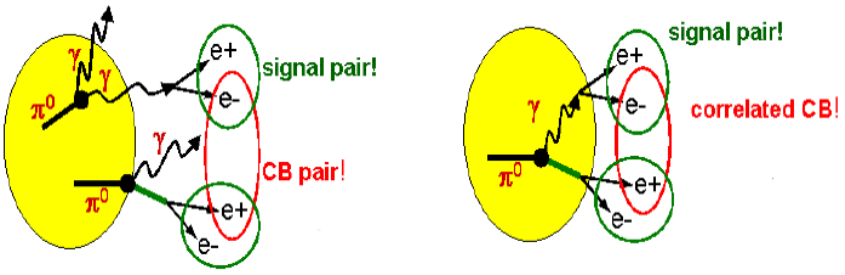

Fig 3.6 The sources of uncorrelated and correlated combinatorial background.

The combination between leptons (**Fig 3.6**) originating from two independent sources gives the contribution to the smooth background. On the other hand there is also a correlated background which originates mainly from the $\pi^0 \rightarrow \gamma\gamma$ decay or the π^0 Dalitz decay, where a positron and an electron come either from two conversions or from the Dalitz decay and from the conversion in the single π^0 decay. In the experiment described in this thesis the main source of the conversion was inside the target material (green area in **Fig 3.7**) and the RICH flange, as illustrated in **Fig 3.7**.

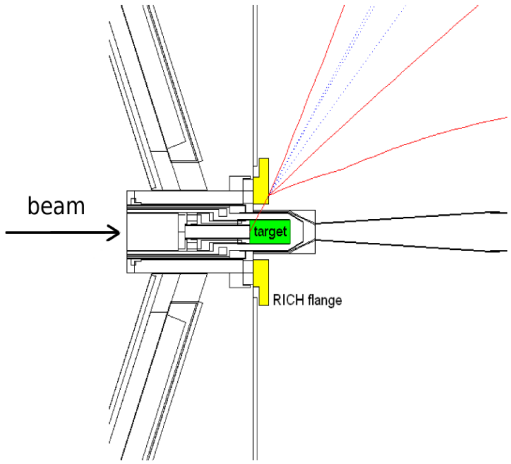

Fig 3.7 Example of the background production on detector material.

To select only the interesting dilepton pairs coming from the target a topological cut on the correlation between the emission angle vs vertex position along the beam axis (z) was introduced removing conversion from the RICH flange, as shown in **Fig 3.8**. The area selected with red lines shows the sample removed from the analysis.

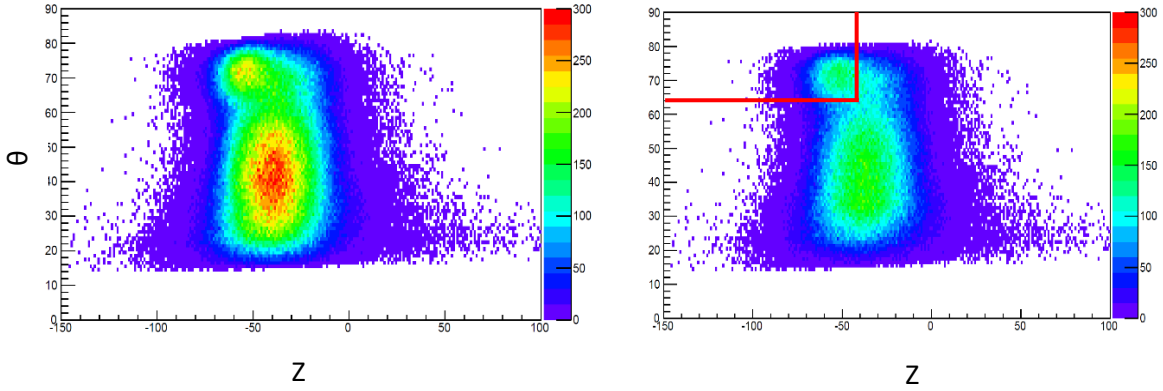

Fig 3.8 Distribution of the polar angle (θ) vs track vertex positon (z) for electrons (left) and with section criteria. Red square represents the area of rejected particles.

The remaining dielectron pairs were combined into pairs of like-sign and opposite-signs and the combinatorial background as estimated according to the prescription commonly used in dielectron analysis [49].

$$N_{CB} = 2 * \sqrt{N_{++} * N_{--}}$$
$$N_{sig} = N_{+-} - N_{CB} \quad (14)$$

where:

N_{++}/N_{--} - are the like sign pairs
N_{+-} – are the opposite-sign pairs

At invariant mass $M_{ee} > M\pi^0$ where the N_{++} and N_{--} distributions are not symmetric or missing the N_{CB} is calculated as follows.

$$N_{CB} = N_{++} + N_{--} \qquad (15)$$

The obtained signal pairs can be plotted in bins of any desired observable (the invariant mass, emission angles etc.). This procedure of the CB subtraction has been extended in the same manner also for the events including proton. For example CB three-particle quantities like proton-dielectron invariant or missing masses, which will be shown below, were calculated as given by equation (14 and 15)

Fig 3.9 shows the dielectron invariant mass distributions of the signal and the CB obtained for the events with the identified pe^+e^- tracks.

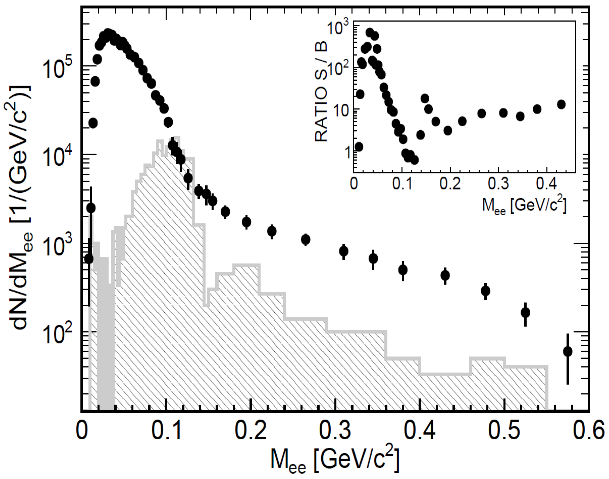

Fig 3.9 Distribution of the exclusive invariant mass of e^+e^- pairs, signal (black dots), CB (gray) and the ratio of Signal to Background (S/B) (inset).

The obtained signal to noise ratio is higher than 10 in the mass region above 0.14 GeV/c^2 and the contribution of the CB is very small. The significantly worse signal/background ratio at 0.1 GeV/c^2 originates from correlated background from π^0 decay.

3.6 Neutron missing mass selection

The HADES spectrometer has no capability of detecting neutral particles. The only possible way of selecting such a particle is via the missing mass. The quasi free $np \rightarrow np\ e^+e^-$ reaction channel was finally selected via a conditions imposed on the missing mass calculated for all three-particle (dielectron and proton) combinations present in the given event (in most cases it was only one such combination per event):

- for all identified particles 4 vectors are calculated

This leads to $(n_{projectale} + p_{target}) - (p\ e^+\ e^-)_{\text{inside hades acceptance}} = \text{missing mass}$.

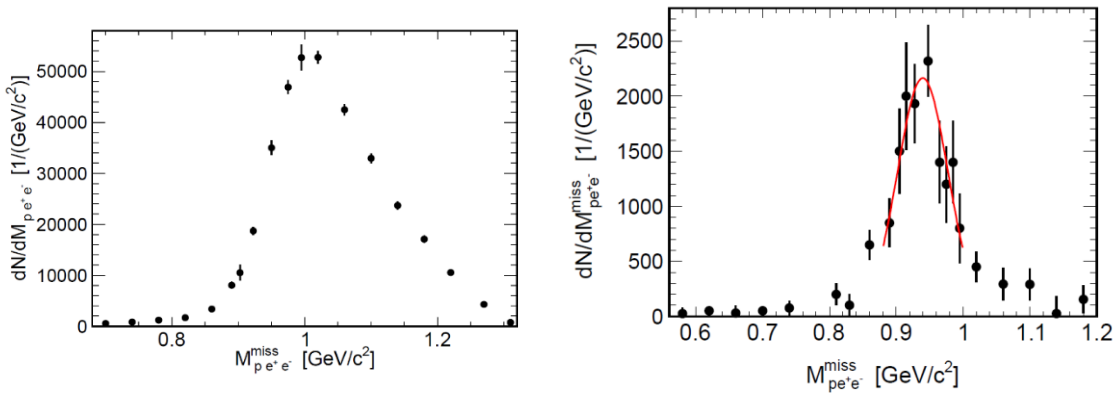

Fig 3.10 Missing mass spectra obtained from experimental data. Left: Spectrum calculated for the total e^+e^- invariant mass region. Right: the same as before but for $M_{ee} > 0.14$ GeV/c^2.

The missing mass spectra with subtracted CB are shown in **Fig 3.10**. The left panel shows the spectrum without any selection on the dielectron invariant mass while the right one with a cut $M_{ee} > 0.14$ GeV/c^2. The distribution with the cut shows a clear but broad peak round the neutron mass. The spectrum on the left side is much broader and shifted to a higher mass, this is related to the fact that it is dominated by $\pi^0 \rightarrow \gamma e^+e^-$ and the photon is not registered by HADES. In order to select the final state of the final state of pne^+e^- a selection window (0.8 GeV/c^2 up to 1.08 GeV/c^2) with the width of 3σ (fit is shown in **Fig 3.10** on the right).

The presented spectrum in **Fig 3.10** was fitted with a Gaussian function to calculate the mean (0.944±0.003 GeV/c^2) and σ values (0.037±0.004 GeV/c^2). The significant boarding of the spectrum is caused by the momentum distribution of the neutron in deuteron, as it is discussed in chapter **1.3.2**.

3.7 Normalization to elastic scattering

The pp elastic scattering events from the quasi-free scattering $dp \rightarrow ppn_{spec}$ were collected during the experimental run in order to obtain the normalization factor. The energy and momentum conservation provides the following condition for quasi-elastic pp pairs selection:

$$|\varphi_{p1} - \varphi_{p2}| \approx 180^o \qquad (16)$$

and

$$\tan(\theta_{p1}) - \tan(\theta_{p2}) \approx \frac{1}{\gamma_{cm}^2} \qquad (17)$$

where φ, θ are the azimuthal and the polar angles for protons, γ is the Lorentz factor:

$$\gamma = \sqrt{\frac{E_k - m_{pr}}{2}} \qquad (18)$$

where m_{pr} is a mass of a proton. In dp collisions, particles momenta, therefore also γ, are slightly modified, due to relative proton-neutron motion inside the deuterium.

Two-dimensional distributions of $\Delta\varphi_{p1p2}$ vs. $\tan(\theta_{p1}) * \tan(\theta_{p2})$ presented in **Fig 3.11** show a well-defined correlation of elastic events both in the simulation (left) and the experiment (right). One can see that in the experimental data the inelastic events (considered as background) are visible as well (they were not included in the simulation). An elliptical cut was introduced, it corresponds to 3σ section both in X and Y axis to select events corresponding to the elastic scattering.

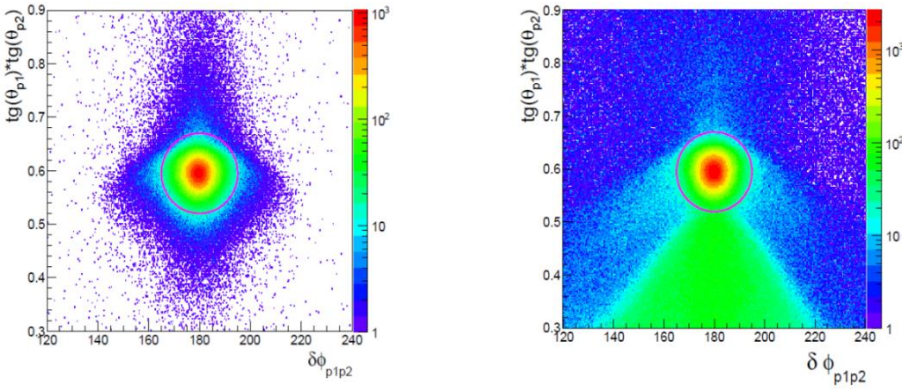

Fig 3.11 Correlations of $\Delta\varphi_{p1p2}$ vs. $tan(\theta_{p1}) * tan(\theta_{p2})$ done for the Monte-Carlo simulation (left) and experimental data sets (right). The events placed inside a red ellipse (3σ) were accepted as coming from elastic scattering.

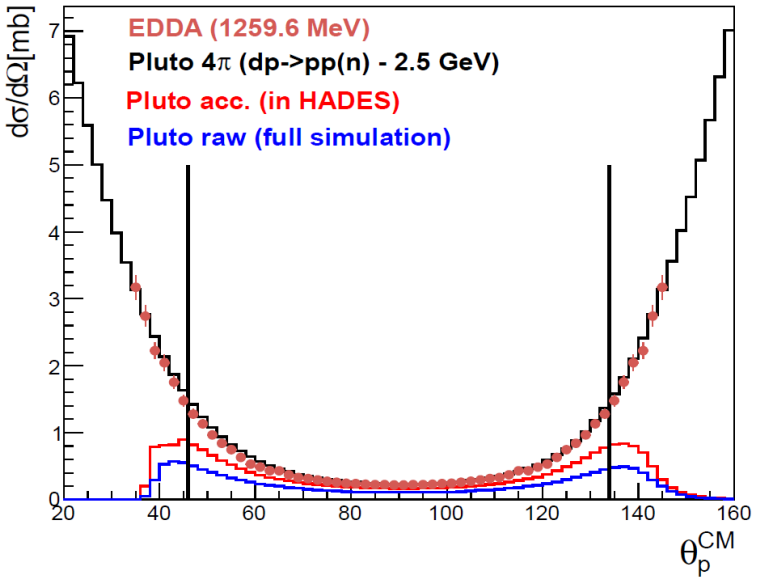

Fig 3.12 Comparison of the experimental data, corrected for the detector acceptance and reconstruction inefficiency, to the simulation with a distribution and cross section taken from the EDDA experiment [50].

To obtain the number of pp elastic events, an angular range of the proton in centrum of mass frame (CM) $\theta_p^{CM}(46^\circ - 134^\circ)$ was selected (**Fig 3.12**). In this range experimentally measured data were compared to the distributions measured by the EDDA experiment [50]. The experimental spectra were corrected for the detector acceptance and the reconstruction inefficiency. The correction was obtained as the ratio of the reconstructed and the full solid angle yields (formula **19**). **Fig 3.13** shows the correction factor as a function of a proton CM angle.

$$Correction(\theta) = \frac{4\pi\ SIM\ \ (\theta)}{Acceptance\ (\theta)} \qquad (19)$$

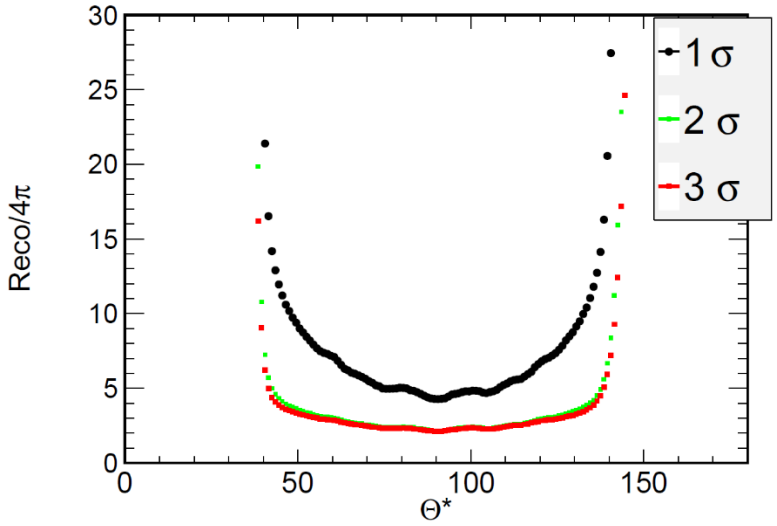

Fig 3.13 Correction obtained from Monte-Carlo simulation, the call calculations are done for a set of different elliptical cuts, 1 to 3 σ applied on data presented in **Fig 3.12**.

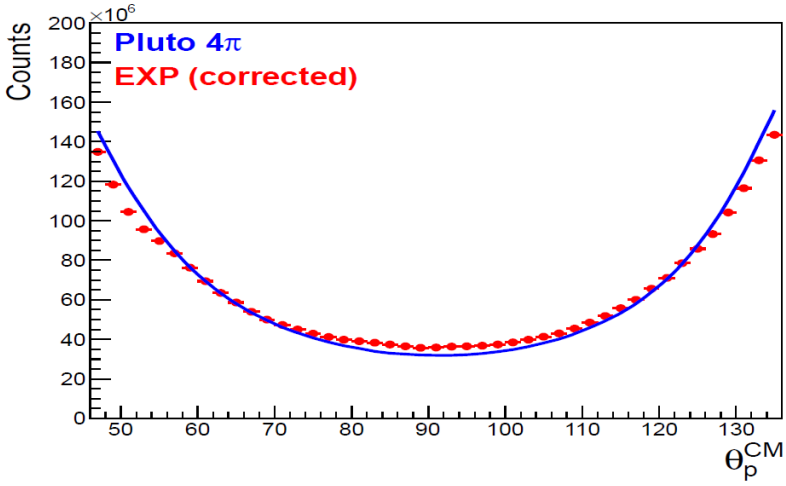

Fig 3.14 Comparison of the experimental data, corrected for the detector acceptance and the reconstruction inefficiency, with the simulation based on the parametrization from the EDDA experiment [50].

The corrected experimental distribution of a proton polar angle in center of mass frame is presented in **Fig 3.14** together with distribution generated by the PLUTO event generator [52] in the full solid angle. The total number of pp elastic events in the range of ($46^o - 134^o$) of the proton polar angle spectra is $N_{pp} = 1.35 \cdot 10^9$. The error has been estimated a shown below:

$$\Delta N_{elastic}^{46^0-134^0} = 1.751 * \sqrt{\sum_{i=46}^{134} \delta_i^2 * f_i^2} = 2.94 * 10^7 \quad (20)$$

where:

1.751 – is the respective acceptance correction factor;
f_i – is abundance weight according to the elastic cross section;
δ_i – stands for yield uncertainty in the *i*-th bin of the scattering angle obtained by the difference between the yield of elastic scattering both in the experiment and in the simulation after normalization to the same area.

The differential cross section from dσ/dΩ distribution (**Fig 3.12**) was calculated by using the following formula:

$$\int \frac{d\sigma}{d\Omega} \cdot d\Omega = 2 \cdot \pi \cdot \sum \sigma_i \cdot [cos(\theta_r) - cos(\theta_l)] \quad (21)$$

where θ_l and θ_r are left and right limits of the θ intervals.

The value of the pp elastic cross section in the region measured by HADES θ_p^{CM} ($46^\circ - 134^\circ$) calculated from the EDDA data is 3.98 ± 0.16 mb. The error has been estimated as follows:

$$\Delta\sigma_{elastic}^{46^0-134^0} = \sqrt{\sum_{i=46}^{134} \sigma_i^2} = 0.16\, mb \quad (22)$$

where σ_i stands for the uncertainty of the measurement in the EDDA experiment for an *i* -th bin in a function of a polar angle.

The normalization factor with obtained numbers of pp elastic events and the value of the cross section obtained as follows:

$$\frac{\sigma_{pp}}{N_{pp}} = (2.95 \pm 0.17) * 10^{-9}\ mb/event$$

3.8 Comparison of the data to expected models (model I and model II)

As discussed in the introduction recent calculations of [31] and [32] offer an explanation of inclusive dielectron data measured in the np collisions at T = 1.25 GeV. A salient feature of both models is an enhancement in the dielectron invariant mass spectrum apparent for $M_{e^+e^-} > 0.3$ GeV/c^2 due to the intermediate ρ-meson state. The models had been chosen as a basis for simulation, which is describe in details below.

The model proposed by Bashkanov and Clement [32] considers a sub-threshold ρ-meson production, via intermediate double delta $\Delta^+\Delta^0$ excitation, and its subsequent e^+e^- decay via ρ, according to the strict Vector Dominance Model (VDM)[6]. The events, containing four vectors of $pn\gamma^*$, have been provided by the authors [32]. The dielectron decays of the ρ have been modelled in the Monte-Carlo simulations following the VDM prescription for the ρ-meson differential decay rate (see **1.3.2**) and assuming isotropic electron decay in the virtual-photon rest frame. The total exclusive cross section for this channel is assumed to be 210 μb since only channel 1 and 2 (see **1.3.2**) contribute in the analysis.

The remaining dielectron sources included in this model, later referred as model I, π^0, Δ and η Dalitz decays, were computed using the PLUTO [52] event generator, as it has been done in [32]. The following channels are included in the simulations:

1. $d + p \rightarrow p_{spec} n\Delta^+ \rightarrow p_{spec} np\pi^0 \rightarrow p_{spec} np\gamma e^+e^-$ $\sigma = 3.7\, mb;\ BR = 0.012$
2. $d + p \rightarrow p_{spec} n\Delta^0 \rightarrow p_{spec} pn\pi^0 \rightarrow p_{spec} pn\gamma e^+e^-$ $\sigma = 3.7\, mb;\ BR = 0.012$
3. $d + p \rightarrow p_{spec} p\Delta^0 \rightarrow p_{spec} pne^+e^-$ $\sigma = 5.54\, mb;\ BR = 4.94 * 10^{-5}$
4. $d + p \rightarrow p_{spec} n\Delta^+ \rightarrow p_{spec} npe^+e^-$ $\sigma = 5.54\, mb;\ BR = 4.94 * 10^{-5}$
5. $d + p \rightarrow p_{spec} np\eta \rightarrow p_{spec} pn\gamma e^+e^-$ $\sigma = 13.6\, mb;\ BR = 5.86 * 10^{-3}$
6. $d + p \rightarrow p_{spec} d\eta \rightarrow p_{spec} d\gamma e^+e^-$ $\sigma = 23.9\, mb;\ BR = 5.82 * 10^{-3}$

And in addition:

7. $d + p \rightarrow p_{spec} \Delta\Delta \rightarrow p_{spec} pn\pi^0 \rightarrow p_{spec} pn\gamma e^+e^-$ $\sigma = 0.515\, mb;\ BR = 0.012$
8. $d + p \rightarrow p_{spec} \Delta\Delta \rightarrow p_{spec} pne^+e^-$ $\sigma = 0.391\, mb;\ BR = 4.82 * 10^{-5}$

The cross section and branching ratios are taken from [51]. One can clearly state that the π^0 production in this energy region is dominant. According to [51] the main source of the π^0 are decays of the Δ(1232) (reaction 1 and 2), as also given by a resonance model shown in **Fig 3.15**. The Δ(1232) can directly decay to the e^+e^- and nucleon in Dalitz decay $\Delta \rightarrow Ne^+e^-$ with branching ratio (BR) at resonance pole $4.94 \cdot 10^{-5}$ (a theoretical value deduced form [98]). The mass dependent branching ratio BR(M) for this decay has been given by [52] and implemented in the PLUTO event generator [7]. This contribution is important because it populates the $M_{ee} > 0.14$ GeV/c^2 region, where the excess of the yield is visible, (see **Fig 1.13**) and will be given special attention in this study.

Furthermore the simulation includes angular distributions of the Δ excitation concluded from the partial wave analysis of one pion production in the pp collisions at the same energy [19] (note that for the pp only the isospin I = 1 channel contributes).

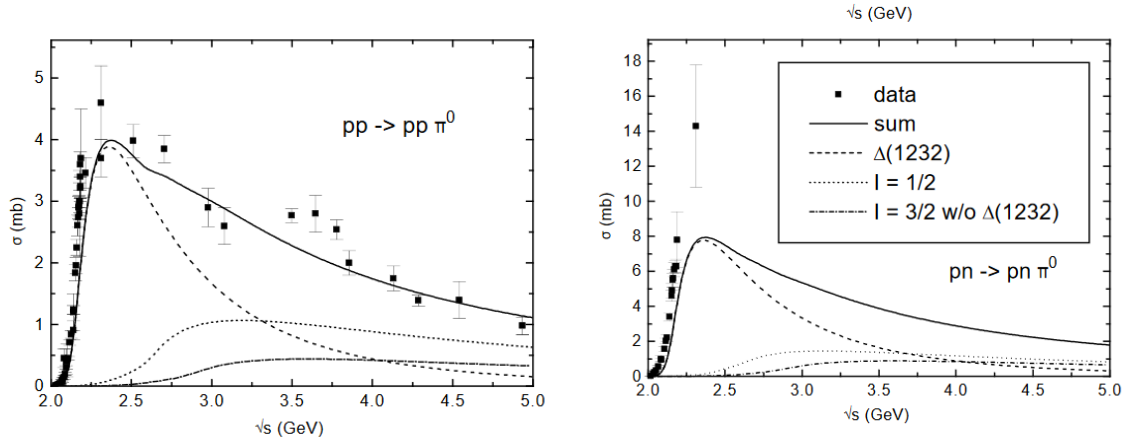

Fig 3.15 Left: one-pion production cross sections (solid curve) for channels with different isospins in a function of $\sqrt{s}$ [51]; in the description of a resonance mode contributions originating from the Δ(1232) (dashed); the isospin 1/2 resonances (dotted); the isospin 3/2 resonances (dashed dotted) according to [51]. Right: pn → pnπ^0 production cross section taking into account the contributions coming from the decay of baryonic resonances (dashed curve) and total cross sections calculated by adding the direct pion production in N-N collisions (solid curve) compared to various experiments.

It is important to point out that also η meson can be produced in the dp reaction at 1.25 AGeV. E_{kin} = 1.25 GeV is the kinetic energy which corresponds to the η meson production threshold in free N−N collisions. However, as already mentioned, when the relative momentum of nucleon inside deuterium is opposite to the momentum of the beam, the available $\sqrt{s}$ is larger and η can be produced. The respective production cross sections have been taken from [29] and [53]. However, as it will be shown the contribution coming from η will be mostly removed (reaction 6) due to a selection window on the missing mass (see **Fig 3.20**).

In the model of Shyam and Mosel [31] a coherent sum of the nucleon-nucleon bremsstrahlung contributions have been calculated. The channel was simulated with the respective distribution of the dielectron invariant mass to account for the results of [31]. Unfortunately, the proposed model does not provide details about angular distributions of the final state particles. Since there is no guidance in the model on angular distributions of the protons and the virtual photons, it was assumed the same as in the model I for the Δ. This model is denote as model II.

To compare theoretical predictions with the extracted experimental signal a procedure has presented in **Fig 3.16** has been applied.

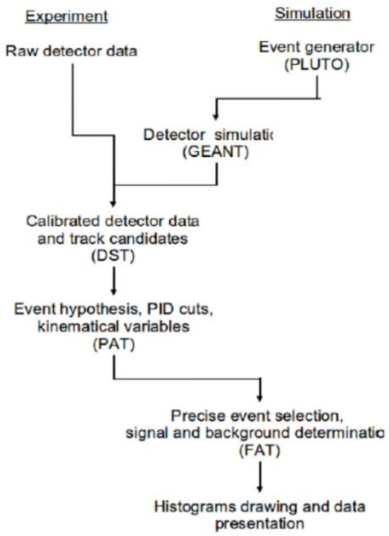

Fig 3.16 A diagram showing both experiment and simulation analysis chain.

The same specific procedure has been followed both for experimental data and the simulation. The detector data were processed to select track candidates then a hypothesis of (pe^+e^-) with selection cuts applied on identified particles. In the final step selection on missing mass, presented in section **3.5** and **3.6**, was applied followed by the subtraction of combinatorial background and extraction of the signal. In the case of simulation the first step was to simulate events by the PLUTO event generator and process the data into the GEANT [54] tool responsible for performing the simulation of interaction of particles with the detector material. The rest of the analysis chain was the same as in the experimental case, including all selection criteria discussed above.

First, a verification whether momentum distributions of the spectator agrees with the assumptions of the spectator model (section **3.2**) was done. **Fig 3.17** shows distributions of the spectator momentum for the different polar emission angles and in the invariant mass regions and $m_{e+e-} > 0.14$ GeV/c^2 compared to Monte-Carlo simulations, normalized to the same total yield in this mass region.

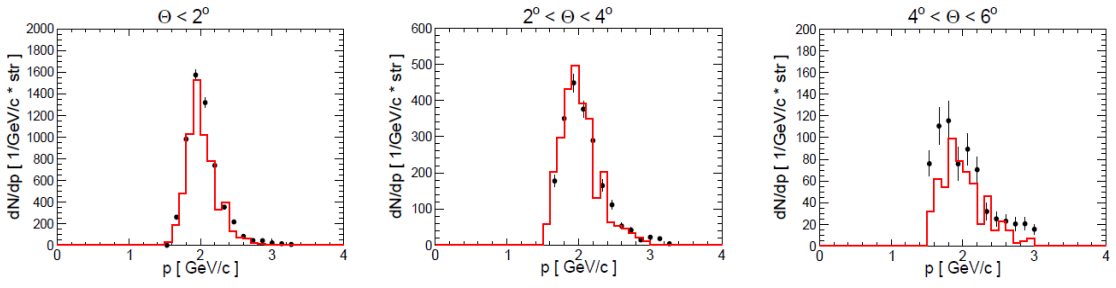

Fig 3.17 The proton spectator momentum distributions for the polar (θ) angle slices (2°, 2°-4°, 4°-6° degree).

The simulation based on the assumed spectator model reproduce shapes of the experimental data. Yet another verification of the spectator model approximation was performed by looking on the exclusive e^+e^- invariant mass for selected polar angle θ regions of the spectator emission.

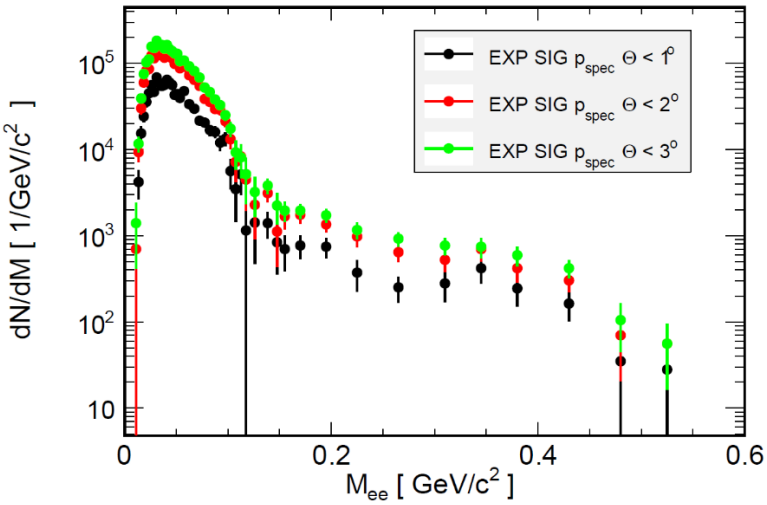

Fig 3.18 Counts in a function of the invariant mass of lepton pairs done for selected polar angle θ region of the $p_{spectaror}$.

The different regions of $\theta_{spectator}$ imposes only small variations in the distribution but quite significant in the yield (as presented in **Fig 3.18**)

Next, a comparison of the simulation with the data after the selection on the missing mass has been performed. **Fig 3.19** presents the pe^+e^- missing mass, the experimental data are overlapped with a simulation.

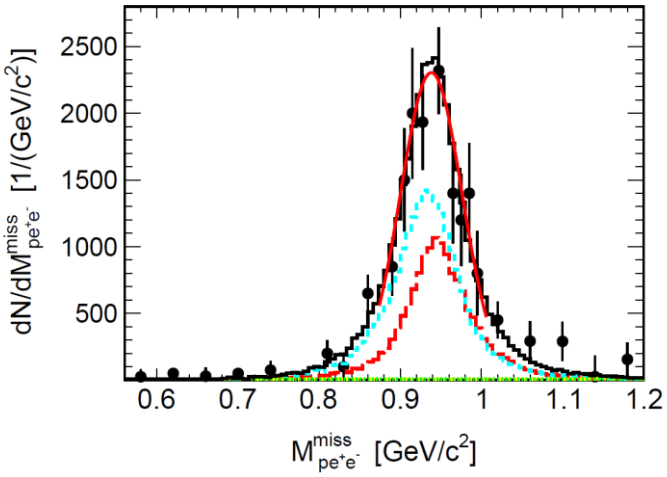

Fig 3.19 The pe^+e^- missing mass distributions for the $M_{ee} > 0.14$ GeV/c^2 obtained for the experimental data (black dots) and the simulated data sets channels 3 and 4 in model I (red dashed curve), ρ (blue dashed curve) and a sum of both (black solid curve) normalized to the same yield. A Gaussian fit to the sum of simulated components is presented by red solid curve.

Distributions presented in **Fig 3.19** have similar mean value 0.945(2) GeV/c^2 (slightly higher than a free neutron mass) and sigma 0.036(0.3) both obtained from a Gaussian fit. This clearly indicates that the simulation reproduces the momentum enhancement and the experimental yield. A selection window of 3σ around the neutron peak has been applied as presented in **Table 2**.

Missing mass selection windows (np)	
Simulation	Experiment
0.82 GeV/c^2 to 1.073 GeV/c^2	0.8 GeV/c^2 to 1.080 GeV/c^2

Table 2. Values of a selection window applied in analysis.

The contributions coming from channel 7 and 8 (model I) are minor and not even visible in the presented spectrum and therefore will be neglected in the following analysis.

The exclusive final state pnγ^* can be characterized by five independent variables which can be chosen in a number of ways. Assuming azimuthal symmetry in the production one can further reduce it to four variables. The decay of the γ^* can be characterized by another two variables. In this work the following observables have been chosen:
1) three invariant masses of the γ^* (equivalent to the invariant mass of dielectron pair $M_{e^+e^-}$), of the proton virtual photon $M_{pe^+e^-}$ and of the proton-neutron M_{pn} systems.
2) distributions of two polar emission angles defined in the Centre of Mass reference frame (c.m.s): of the proton $\cos^{CM}(\theta_p)$ and of the virtual photon $\cos^{CM}(\theta_{\gamma^*})$ and the angle describing the lepton (electron or positron) emission in the γ^* rest frame $\cos^{\gamma^*}(\theta_e)$ (helicity angle).

The experimental distributions are corrected for the reconstruction inefficiencies and are presented as the differential cross sections (obtained via normalization to proton-proton elastic scattering) inside the HADES acceptance. For the angular distributions also acceptance corrected spectra are presented.

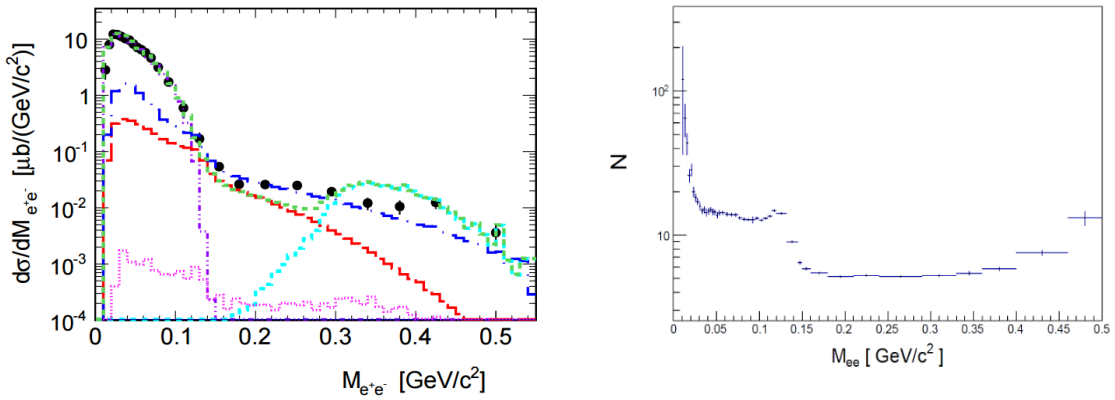

Fig 3.20 npe$^+$e$^-$ final state. Left: Differential cross section in a function of the di-lepton invariant mass compared with the model predictions [model I, model II and ρ]. The low mass region described by the π^0 Dalitz decay [model I reaction 1 and 2, purple dotted curve]. The high mas region (above the π^0) dominated by pairs coming from the Δ Dalitz decay, reaction 3 and 4 form model I (red curve). Contributions from η (magenta) decay is also present but the amount of pairs coming from the decays is minor. Dark blue curve represents the calculations obtained from the model II [31], blue dotted curve corresponds for leptons coming from the ρ [32]. Right: a plot, showing the efficiency correction (correction factor (Z) in a function of M_{ee}).

As already discussed above, the dielectron invariant mass distributions is very sensitive to the coupling of the virtual photon to the ρ meson. Therefore the starting point of presentation of the data is **Fig 3.20** which presents the dielectron invariant mass distribution and comparison to the simulated distributions. The differential cross section is dominated at low invariant masses by the pn→pn($\pi^0 \rightarrow \gamma e^+ e^-$) Dalitz decay which could not be completely eliminated by the selection on the pe^+e^- missing mass (section **3.6**) due to the detector mass resolution. This contribution is well described by our simulations, confirming assumed cross section of the one pion production.

The distribution for larger invariant masses, $M_{e+e-} > M_{\pi 0}$, is dominated by the true pne^+e^- events (as also proven by the respective missing mass distribution in (see **Fig 3.19**) which is of the main interest for this study. In this mass region the dielectron yield is described to some extent by the model I (green curve) with indicated components: Δ(red-dashed curve), η (magenta-thin dotted) Dalitz decays and at higher masses dominant ρ contribution (cyan-dotted) originating from the double Δ fusion. More closer inspection, however, reveals that the Δ Dalitz alone cannot describe the yield in the $0.14 < M_{e+e-} < 0.28$ GeV/c^2 mass region, what in fact is not surprising since some space must be left for the nucleon-nucleon bremsstrahlung. On the other hand the ρ overshoots the measured yield at higher masses, even stronger than in the case of the inclusive data [32].

The simulation based on the model II (dark blue thick solid curve) gives a better description of the data, except the largest invariant masses where it slightly underestimates the measured yield. Hence, one can conclude that the enhancement at high masses, due to the contribution from the internal charged pion line and electromagnetic form-factor of a pion proposed for the explanation of the inclusive spectrum is supported by the exclusive data. The exclusive invariant mass distribution can be also compared to the ppe^+e^- final state measured by the HADES at the same beam energy (section **1.2** in **Fig 1.7**). Since the latter one is well described, as discussed in section **1.2** (see **Fig 1.7**) by various independent calculations it can serve as the reference for the identification of some additional contribution appearing solely in the pne^+e^- final state. **Fig 3.21** (left) shows the respective comparison of the two invariant mass distributions normalized to the cross section of the π^0 measured in the np → npe^+e^-. It reveals apparently a different shape above the pion mass. The right panel shows the ratio of both differential cross sections (not normalized as in **Fig 3.21** left) as a function of the invariant mass in comparison to three different simulations. The errors bars plotted for the data and the simulations are statistical only.

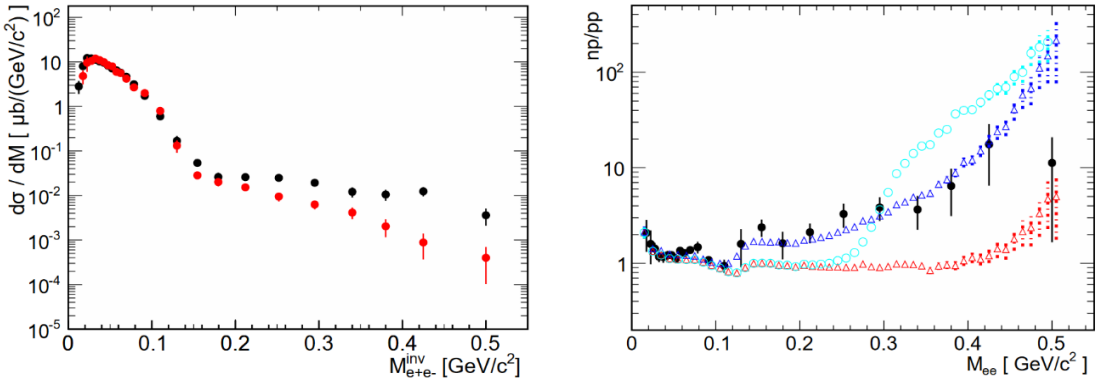

Fig 3.21 Exclusive invariant mass spectra for np (black) compared with pp (red, pp data scaled to the same $\sigma_{np}(\pi^0) = \sigma_{pp}(\pi^0)$) yield. (right panel) Ratio of np/pp (black dots) obtained from the experiment compared with various model simulations (colored symbols). (detailed description see text)

First, let's note that the measured value of the ratio of two cross sections in the π^0 region in the HADES acceptance and inside the $M_{pe^+e^-}$ missing mass window amounts to: $\sigma_{\pi^0}^{np}/\sigma_{\pi^0}^{pp} = 1.48(\pm 0.24)$ and is well reproduced by the simulations. Though the ratio of the cross section in the full solid angle is about 2, the one measured inside the HADES acceptance is smaller because it is reduced by larger acceptance for the ppe^+e^- final state as compared of the pne^+e^- due to the fact that two protons can be detected in pp collisions.

Above the pion mass the ratio clearly demonstrates apparent excess of the dielectron yield in the exclusive pne^+e^- channel over the one measured in the pp collisions. Hence, it indicates additional production process which is apparently absent in the pp reactions, as proposed in the discussed models. The predictions of the respective simulations are shown by blue open triangles (model II) and cyan open circles (model I). As already visible in the comparison to the dielectron invariant mass distribution in **Fig 3.20**, the calculation of Shyam and Mosel describe the data above the π^0 in a better way.

In order to eliminate more trivial effects due to different phase space volumes available in the pp and the quasi-free np collisions the ratio of the cross sections of the Δ channels in both reactions (red triangles) has been plotted as well. As one can see, indeed some enhancement can is seen but only at the limits of the available phase space. Hence, the conclusion is that these effects cannot explain the measured enhancement.

Fig 3.22 shows the two other invariant mass distributions: of the pe^+e^- (left) and pn (right) systems. Both distributions are plotted for the mass of a virtual photon $M_{e^+e^-} > 0.14$ GeV/c^2 and are compared to the models II and I, where the latter is separated into the contributions: Δ, ρ (same color code as in **Fig 3.20**).

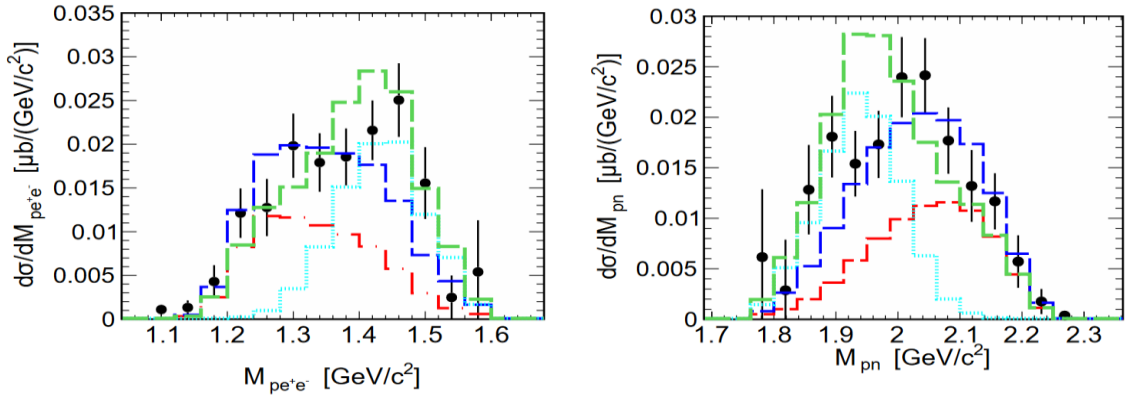

Fig 3.22 Differential cross section in a function of the $\mathbf{pe^+e^-}$ (left) an **pn** (right) invariant mass (M_{ee}>0.14 GeV/c^2), major contributions coming from model I (red), Shyam model (dark blue) and ρ (light blue) are presented. The green curve presents a sum of the model I and the ρ.

As one could expect, the distribution at low $M_{pe^+e^-}$ is dominated by low mass dielectrons, originating mainly from the Δ decays (note that observed shape in the simulation is due to an interplay between $\Delta^+ \rightarrow pe^+e^-$ and $\Delta^0 \rightarrow ne^+e^-$ decays, both contributing with same cross section) and at higher masses by the ρ-meson channel. On the other hand, the invariant mass of pn system is dominated at low masses by the ρ contribution, which in model I overshoots slightly the data and leads to some shift of the mean position. In general, one can however see, that the high-mass enhancement visible in the e^+e mass spectrum is consistently reflected in the shapes of two other invariant mass distributions. In the discussion of the angular distributions separately two bins of the dielectron invariant mass:

$0.14 < M_{e^+e^-} < 0.28$ and $M_{e^+e^-} > 0.28$ GeV/c^2 were considered. The selection of the two mass bins is dictated by the comparison to the calculations which point to two possible different production regimes, in particular the second bin dominated by the ρ-like contribution.

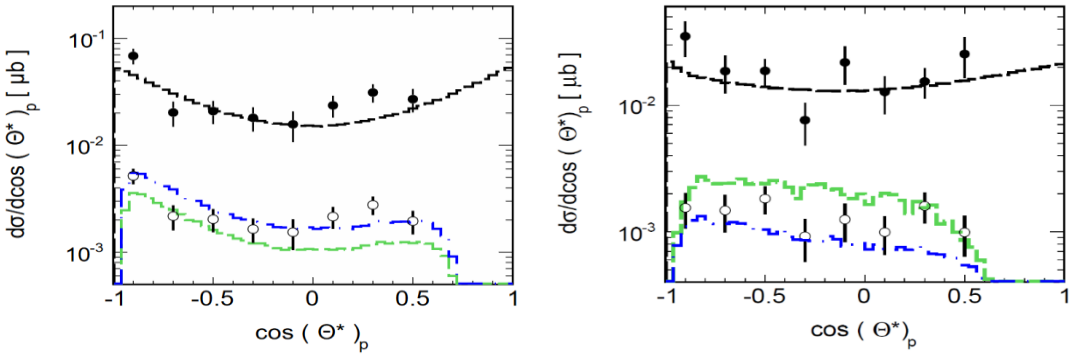

Fig 3.23 Differential cross sections for the dilepton production in pne$^+$e$^-$ channel as a function of the proton emission angle in the c.m.s of the reaction: for the $0.14 < M_{e^+e^-} < 0.28$ GeV/c^2 (left) and $M_{e^+e^-} > 0.28$ GeV/c^2 (right) in the HADES acceptance (open symbols) and the full solid angle (full symbols). The dashed curves displays predictions from the simulations in the full solid angle normalized to the experimental yield while the dotted ones inside the detector acceptance for the model I (green curve) and II (blue curve) respectively.

Fig 3.23 displays the differential angular distributions of the proton in the c.m.s. The distributions measured inside the HADES acceptance are shown by the open symbols while the acceptance corrected ones by the filled symbols. The left panel shows the distribution for the smaller while the right one for the larger dielectron invariant masses (with respect to the pion mass). The dotted curves show distributions obtained from the simulation with the models I (green curve) and II (blue curve) inside the HADES acceptance. Both simulated distributions differ in magnitude but have similar shape because of same angular distributions assumed in the simulation, as shown by the dashed curve (note that the model I is dominated in this mass region by the bremsstrahlung contribution). The distributions shown for the full solid angle are normalized to the experimental yields obtained after acceptance corrections. The acceptance correction factors applied to the data have been calculated as a two-dimensional function of the respective angle and the dielectron invariant mass using the above described models. The respective correction matrices are presented below in **Fig 3.24**.

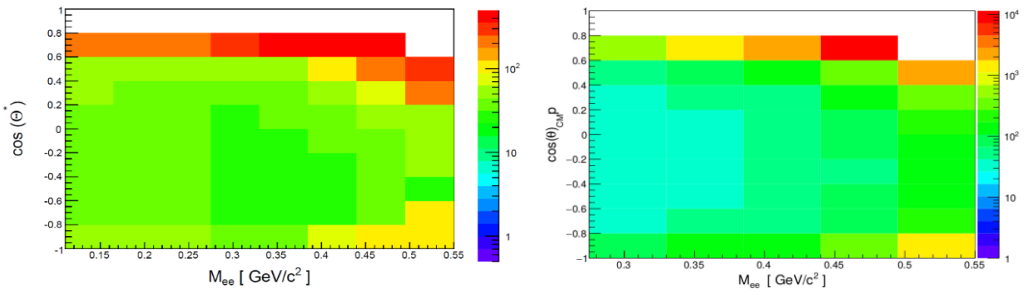

Fig 3.24 Corrections of cos(θ) of a proton in the c.m.s frame in a function of the invariant mass. Correction on the left obtained from the model I, the right one comes from the model II.

The correction matrices in **Fig 3.24**, show a strong increase of the factor at the edge of the distribution . In order to avoid such big correction values a cut on the detector fiducial volume $\cos(\theta) < 0.6$ and $M_{ee} < 0.5$ GeV/c^2 has been imposed. It is important to notice as well that the extrapolation carries an additional mean statistical error of 5%. For lower invariant mass bins (0.14 GeV/c^2 < M_{ee} < 0.28 GeV/c^2) the correction shown in **Fig 3.24** (left) was applied (results are indicated in **Fig 3.23** right, by black full dots). It was obtained from the Δ simulation (channel 3 and 4 presented at the begging of this section) by generating a Monte-Carlo data sample and diving the result by the corresponding data but within HADES acceptance after reconstruction (4π/RECO). As for higher invariant mass bins (M_{ee}>0.280 GeV/c^2) a correction matrix shown in **Fig 3.24** (right) was used. It was obtained in an identical way as previous, but for events taken form Bashkanov model [32] (results are shown in **Fig 3.23**).

Returning to the main point, as can be seen from (see **Fig 3.20**), the low mass bin is dominated in the simulation by the Δ Dalitz while the ρ-meson contribution determines dielectron production in the higher mass bin. In the first mass bin, the angular distribution exhibits clear anisotropy (see **Fig 3.23** left). It is accounted for in the simulation by the applied angular distribution of the Δ production known from pp data, as discussed in details in [19]. The strong forward-backward peaking of the distribution signals the importance of the t-channel exchange in the resonance production. There is an indication of some enhancements above the simulation in the npe^+e^- channel for the forward emitted protons, unfortunately it is cut at small angles by the HADES acceptance. It might indicate importance of a charge exchange reaction of the type $np \rightarrow pne^+e^-$ which leads to a proton emission at forward angles. For the higher masses the angular distribution is more isotropic and is described rather well by both simulations which again exhibit similar characteristics. In the model I, the alternation of the distributions indicates the increasing importance of larger momentum transfer needed for production of the virtual photon with larger mass.

Fig 3.25 present similar distributions (and for same the invariant mass bins) to the discussed above but for the virtual photon. The distributions are also strongly modified by the HADES acceptance, particularly in the backward region. A deviation from the isotropic emission, assumed in the simulation, seems to be visible, particularly for the smaller mass bin. The acceptance corrected distributions are, as in the previous, case normalized to the experimental cross sections. The correction matrices are made in an identical way as before.

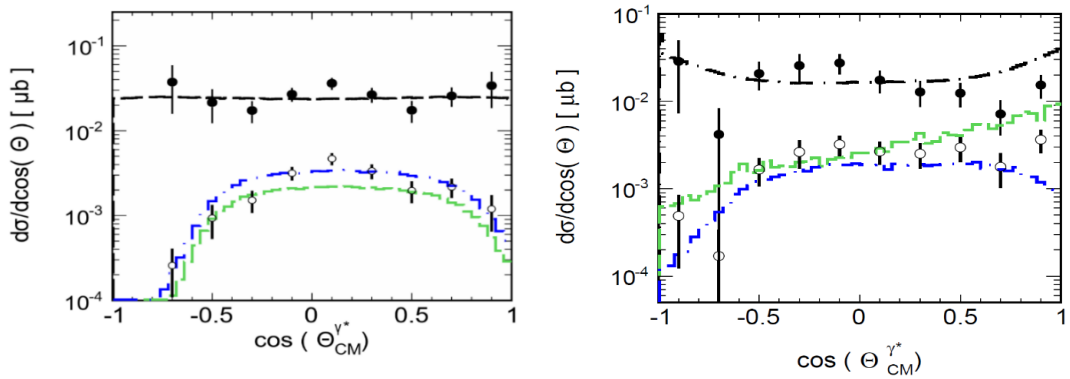

Fig 3.25 Distributions of emission angle of the virtual photon in the c.m.s for 0.14 < M_{e+e} < 0.28 GeV/c^2 (left) and M_{e+e-} > 0.28 GeV/c^2 (right)**.** Black dots represent experimental data corrected by the efficiency and the acceptance of the HADES spectrometer, black open dots show the data in the acceptance, green and black dashed curves represent the simulation in the acceptance and the full solid angle for the model I and the model II. The blue curve presents the calculations form the Shyam model [31].

Distributions of the leptons in the rest frame of the virtual photon, so called helicity frame will be presented next. These observables are predicted to be particularly sensitive to underlying reactions process [38]. Indeed, for a pseudo-scalar particle, like the a pion or the eta mesons, and their Dalitz decay to γe^+e^- the angular distribution of the electron (or positron) with respect to direction of the virtual photon in its rest-frame is predicted to be proportional to $1+B\cdot\cos^2(\theta_e)$. This predictions were confirmed in measurements of the exclusive pion and eta meson decays in proton-proton reactions [19]. B denotes the anisotropy of the distribution (B = 1 for the pseudo-scalar mesons).

For the Δ Dalitz decay the situation is more complex since the angular distribution depends on the spin density matrix, or in other words spin alignment of the Δ, which in nucleon-nucleon collisions might be non-zero. However, assuming no polarization of the Δ isobar and a dominance of the magnetic transition in the $np\rightarrow Ne^+e^-$ process the authors of [38] arrive to the same distribution as for the pseudo-scalar mesons. The situation is even more complex for the nucleon-nucleon bremsstrahlung process and only predictions based on the so called Photon Soft Approximation exist [38]. According to this model, the respective angular distributions show at our energies only small anisotropy with some dependence on the dielectron invariant mass. On the other hand, the angular distribution of leptons from the ρ-meson decay from the pion annihilation, measured with respect to direction of the pion in the virtual photon rest frame, has a strong anisotropy, i.e. $1 - B\cdot\cos^2(\theta_e)$, opposite of that expected for the Δ Dalitz decay.

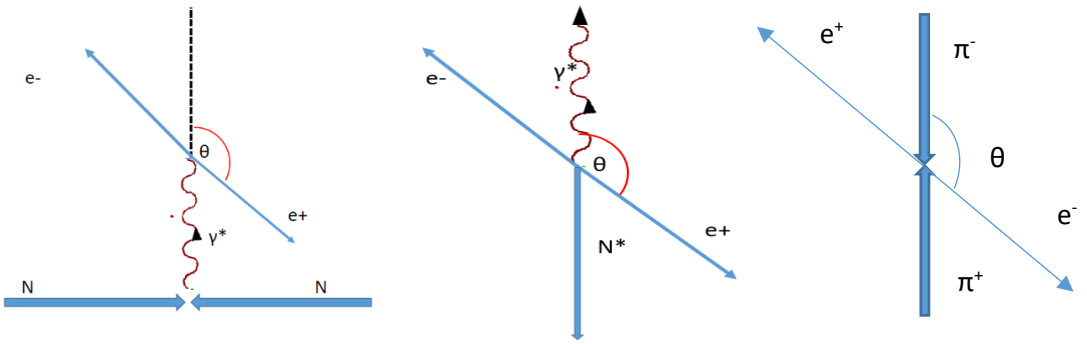

Fig 3.26 Diagrams showing a representation of the pseud-helicity (left) and helicity (right). In the first case on the left the angle between the lepton and virtual photon is calculated in the virtual photon rest frame. In the second situation (middle diagram) the calculations are done in the N* rest frame. The third diagram (right) shows the calculation with respect to the charge meson exchange line.

Fig 3.26 shows the different ways of calculating the helicity angle used in the results presented below. In the first case (left) the angle between the γ* and the lepton (positron or electron) is calculated in the virtual photon rest frame defined in the CM of collisions. In the second case (middle) the γ* rest frame is defined in the resonance ($p(n)e^+e^-$) decay frame. This scenario is appropriate for the investigation of the pairs originating from a resonance decay. Finally the third scenario (right) is defined as in the first case but the angle of the electron is calculated with respect to the vector of the exchanged momentum between two nucleons in the reaction. The latter one would be more appropriate for the pair production from the exchange charge meson line. This different cases correspond to various possible sources of the pair production which will be examined in the analysis.

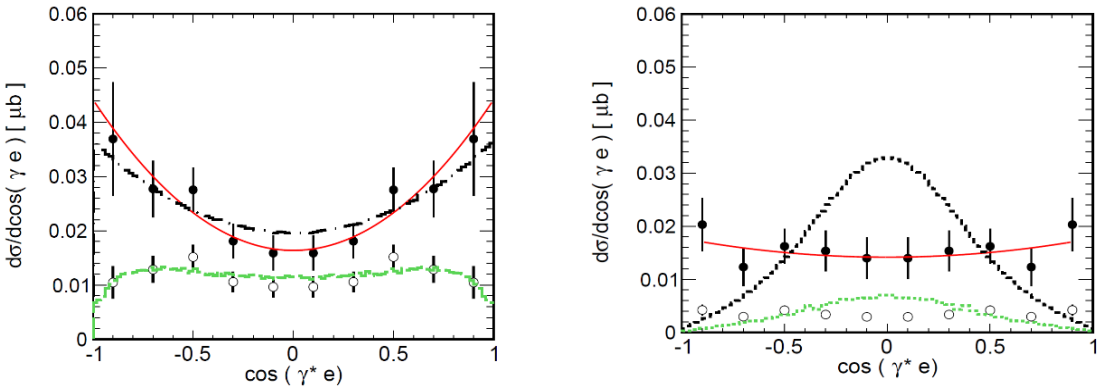

Fig 3.27 Angular distributions of the leptons in the rest frame of the virtual photon calculated with respect to the reconstructed γ* direction and for dielectrons with the mass $0.14 < M_{e^+e^-} < 0.28$ GeV/c^2 (left) and $M_{e^+e^-} > 0.28$ GeV/c^2 (right). The open symbols present the experimental data inside the HADES acceptance (multiplied by a factor 5) while the full symbols shows the data corrected for the acceptance. The dashed curves display predictions from the simulations in the full solid angle and in the HADES acceptance normalized to the experimental distributions. The curve shows a fit with a function $A(1 + B\cdot\cos^2(\theta_e))$. A is the normalization factor.

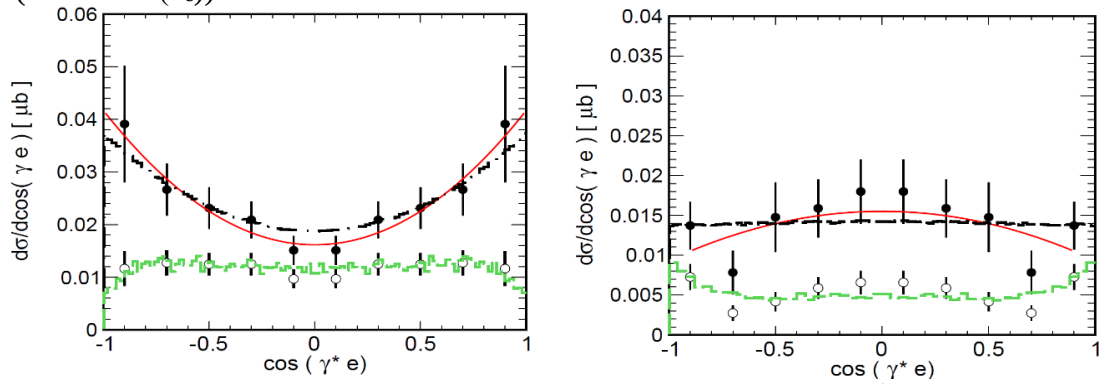

Fig 3.28 Angular distributions of the leptons in the rest frame of the pe^+e^- and virtual photon calculated with respect to the reconstructed γ* direction and for dielectrons with the mass $0.14 < M_{e^+e^-} < 0.28$ GeV/c^2 (left) and with respect to the direction of the charged pion exchange for dielectrons with $M_{e^+e^-} > 0.28$ GeV/c^2 (right). The open symbols presents data inside the HADES acceptance (multiplied by factor 5) while the full symbol shows data corrected for the acceptance. The dashed curves display predictions from the simulations in the full solid angle and within the HADES acceptance normalized to the experimental distributions. The solid curve shows a fit with a function $A(1 + B\cos^2(\theta_e))$.

Fig 3.27 presents the respective helicity distributions for the experimental data calculated in the first scenario (see **Fig 3.26** first plot form the left) and the two bins of the dielectron invariant mass. The distributions provide a symmetric distribution over the electron and the positron emission directions in the rest frame of the virtual photon. The distribution has been corrected for the acceptance and reconstruction inefficiency by means of the respective two dimensional functions calculated by means of the Δ simulation (lower mass bin) and the Bashkhanov model (higher mass bin) shown in **Fig 3.29**. For the $M_{e^+e^-} > 0.28$ GeV/c^2 a fiducial volume was limited by a cut $M_{e^+e^-} < 0.5$ GeV/c^2 in order to avoid too large correction factors.

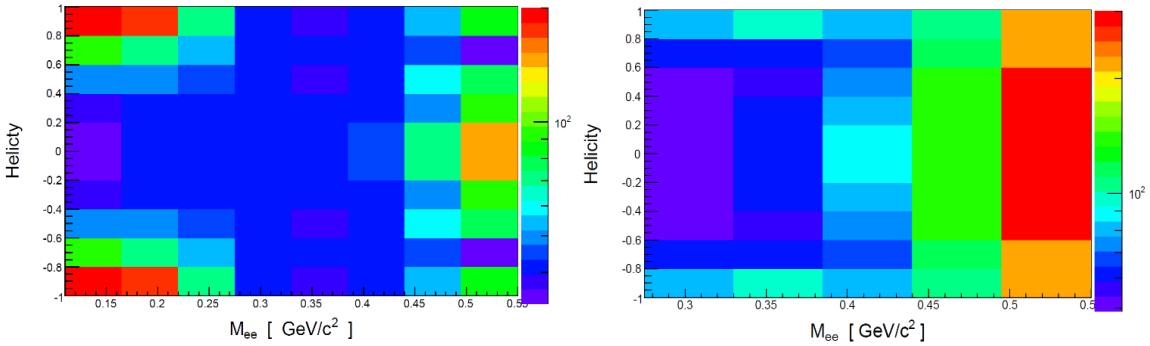

Fig 3.29 Acceptance and reconstruction inefficiency correction factors as a function of the helicity and the invariant mass calculated with the Δ simulation (left) and the Baskhanov model (right).

As for the results presented in **Fig 3.28** the helicity distribution were calculated in a following way, first plot form the left presents a helicity distribution calculated for the lower mas bin ($0.14 < M_{e^+e^-} < 0.28$ GeV/c^2) in the second way of the boost (as described above) (see **Fig 3.26** middle plot), second plot calculated for higher mass bin ($M_{e^+e^-} > 0.28$ GeV/c^2) the calculation has been done for the third way of the boost (see **Fig 3.26** plot on the right). The correction matrices used for those calculations were obtained in an identical way as for previous case.

The anisotropy values (B) obtained from fits using a function $A(1 + B\cos^2(\theta_e)$ give following results for: **Fig 3.27** B = 1.69(±0.54) (left), B = 0.25(±0.36) (right) and B = 1.58(±0.51) (left) and B = -0.5(±0.25) (left) for the **Fig 3.28**. As one can see the fits for the lower invariant mass clearly show anisotropy parameters which are in agreement with the one expected for the Δ decay. One can also see that choice of the reference frame and respective angle is important for the higher mass bin.

For the left panel (bin with the smaller masses, **Fig 3.28**) the distribution has been calculated with respect to γ^* (in pe^+e^- rest frame) direction while for right panel (bin with the larger masses) with respect to the direction of the charged pion exchange. The latter one has been calculated as the direction of the vector constructed from the difference between the vectors of the proton and the neutron and boosted o the rest frame of the virtual photon. The open symbols present data within the HADES acceptance while the full symbols show the data corrected by the acceptance. The dashed curve displays predictions from the simulations in the full solid angle and within the HADES acceptance. Simulated distributions are normalized to the respective experimental yield for a better comparison of the shape. The solid curve shows a fit with a function $A(1+B\cos^2(\theta_e))$. While for the lower mass bin the data confirm the distribution expected for the Δ, B = (1.59)(±0.51) (in fact it almost overlays with the simulated distribution) the higher mass bin shows the opposite anisotropy, B = -0.5(±0.25) and suggests, within available statistics, to the dominance of ρ decay from the exchanged charged pion line.

3.9 Conclusions

1. The presented studies of the exclusive spectra for the $np \rightarrow npe^+e^-$ provide several important findings. The invariant mass distribution of the pairs is well described in the π^0 mass region by the simulation while the high mass region is underestimated by the single Δ and $\Delta\Delta$ Dalitz decay (model I).
2. There is a significant difference in pair production between the np and the pp collisions measured at the same beam energy (**Fig 3.21**). The ratio between the two cross section indicates an important role of the intermediate ρ-meson production and is closest to the model of bremsstrahlung production in [31].
3. Contribution coming from the ρ^0 decay calculations overestimates the data by a factor of 2 in the $e^+ e^-$ invariant mass (**Fig 3.20**).
4. The study of helicity tells that there is a significant contribution of lepton pairs coming from Δ Dalitz decay in the low mass bin ($0.14 < M_{e^+e^-} < 0.28$ GeV/c^2) (**Fig 3.27** and **Fig 3.28** left plot)
5. The results of helicity distributions for the high mass region, presented in **Fig 3.28,** are in agreement with the expectations discussed in [32] and point to the $\pi^+\pi^-$ annihilation as the main source of pairs.
6. The study of the model I leads to conclusion that the simulation can reproduce to some extent the shape (within the error) of the distribution of $\cos(\theta)$ of proton in the c.m.s and the virtual photon distributions in the higher mass region.
7. Virtual photon distributions are described by the simulation and are isotropic in both regions.

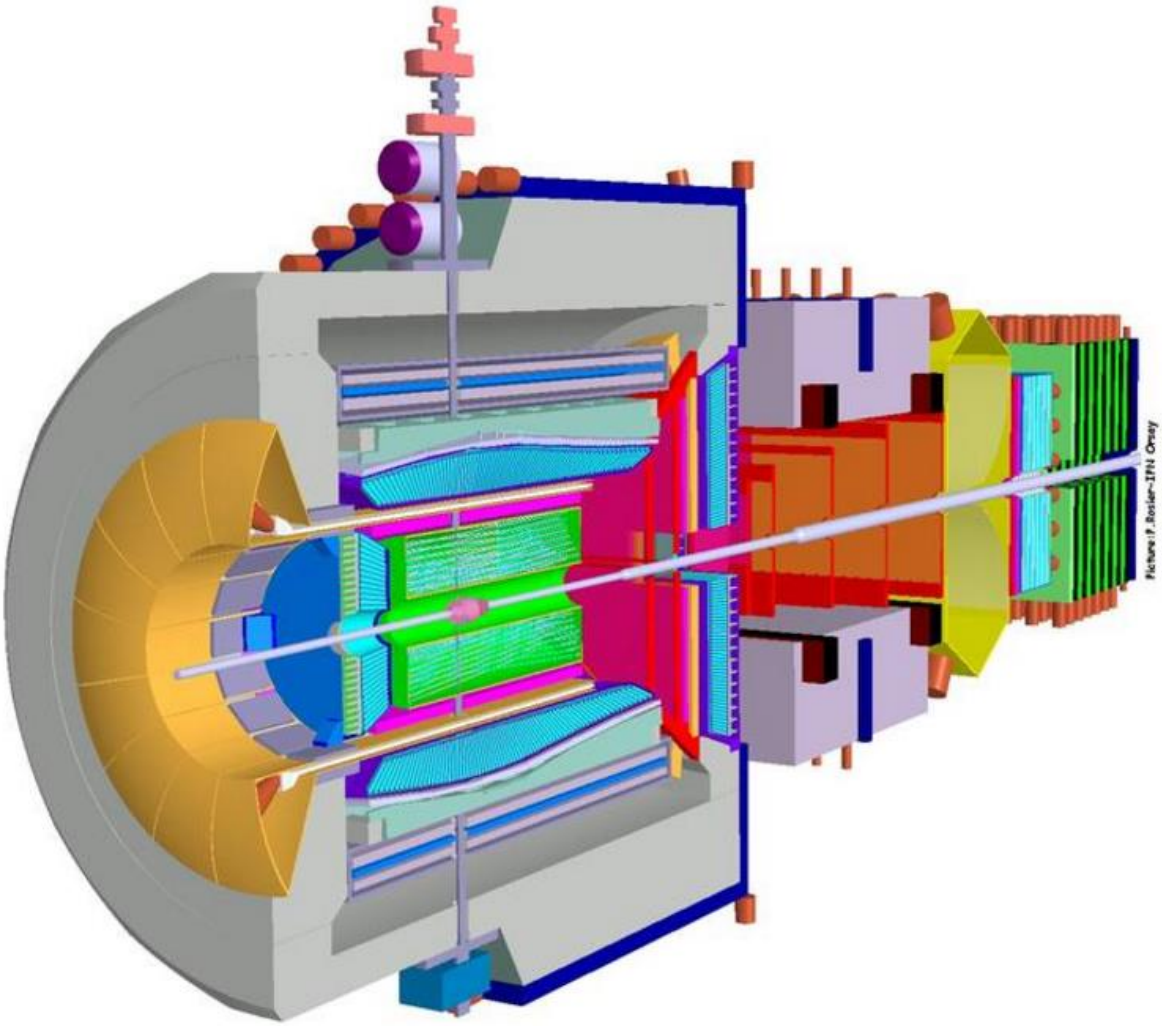

4. Introduction to PANDA@GSI physics program

FAIR stands for "Facility for Antiproton and Ion Research". It is a particle accelerator facility which is under construction in Darmstadt, Germany. FAIR will give the possibility to conduct research in five fields: physics of the structure of atomic nuclei, physics of antimatter, physics of nuclear matter under extreme conditions, plasma physics, physics of the atomic shell. FAIR will be built next to the existing GSI research center and will use its accelerators as injector [56]. The author will now address two points of the physics program of PANDA experiment related to physics of proton-antiproton annihilation.

4.1 Charmonium as a tool in the study of strong interactions.

Charmonium has been discovered in 1974 [57], and form this point it was a “probe” in the understanding of the strong interactions. The mass of c quark is high (~1.5 GeV/c^2) hence an ideal candidate in the study of dynamical properties of the bound quark ($c\bar{c}$)-charmonium. Up to now most of the studies have been done via the non-relativistic potential models, in which the functional form of the potential is assumed to reproduce the asymptotic behavior of strong interactions. The parameters in those models are obtained by comparison with the data. Recently, a rapid progress in calculations using formulation of the QCD on lattice (LQCD) allows also studies of the mass spectrum of bound quark, quark-gluon (hybrid) and gluon-gluon (glueballs) systems.

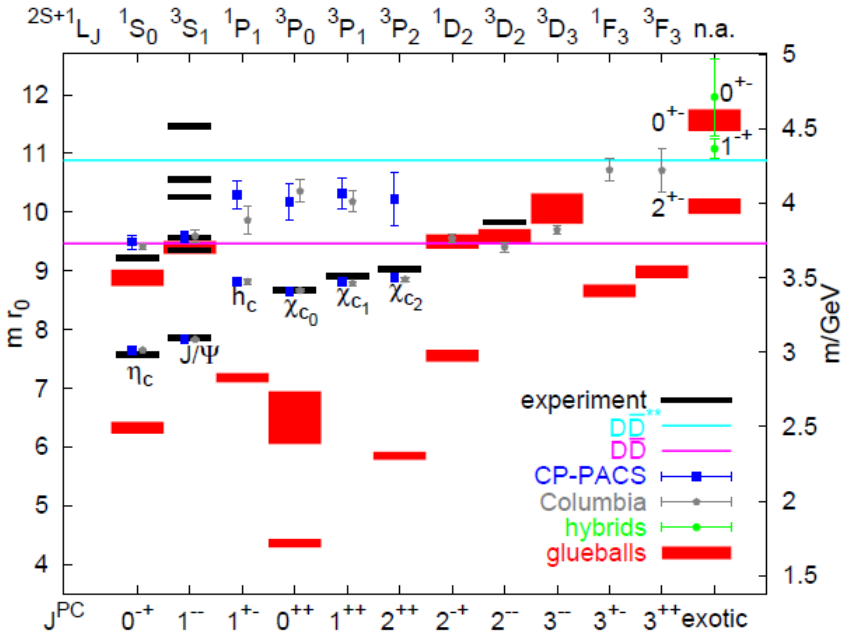

Fig 4.1 Presentation of the predictions obtained by the LQCD in charmonium mass region and the experimentally discovered states [58].

Fig 4.1 presents the comparison of the currently known masses, spin (S), angular momentum (L) and quantum numbers of states in the charmonium mass region with predictions of various calculations. The mr_0 is a dimensionless variable where the $r_0 \approx 0.5$ fm, it comes from $r^2\, dV(r)/dr = 1.65$ for $r = r^0$ where V(r) is the potential energy between two static quarks (see **Fig 4.2**). The CP-PACS and Columbia calculations are presented as well [86, 87, 88] in **Fig 4.1**.

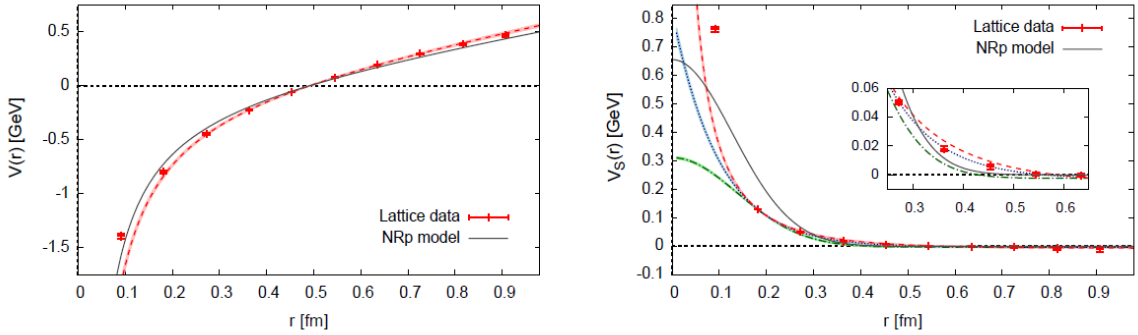

Fig 4.2 Spin independent (left) and spin-spin (right) charmonium potential calculations (dots), the dashed curve represents results from the fit [91].

As one can see after the discovery of the J/ψ, many new states were discovered. The majority of charmonium states are well described by potential models, but there are also other states which nature remains controversial. What is mostly described at the present moment, is the spectrum below the so called "open charm threshold", presented by a purple line in **Fig 4.1** (3.73 GeV) but note that there are also exotic states such as glueballs and hybrid states which are predicted by the calculations but not yet confirmed by experiment. The search for the latter one is one of the goals of the PANDA physics program. On the other hand, there are many new states that have been discovered above the open charm threshold which nature remains "controversial". They are labelled as "X,Y,Z" and summarized according to production mechanisms in **Table 1.1**.

$(e^+ + e^-)_{\mathrm{ISR}} \to (c\bar{c})$	$b \to s(c\bar{c})$	$e^+ + e^- \to J/\psi + (c\bar{c})$	$\gamma\gamma$ fusion
$Y(4260)$ $Y(4008)$ $Y(4320)$ $Y(4664)$ $X(3773)$	$X(3872)$ $Y(3940)$ $Z^+(4430)$ $Z^+(4051)$ $Z^+(4248)$ $Y(4140)$	$X(3940)$ $X(4160)$	$Z(3930)$ $Y(3915)$ $Y(4350)$

Table 1. 1 A list of the states labeled as "XYZ" with their corresponding production diagrams, taken from [89].

The first discovered state was the X(3872) by the Belle experiment [100] in 2003 via $X(3872) \rightarrow {}^{J}/_{\psi}\,\pi^{+}\pi^{-}$ decay. What's more the CDF group [90] has proven that the di-pion comes from the decay of the $\rho \rightarrow \pi^{+}\pi^{-}$, such evidence shows a isospin violation and thus this state cannot be identified as a conventional charmonium. What is also very important that the X(3872) has its mass pole very close to the sum of $D^{0}D^{*0}$ meson mass, thus making it a candidate for the for a molecular structure. The X(3872) was also observed in ${}^{J}/_{\psi}\,\pi^{+}\pi^{-}\pi^{0}$ and $D^{0}\overline{D^{0}}$. The Z(3930) was seen as a peak in the $D\overline{D}$ invariant mass (see **Table 1.3**) in $\gamma\gamma$ collision, as for the Y(3940), the first observed decay mode was $Y(3940) \rightarrow \omega\,{}^{J}/_{\psi}$.

Resonance	Mass [MeV/c^2]	Width [MeV]	$I^{G}(J^{PC})$	Main Decays
$\psi(3770)$	3773.15±0.33	27.2±1.0	$0^{-}(1^{--})$	$D\overline{D}$ $\gamma\chi_{cJ}$
$\chi_{c2}(2P)$	3927.2±2.6	24±6	$0^{+}(2^{++})$	$D\overline{D}$
$\psi(4040)$	4039 ±1	80 ±10	$0^{-}(1^{--})$	$D\overline{D}$ $D^{*}\overline{D}$, $D^{*}\overline{D^{*}}$
$\psi(4160)$	4153±3	103±8	$0^{-}(1^{--})$	$D\overline{D}$ $D^{*}\overline{D}$, $D^{*}\overline{D^{*}}$
$\psi(4415)$	4421 ±4	62±20	$0^{-}(1^{--})$	Hadrons $D^{0}D^{*-}\pi^{+}$

Table 1.2 States of $c\bar{c}$ confirmed as conventional [60] .

Most of the newly discovered states are very close to the $D\overline{D}$ threshold and they do not seem to apply to the conventional charmonium characteristics because of their quantum numbers, their charge or their narrow width. There are several theoretical explanations of these XYZ states as:

- Conventional charmonium (known states are listed in **Table 1.2**)
- Tetra-quark system
- Molecular states
- Charmonium hybrids
- Hadrocharmonium
- Threshold effects occurrences

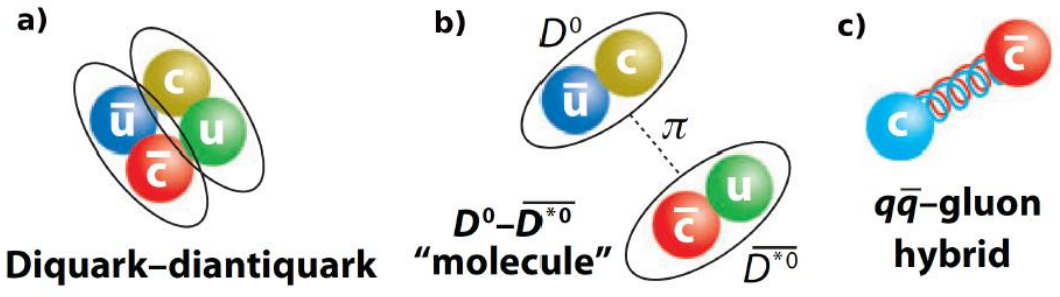

Fig 4.3 XYZ possible states: a) schematic of a tetra quark state, b) molecular $D\overline{D}$ sate and c) gluon hybrid state [60].

The tetra quark system, presented in **Fig 4.3** a), consists of four quarks tightly bound, as described for example in [61]. The idea itself is quite old and dates to the mid-seventies. It was assumed that a(980) and f(980) [62] can be $K^- K^+$ bound the same way as nucleons are bound together in the nuclei. Nonetheless the tetra-quark system can be described as a di-quark anti-di-quark system in which quarks are grouped into color-triplet scalar and vector systems and where the spin-spin is the dominant interaction. Those states can be identified from the typical conventional states if those multiples include participants with a charge Q = 0.

Candidates laying close to the $D\overline{D}$ production threshold, like the X(3872), can also be viewed as a molecules of two charged mesons which are weakly bound via a pion exchange. This is presented in **Fig 4. 3**, case b). Calculations assuming this situation are discussed in [63] in the framework of the coupled channels and include several meson-anti meson channels and several $q\bar{q}$ states. In general the idea includes a bound mechanism such as: short distance exchange of a quark or a gluon and the other, a long distance exchange of a pion.

The charmonium spectrum is populated by narrow states minimizing the chance of mixing. This situations favors searches for hybrid states (case c). In a general picture the hybrid can be described in the framework of the LQCD as a quark moving in adiabatic potential produced by gluons. The width of the hybrid can be as narrow as 20 MeV [64] for the lowest state, if the width and the decay modes of it depends sensitively on the mass. It is assumed that the decay to open charm is forbidden or at least suppressed, hence a slow decay into hidden charm is most probable.

Hadro-charmonium is believed to have a separation of heavy and light degrees of freedom separated by their size. It can be referred as a compact and colourless charmonium placed inside a large area of light hadronic matter [65]. The interaction between the charmonium core and its surrounding light hadronic shell is described by the QCD in analogy to the van der Waals force [66].

The physics program of PANDA detector addresses spectroscopy of exotic states near the $D\overline{D}$ threshold. It is expected that $p\bar{p}$ reactions are advantageous in comparison to positron-electron annihilation because any exotic quantum numbers can be populated in the production. Furthermore, due to an excellent resolution of the anti-proton beam (see chapter **4.4**) the width of the states can be measured by the beam momentum scan more precisely (even with tens of keV) as compared to decay experiments which are limited by the detector resolution. However, since most of the decay channels include open charm states ($D\overline{D}$)- see **Table 1.3** it is important that the detector has a sufficient acceptance for the detection of those states. This is a motivation for this work, to study a bench-mark reaction $p\bar{p} \rightarrow X \rightarrow D\overline{D}$ with a special emphasis on the importance of the Forward Spectrometer, which main component namely the tracking systems is under development at the Jagiellonian University in Kraków.

State	Mass(MeV)	Width(MeV)	Decay mode	Process
$Z_c(3900)^{\pm}$	3899.0±3.6 ±4.9	46±10 ±20	$\pi^{\pm}J/\psi$	$e^+e^-\to\pi^+\pi^-J/\psi$
$Z_c(3900)^0$	3894.8±2.3±2.7	29.6±8.2±8.2	π^0J/ψ	$e^+e^-\to\pi^0\pi^0J/\psi$
$Z_c(3885)^{\pm}$	3883.9±1.5±4.2 [single D tag] 3884.3±1.2±1.5 [double D tag]	24.8±3.3±11.0 [single D tag] 23.8±2.1±2.6 [double D tag]	D^0D^{*-} D^-D^{*0}	$e^+e^-\to\pi^+D^0D^{*-}$ $e^+e^-\to\pi^+D^-D^{*0}$
$Z_c(4020)^{\pm}$	4022.9±0.8 ±2.7	7.9±2.7 ±2.6	$\pi^{\pm}h_c$	$e^+e^-\to\pi^+\pi^-h_c$
$Z_c(4020)^0$	4023.9±2.2 ±3.8	fixed	π^0h_c	$e^+e^-\to\pi^0\pi^0h_c$
$Z_c(4025)^{\pm}$	4026.3±2.6±3.7	24.8±5.6±7.7	$D^{*0}D^{*-}$	$e^+e^-\to\pi^+(D^*\bar{D}^*)^-$

Table 1. 3 List of known Z states and there decay modes [92].

The other reaction which has been studied is connected to electromagnetic structure of the hyperons, a subject which is an extension of the HADES physics programme related to baryon eTFF discussed in the first chapter of this thesis. This subject is presented in the next chapter.

4.2 Probing the quark- gluon structure of hyperons

At large momentum transfer measuring electromagnetic form-factors can be an important tool in understanding the quark gluon structure. One of the first proposals made by Cabibbo and Gatto in 1961 [67] was to study the electromagnetic form-factors a low $Q^2 < 0$ in the time like region by e^+e^- annihilation. Measurements of the form-factors for p, Λ, ∑ and Ξ were performed in $e^+e^-\to B\bar{B}$. In general for hyperons, as for non-strange baryons, with J > ½ one can define a set of three form-factors G_M, G_E, G_C representing a magnetic, electric, coulomb transition form-factors. A relation between the cross section and the form-factors in this case, presented in a formula [68].

$$\sigma_0^B = \left(\frac{4\pi\alpha^2\,\beta_B}{3s}\right)[|G_M^B(s)|^2 + (2m_B^2/s)|G_E^B|^2] \qquad (23)$$

where:

β_b- baryon velocity in the c.m.s.

s- energy in the c.m.s.

α^2- fine-structure constant squared

m_B- mass of the baryon.

The recent results of such measurements obtained by the CLEO collaboration [69] are presented below in **Fig 4.4**, for the assumed relations between form-factors.

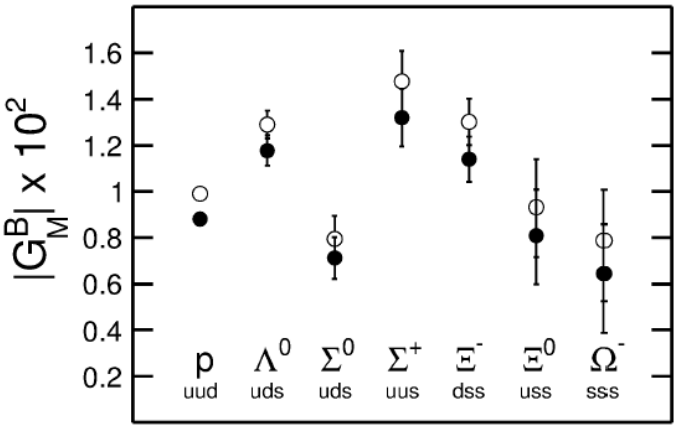

Fig 4.4 Measurement of the transition form-factors performed by the CLEO experiment [69], the open circles represent a situation when $G_E = 0$, closed circles on the other hand are related to $G_M = G_E$.

The results demonstrate a significant difference of obtained form-factor value for different cases. But what is very interesting and significant in further discussion if one takes a closer look at Λ^0 and $\sum^0$ cases. Both share the same quark content but the values of G_M differ dramatically. First question witch can be addressed "What is the reason of those dramatic differences?". The answer to this question leads to the issue of quark correlations inside a hyperon.

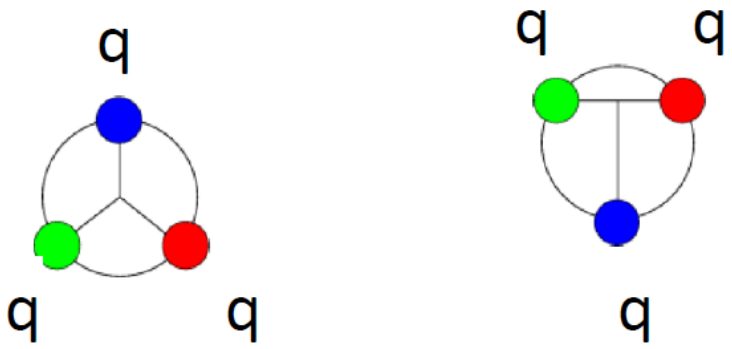

Fig 4.5 Possible quark configuration inside a hyperon, first graph from the left is the triplet configuration the second one features a singlet state, also referred as a di-quark configuration.

The diagrams presented in **Fig 4.5** show the possible quark configurations. It has been emphasized lately by Wilczek [70] that di-quark configurations (see **Fig 4.5** second form the left) are very important in low energy QCD dynamics. Looking at results presented in [71] and the relation presented in formula (23) together with **Fig 4.4** leads to a conclusion that the di-quark configuration is "favored" when comparing G_m for Λ^0 and $\sum^0$.

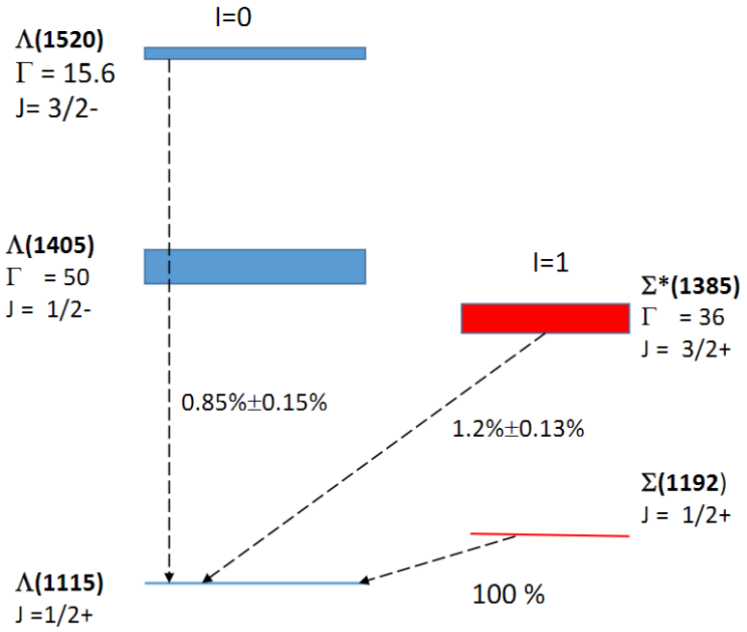

Fig 4.6 Diagram showing decays of hyperons to a real photon. Known widths of the states and their corresponding branching ratios are presented as well.

As discussed in section **1.2**, eTFF in the time like region can be investigated via Dalitz decays. **Fig 4.6** shows a mass diagram of established hyperon states, known branching ratios for the radiative decays and the width of each state. As discussed, the decays to a real photon or a virtual photon are sensitive to the structure of the state. The hyperon states are very narrow, thus in contrast to broad non-strange baryon resonances, are very easy to identify. An example of such a decay can be the Dalitz decay of $\Lambda(1520) \rightarrow \Lambda^0 e^+ e^-$.

In the analysis presented in this thesis, the simulation of the $\Lambda(1520)$ Dalitz decay into a Λ^0 and a pair e^+e^- will be presented. The width of this decay has be parametrized as described in [72] assuming point-like structure of the resonance. But in general it can be written as presented below.

$$\frac{d\Gamma}{dM} = \text{"QED"} \cdot eTFF(Q^2 = M^2) \qquad (24)$$

The QED part stands for a point like object with a given spin and parity, adjusted to the known width of $\Lambda(1520)$ radiative decay. The term eTFF relates to the already discussed electromagnetic transition form-factors which depend on the lepton invariant mass and grant access to the information related to hyperon structure.

The calculations based on the VDM [6] show spectacular effects. The model predictions for kaon induced reactions presented in [93], show a significant enchantment of the hyperon production cross section. The peaks visible in **Fig 4.7** correspond to resonant vector meson states such as ρ, ω and φ dominating the eTFF. Different curves correspond to the Λ, the $\sum^0$ and the $\Lambda(1405)$, the difference between them is connected with the sensitivity of coupling with different hadrons.

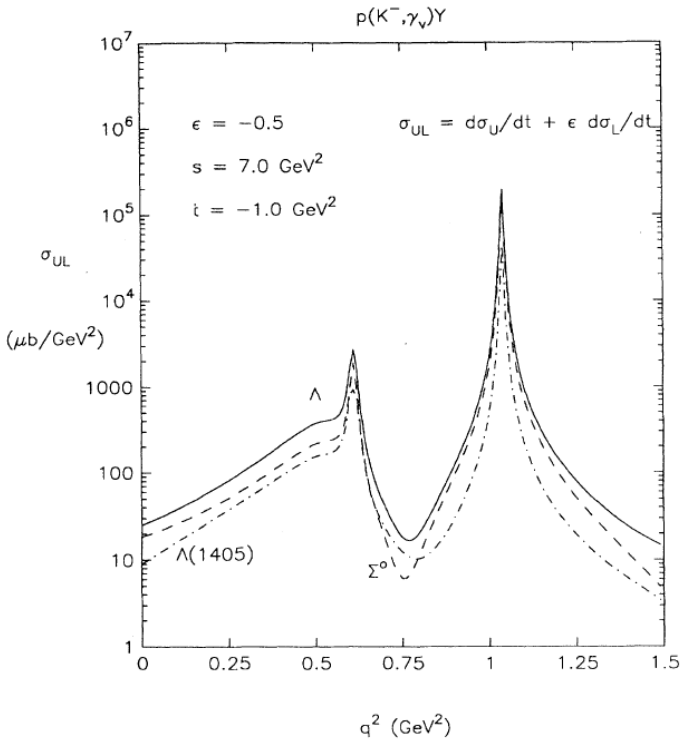

Fig 4.7 Cross section in a function of the q^2 for the radiative capture in $p(K^- \gamma)Y$ (Y – stands for a hyperon)[93].

4.3 Future FAIR facility

Presently, GSI operates in many aspects of a unique accelerator facility for the heavy ion beams. The accelerator complex consists of the universal linear accelerator the UNILAC, the synchrotron SIS18, and the experimental storage ring ESR. In 2001 an additional complex has been proposed by the international community that will turn the GSI into an international, the Facility for Anti-Proton and Ion Research (FAIR). The central part of the FAIR facility will be a synchrotron complex consisting of two separate synchrotron accelerator rings with a maximum magnetic rigidity of 100 Tm and 300 Tm. Both devices have the same circumference and will be installed on top of each other in the same underground tunnel. To achieve high beam intensities, the SIS100 synchrotron will be operated at rate of about 1 Hz with ramp rates of up to 4 Tesla per second for the dipole magnets. The purpose of the ring is to produce intense pulsed uranium ($q=28^+$) beams at a kinetic beam energy of 2.7 GeV/u and intense proton beams at an energy of 29 GeV. For high-intensity proton beams, required for anti-proton production, a new proton linear accelerator injecting into the SIS18 is foreseen as a part of the project. The plan of the FAIR facility is presented below in **Fig 4.8**. The SIS 300 is a future upgrade facility of the SIS 100.

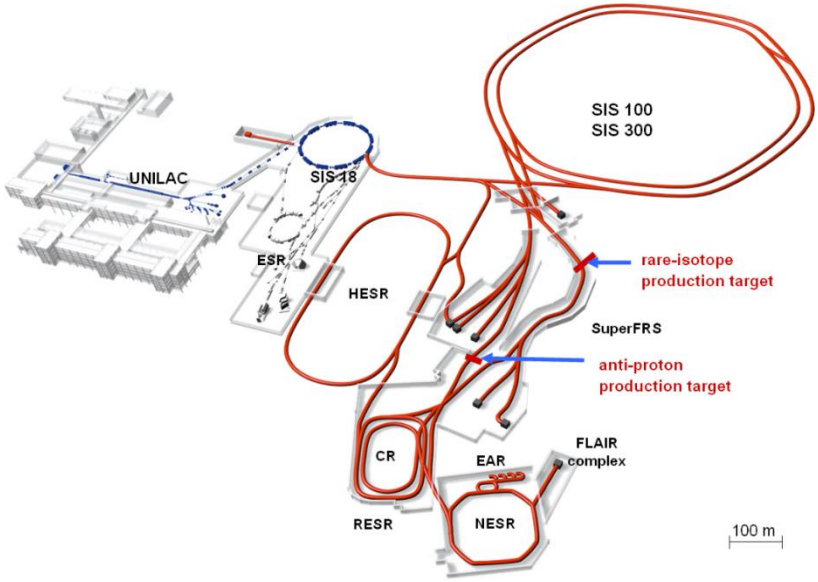

Fig 4.8 A scheme of the future FAIR facility, the existing part is marked by blue and the planned future part is marked as red [56].

In addition to fixed beam experiments stations the facility will have a system of cooler/storage rings: a collector ring (CR) to capture radioactive ion or anti-proton beams from the production targets and apply stochastic cooling. The RESR ring will be used for the accumulation of anti-protons after pre-cooling in the CR and for deceleration of short-lived nuclei. The anti-protons will be accumulated for long time, up to 1 hour.

In-beam physics experiments with ions and anti-protons will be set up in the New Experimental Storage Ring (NESR). It will be equipped with stochastic and electron cooling devices. NESR can be used to decelerate ions and anti-protons and extract them for the FLAIR low energy experiments. Experiments with anti-protons of up to 14 GeV will be installed on the High-Energy Storage Ring (HESR). This ring will feature an internal target and associated detectors. It will be equipped with a high-energy electron cooler and a stochastic cooling system to compensate beam degradation coming from target interaction and beam scattering.

4.4 The PANDA spectrometer

$\bar{P}$ANDA is one of the major experiments that will be installed at the international FAIR facility in the GSI laboratory (Darmstadt, Germany). It will use the high-intensity phase-space cooled antiproton beams provided by the High Energy Storage Ring (HESR) (see **Fig 4.10**). The PANDA experiment will use the antiproton beam from the HESR colliding with an internal proton target to carry out a rich and diversified hadron physics program, which includes the charmonium and open charm and strange baryon spectroscopy, the search for exotic hadrons and the study of in-medium modifications of hadron masses [58]. PANDA will be a fixed target experiment consisting of a Target Spectrometer (TS), surrounding the interaction point, and a Forward Spectrometer (FS), covering the acceptance of the spectrometer at low angles. A solenoid and a dipole will provide the magnetic field inside the TS and FS, respectively. The combination of the two spectrometers allows for a full angular coverage and high acceptance for a wide range of

energies. The detector has a modular structure and can be easily adopted for the needs of different measurements and physics goals:

• QCD bound states (charmonium, strange baryons, exotic states)

• electromagnetic processes

• electroweak physics

• hyper nuclear physics

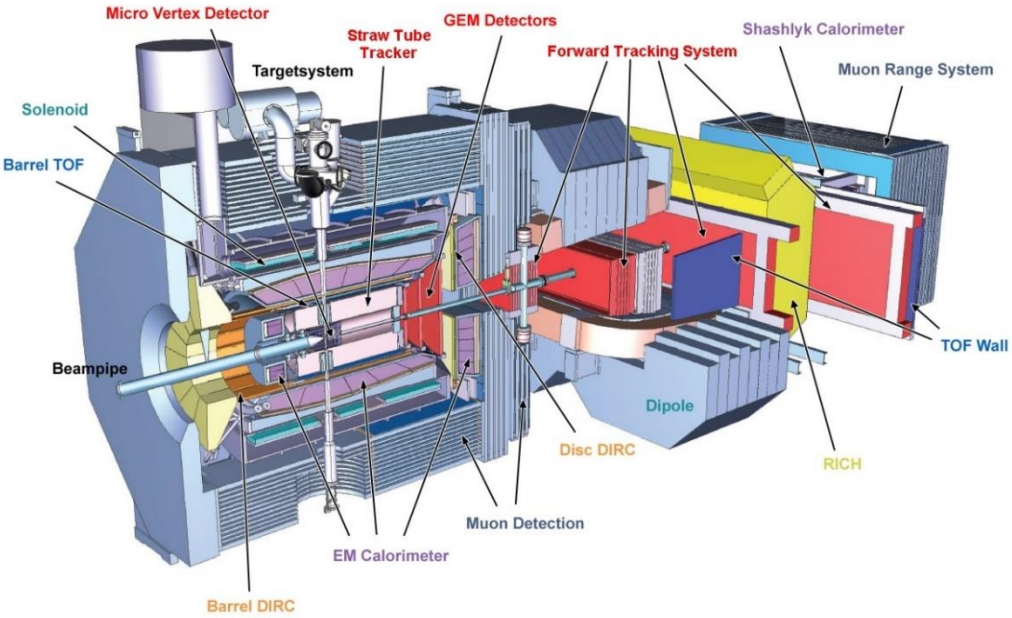

Fig 4.9 Plan of the future spectrometer PANDA. The main components are marked[56].

As mentioned before the system will be installed on a HESR accumulator ring. The technical details and plan of the storage ring are presented below.

Experimental Requirements	
Ion species	Antiprotons
$\bar{p}$ production rate	$2 \cdot 10^7$/s ($1.2 \cdot 10^{10}$ per 10 min)
Momentum / Kinetic energy range	1.5 to 15 GeV/c / 0.83 to 14.1 GeV/c
Number of particles	10^{10} to 10^{11}
Betatron amplitude at IP	1 m to 15 m
Betatron amplitude E-Cooler	25 m to 200 m
Operation Modes	
High resolution (HR)	Peak Luminosity of $2{\cdot}10^{31}\mathrm{cm}^{-2}\mathrm{s}^{-1}$ for 10^{10} $\bar{p}$ assuming $\rho_{target} = 4 \cdot 10^{15}$ atoms/cm^2 RMS momentum spread $\sigma_p/p \leq 4 \cdot 10^{-5}$, 1.5 to 8.9 GeV/c
High luminosity (HL)	Peak Luminosity up to $2{\cdot}10^{32}\mathrm{cm}^{-2}\mathrm{s}^{-1}$ for 10^{11} $\bar{p}$ assuming $\rho_{target} = 4 \cdot 10^{15}$ atoms/cm^2 RMS momentum spread $\sigma_p/p \sim 10^{-4}$, 1.5 to 15 GeV/c

Table 1.4 Technical details of the HESR, the ring will operate in two modes to fulfil the demands of the planned physics program [58].

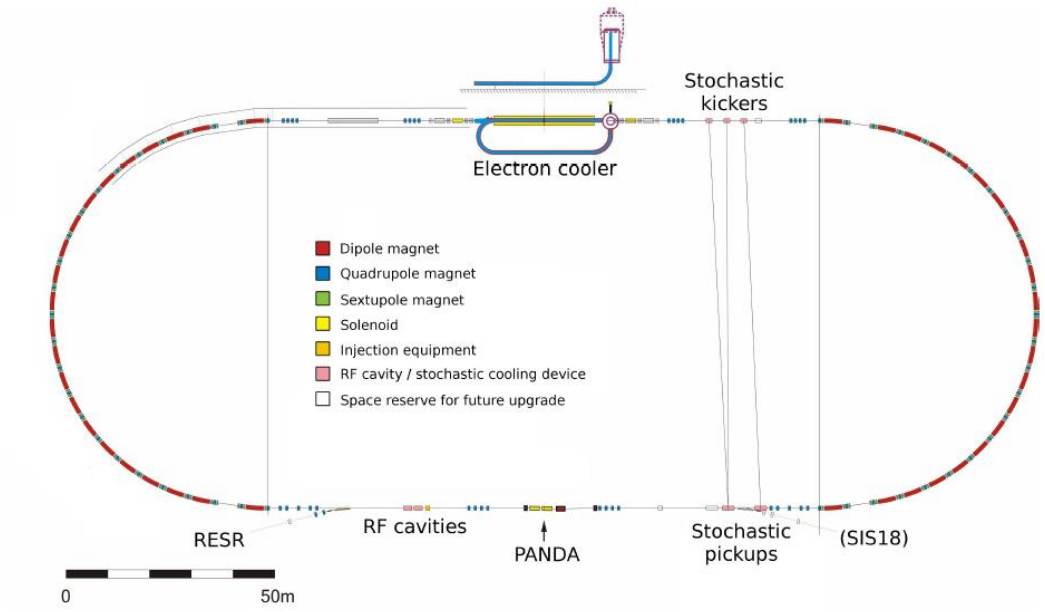

Fig 4.10 Plan of the HESR storage ring, the system will possess the possibility of electron and stochastic cooling. The place of the PANDA detector installation is marked with a black arrow [56].

As visible in **Fig 4.9** the PANDA spectrometer is a complex system consisting of many sub detectors. The Central and Forward spectrometers are equipped with tracking systems providing excellent momentum resolution at a level of 1%. Identification of charged particles with sufficient accuracy is a major requirement for studying many aspects of the physics program inside the PANDA experiment. The PANDA spectrometer will be equipped with various dedicated particle identification (PID) systems granting the ability of classifying particle species over the whole kinematic range in addition to dE/dx obtained from track reconstruction and information from the electromagnetic calorimeters.

4.4.1 The STT (Straw Tube Tracker)

The PANDA central straw tube tracker has a cylindrical shape with an inner radius of 150 mm and an outer of 418 mm. The STT will be the main detector for track reconstruction for charged particles in the PANDA target spectrometer. It consists of 4636 single straw tubes, arranged in a large cylindrical volume around the beam-target interaction point. The arrangement of the straws in the detector is presented in **Fig 4.11**.

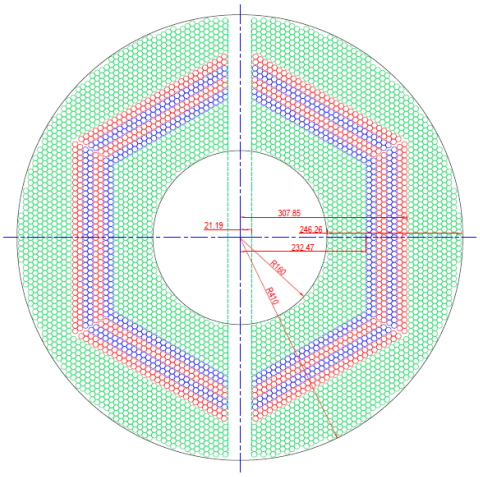

Fig 4.11 Cross section of the straw tubes in the STT. Green straws are parallel to the beam axis. The blue and red straw layers are skewed relative to the axially aligned straws in the same sector [73].

A complete description of this detector can be found in [73]. The lay out of the detector and the prototype frame are presented in **Fig 4.12**.

(a) (b)

Fig 4.12 a) CAD drawing of the detector b) prototype of the support frame [73].

As mentioned before the detector will consist of straws (photo in **Fig 4.11** and **Fig 4.12**), which are gas-filed cylindrical tubes (see **Fig 4.13**) ($ArCO_2$ 90%/10% at 1 bar overpressure) with a conductive inner layer acting as a cathode and an a wire in the middle (anode). Positive voltage at a level of kV applied to the anode wire will provide an electric field which will separate electrons and positive ions produced by a charged particle along its passage trajectory in the gas volume. The strong electric field near the anode (due to its small diameter of an level of few μm) provides the possibility of further ionization of the gas thus amplifying the signal by a factor of 10^4.

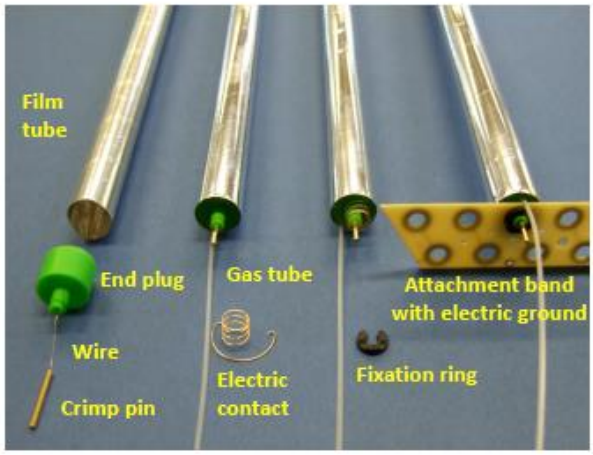

Fig 4.13 Photo of the straw tube components**.**

By the measurement of the drift time one obtains the track distance from the tube wire. The tracks are reconstructed by a fit to the data points in a series of straw tubes. Additional skewed straw layers provide a full stereo view of the particle trajectory.

In addition to the track reconstruction capability the STT provides the possibility of charge particle identification by measuring the specific energy loss dE/dx. Each tube works in the "proportional counter" mode, this corresponds to the fact that the obtained signal form the detector is proportional to the energy loss of the particle (dE), the path will be obtained from track reconstruction (dx). By combining the obtained dE/dx information with the particle momentum thanks to the bending of the trajectory in the magnetic field on can perform a particle identification as presented in **Fig 4.14**.

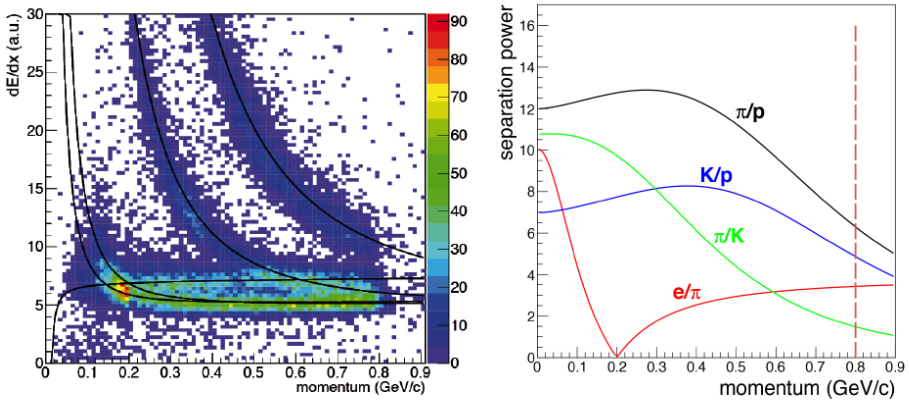

(a) (b)

Fig 4.14 a) dE/dx distribution in a function of momentum for selected particles b) separation power in a function of momentum between selected particles [73].

4.4.2 The Barrel DIRC (Detection of Internally Reflected Cherenkov Light)

Particle identification (PID) for hadrons and leptons at a large range of an polar angle θ and momenta is an important point for the physics objectives at the PANDA experiment. Charged particles in a medium with a specific index of refraction "n" traversing with a velocity $\beta_c > 1/n$ emit radiation at an angle $\theta_c = \arccos(1/\beta n)$. The mass of the detected particles can be obtained by calculating the velocity from θ_c and the momentum reconstructed from the tracking detectors. The principle of operation of the DIRC detector has been presented in **Fig 4.15**.

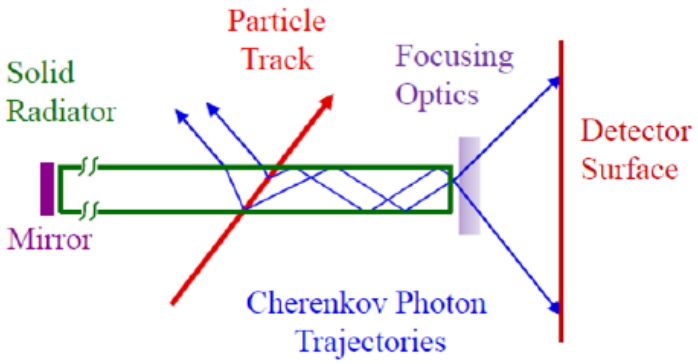

Fig 4.15 The DIRC operation scheme [74,75].

Within the central part of the detector, for the polar angles between 22°-140°, a particle identification can be performed by the detection of internally reflected Cherenkov (DIRC) light. The system will consist of 1.7 cm thick quartz elements surrounding the beam line at a distance of 48 cm. The DIRC also plays a role for the calculation of the distinction between gammas and relativistic charged particles entering the EM-calorimeter behind. The plot presented in **Fig 4.16** presents an overview of the detector and its main components.

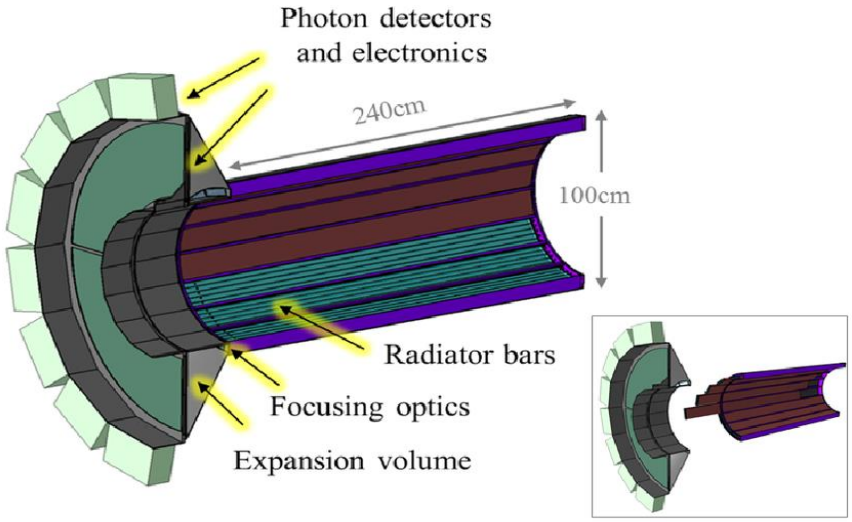

Fig 4.16 Schematic view of the barrel DIRC detector [74,75].

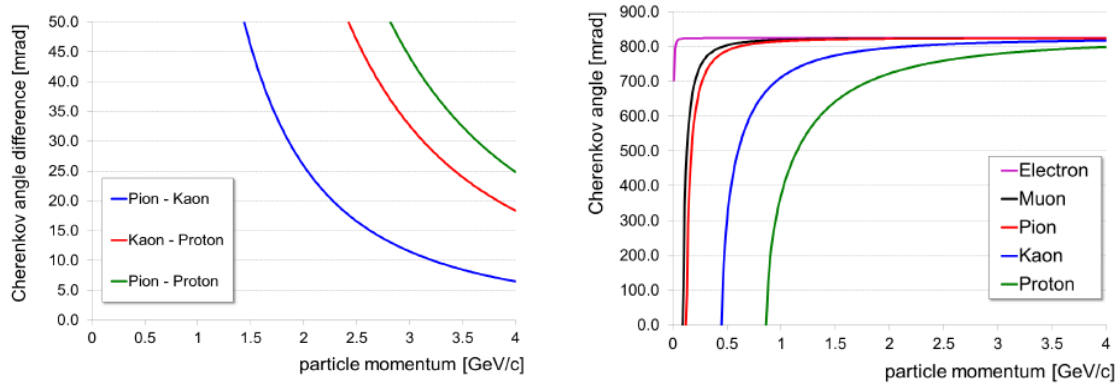

Fig 4.17 Two plots show the simulation results done in order to test the detector. Left plot presents the Cherenkov angle difference between selected particle species, on the right θ_c in a function of the momentum is presented [75].

The majority of the hadrons produced in anti-proton proton annihilations are pions. The hadronic charged particle identification in the central part of the detector has to be able to separate pions from kaons for momenta up to 3.5 GeV/c. As one can see in **Fig 4.17** (left) this point is fulfilled and even more the DRIC will also contribute to an electron identification (**Fig 4.17** right) for particle momentum up to 1 GeV/c. For higher momentum particles the separation power drops significantly, this requires to introduce yet another detector in the setup. This subject will be discussed in the next sections.

4.4.3 The Disc DIRC

The disc has a hexa-decagonal shape with a rectangular hole in the middle for the beam pipe. Each side of the detector is equipped with a LiF bar guiding the photons to silicon light guides. Total 96 light guides are read out by 4608 single photon readout channels (PMT`s or photo multipliers). The traversing particle creates the Cherenkov photons which hit the LiF part of the disc. Leaving the LiF to the fused silicon light guides, the photons are now focused to a focal readout plane. By obtaining the readout position, the Cherenkov angle can be reconstructed. The principle of operation and schematic overview of the detector is presented in **Fig 4.18**.

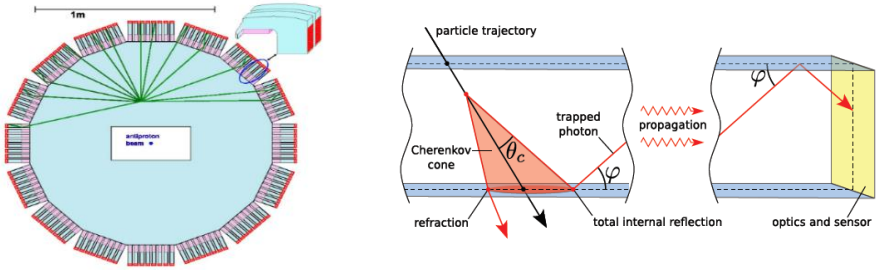

Fig 4.18 Schematic view of the Disc DIRC detector on the left, the principle of operation on the right [76, 77].

The main role of the detector is to fill the acceptance gap of the Barrel DRIC detector for particles emitted at low polar angle and with high momenta. As visible in **Fig 4.19** the π-K separation above the momentum of 3.5 GeV/c is moderate.

Instead of preforming the reconstruction of the Cherenkov angle θ_c as presented in the previous section, a pattern matching approach is used [78]. Each hit in the detector is compared to the corresponding hit in a hypothesis, resulting in a likelihood value for the assumed particle type. The procedure gives a reasonable separation power for higher momenta particles. The results for pion/kaon are presented in **Fig 4.19** as a function of the momentum and the emission angle.

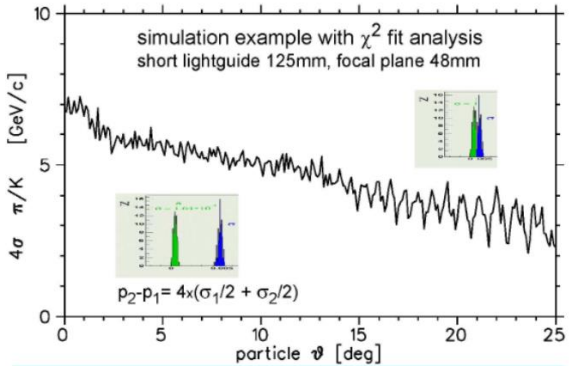

Fig 4.19 Separation power vs the angle of incident [78].

4.4.4 Micro vertex detector

The Micro-Vertex Detector (MVD) will be the inner part of the central tracking. The system will deliver 3D hit information near the interaction point. The capability of identification of open charm and strangeness states is one of the major tasks for the experiment, adding the possibility to reconstruct secondary decays of short-lived particles in displaced vertices.

Additionally, the energy loss measurement of protons, kaons and pions in the silicon detectors may be used to contribute to the global particle identification capability of the whole spectrometer. Two types of detectors will be implemented in the MVD set up, hybrid pixels and double-sided micro-strips. The detailed information related to the detector can be found in [79].

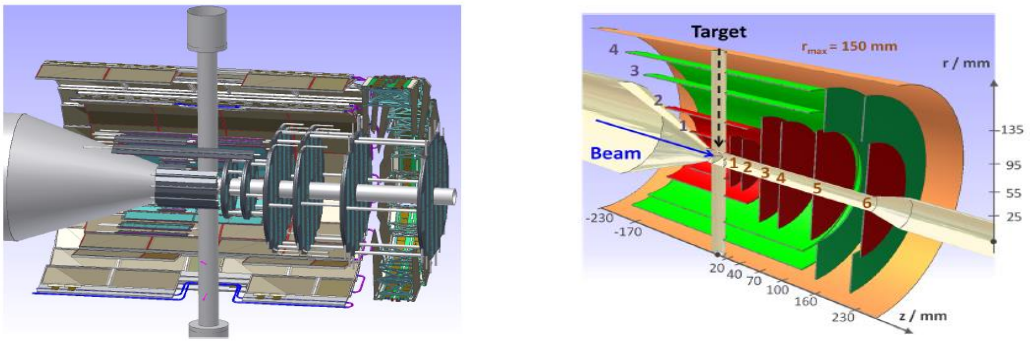

Fig 4.20 Left: schematic view of the MVD detector. Right: a detailed plane the, red areas represent the silicon hybrid pixel sensors the green area on the other hand represent double-sided silicon micro-strip detectors [79].

The MVD is divided into two parts, a barrel and a forward part. The radius of the barrel part is 15 cm and it goes along the beam axis with z = 23 cm with respect to the interaction point. The layout of the detector is presented in **Fig 4.20**. The detector layout results in an acceptance coverage with a minimum of four track points in a polar angle interval from 9° to 145°. The barrel part covers polar angles between 40° and 150°.

To define a benchmark of the detector a simulation has been made. The interaction of different particles has been simulated within PandaROOT (simulation and analysis package) [81] using Geant4. In order to fully reproduce the uncertainty of the detector only reconstructed tracks are analyzed. The results are presented in **Fig 4.21**.

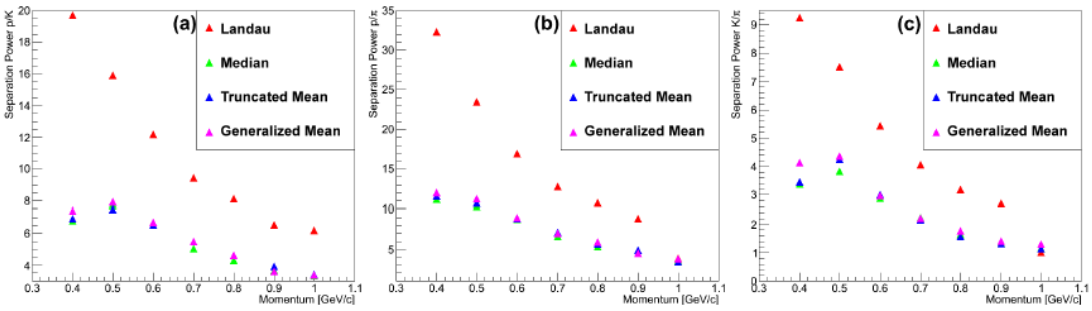

Fig 4.21 Separation power vs momentum characteristic correlations obtained by simulating the MVD detector implemented inside the PandaROOT framework [81]. The separation power was calculated between different particle species a) p/K b) p/π c) K/π. [79]

The presented results for the separation power achieved from the energy-loss measurement were obtained by different methods discussed in detail in [79], but judging only on the "Landau" method the MVD provides an excellent contribution to the detector particle identification capability in the region of low momenta.

4.4.5 The Electromagnetic Calorimeter (EMC)

In the region of the target spectrometer high precision electromagnetic calorimetry is necessary over a wide energy range. Lead-tungstate composite has been chosen for the calorimeters in the target spectrometer because of its high density. Identification and reconstruction of photon and lepton-pair is an important part of the PANDA physics program. Low threshold energy, good energy and spatial resolution are crucial to achieve high yield and background rejection. Due to the high particle flux, fast response and radiation hardness are a key factor in the design. The largest part of the detector will be the barrel calorimeter with 11360 crystals of 200 mm length. In the backward direction 592 crystals will be installed. The 3600 crystals in the forward direction will be inflicted with a much higher rate of particle across the acceptance of the calorimeter. Readout consisting of vacuum photo triodes will be installed in order to operate at the higher particles rates and correspondingly higher radiation load. The schematics of the detection system is presented in **Fig 4.22** and the requirements for the detector are listed in **Table 1.5.**

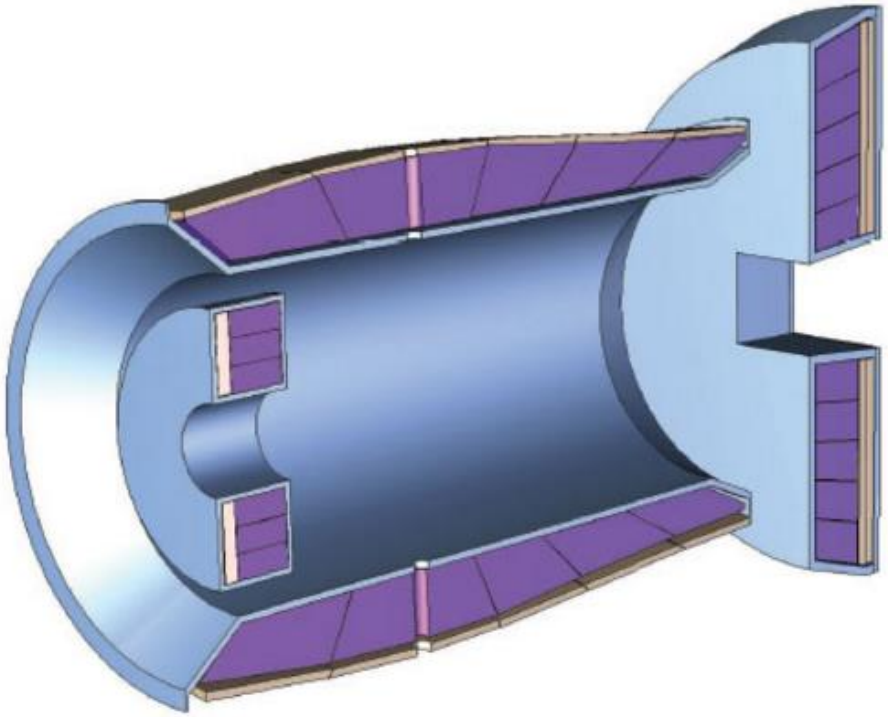

Fig 4.22 3D view of the EMC barrel and the forward and backward endcaps of the detection system, the drawing is taken from [95].

	Required performance value		
Common properties			
energy resolution σ_E/E	$\leq 1\,\% \oplus \frac{\leq 2\,\%}{\sqrt{E/\mathrm{GeV}}}$		
energy threshold (photons) E_{thres}	10 MeV (20 MeV tolerable)		
energy threshold (single crystal) E_{xtl}	3 MeV		
rms noise (energy equiv.) $\sigma_{E,noise}$	1 MeV		
angular coverage $\%\,4\pi$	99 %		
mean-time-between-failures t_{mtbf}	2000 y		
(for individual channel)			
Subdetector specific properties	backward ($\geq 140°$)	barrel ($\geq 22°$)	forward ($\geq 5°$)
energy range from E_{thres} to	0.7 GeV	7.3 GeV	14.6 GeV
angular equivalent of crystal size θ	4°		1°
spatial resolution σ_θ	0.5°	0.3°	0.1°
maximum signal load f_γ ($E_\gamma > E_{xtl}$)	60 kHz		500 kHz
($p\bar{p}$-events) maximum signal load f_γ ($E_\gamma > E_{xtl}$)	100 kHz		500 kHz
(all events) shaping time t_s	400 ns		100 ns
radiation hardness	0.15 Gy	7 Gy	125 Gy
(maximum annual dose $p\bar{p}$-events)			
radiation hardness	10 Gy		125 Gy
(maximum annual dose from all events)			

Table 1.5 List of requirements for the EMC. The table is taken from [95].

4.4.6 Muon System

The system will be made of 13 sensitive layers, each layer will be 3 cm thick (the layer closest to the center of the detector will be doubled), 3 cm thick iron absorber layers will be responsible for the absorption of pions. For the forward End Cap more material is needed because of the foreseen higher momenta particles, six detection layers will be placed around five iron layers of 6 cm each within the return yoke, in addition a removable Muon Filter with additional four layers of 6 cm thick iron and corresponding detection layers will be placed in the space between the solenoid and the dipole magnets. Acting as sensor system in between the absorber layers, the Mini Drift Tubes (MDT) will be placed. The MDTs are drift tubes with additional capacitive coupled strips. The laminated yoke of the solenoid magnet and the additional Muon Filter will be equipped with 2751 MDTs and 424 MDTs. The setup is presented in detail in **Fig 4.**23**.**

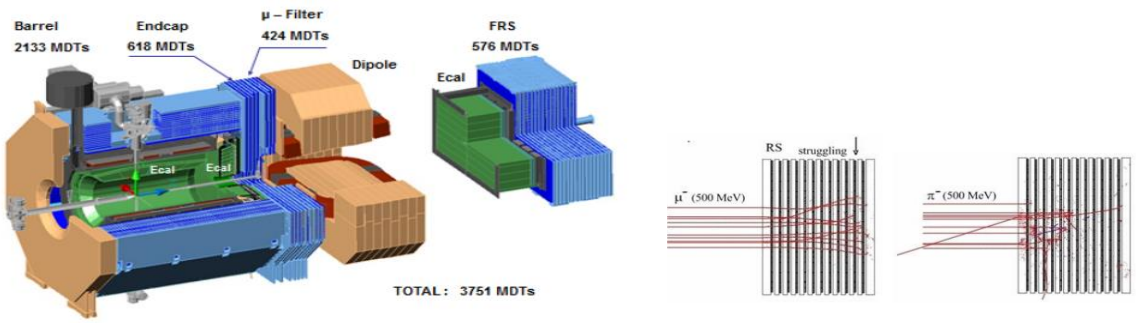

Fig 4.23 Schematics showing a position of the MDTs in the central and forward part of the PANDA spectrometer (left panel), on the right panel 500 MeV (kinetic energy) muons and pions traversing the absorber layers. The picture is taken from [96].

The system will play an important role in the μ/π separation. The pions and the muons behave differently when traversing the absorber material. The muons traversing through the iron absorber, undergo energy loss due to ionization till they are stopped. In the case of pions passing through an absorber, they also experience the ionization energy loss and in addition, the effect of showering because of their strong interaction in the absorber material. This effect is presented in **Fig 4.23** (see right panel). This effect has been confirmed by simulations, the results are presented below.

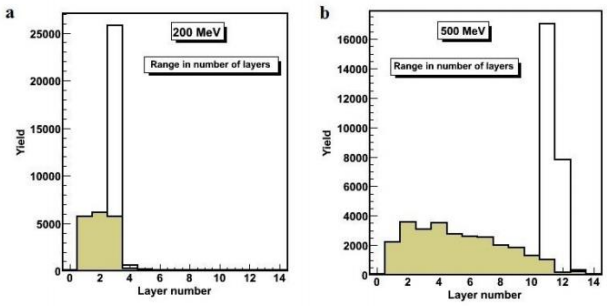

Fig 4.24 Yield as a function of the traversed layers for two different beam kinetic energies 200 and 500 MeV. Events counting muons are presented by the narrow peak (black line), pions are represented by the brown area. Picture taken from [96].

Fig 4.24 shows the distribution of layers traversed by the muons (narrow peak) and the pions represented by a broad distribution (colored area). The muons due to their constant energy loss at 2 MeV produce a narrow peak for booth energies (mean value of about 3 layers for a beam energy of 200 MeV and 11 for energy of 500 MeV) as for the pions the distribution is broad, because of the additional interaction with the material. This technique has a slight disadvantage as one can see in **Fig 4.24**: each narrow muon peak has an admixture of "fake muons" (pions) which depends on momentum.

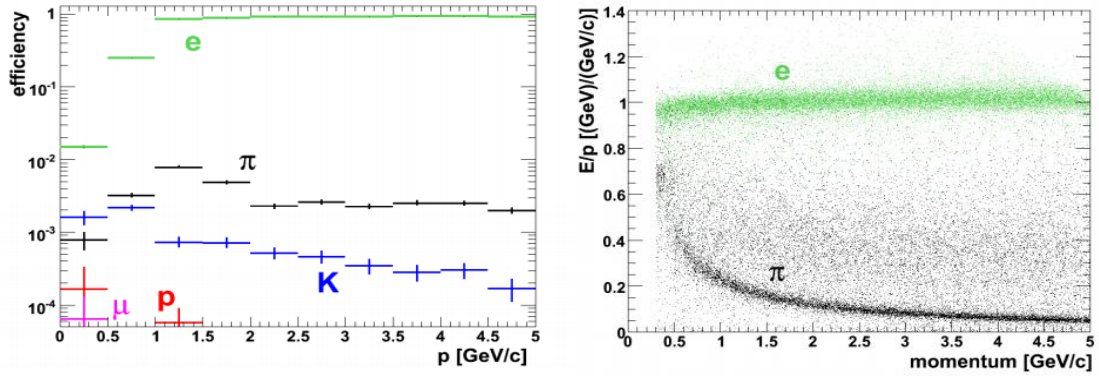

Fig 4.25 Left: Electron identification efficiency (green line), overlapped with contamination coming from K, π, p and μ. Right: E/p (energy to momentum ratio) in a function of momentum, plotted for electrons (green) and pions (black). The plot is taken form [95].

The EMC will play an important role in the identification of electrons/positrons. Electrons, muons and hadrons, can be identified by their characteristic electromagnetic shower. The overall difference will be the deposited energy in the EMC material. Muons and hadrons deposit a fraction of their energy due to the ionization while electrons lose their energy entirely via an electromagnetic shower. The difference in energy loss is presented in **Fig 4.25** (right plot) showing a ratio of the measured deposited energy and momentum in a function of the reconstructed track momentum. As one can see for the electrons this ratio is mostly constant and close to unity and differs in comparison to the one corresponding to the pions. This information and the known difference in the shape of the shower (for details see [95] page 145). Altogether the information provides a possibility to identify the electrons with sufficient efficiency as presented in **Fig 4.25** left. The purity of the electron sample is quite high as well, 100 time higher than the pion contaminated signal.

4.4.7 The Forward Tracker and the Forward Spectrometer

The role of the Forward Tracking (FT) is the momentum analysis of charged particles deflected in the field of the $\bar{P}$ANDA dipole magnet. The FT will detect particles emitted within an angular range of (-10°, 10°) and (-5°, 5°) in the horizontal and vertical directions, respectively. The system consists of three pairs of tracking stations (see **Fig 4.26**): one pair (FT1, FT2) is placed in front, the second (FT5, FT6) behind the dipole magnet and the third pair (FT3, FT4) is placed inside the magnet gap to track low momentum particles.

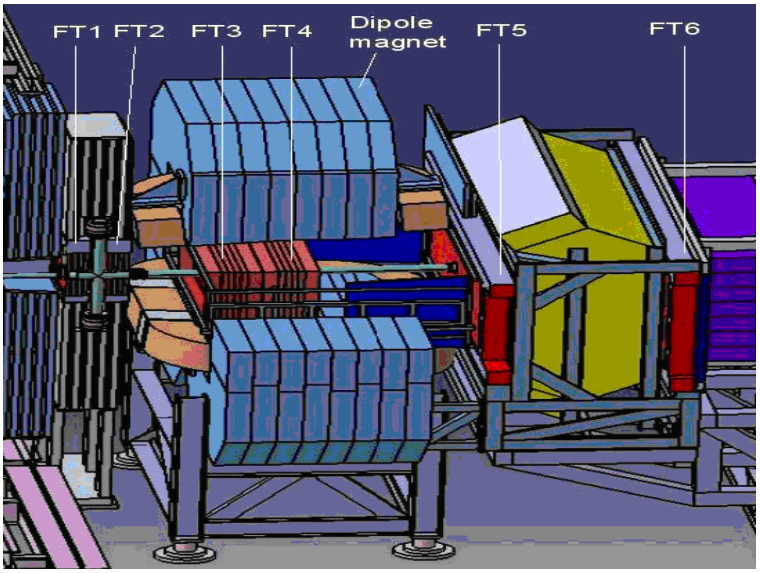

Fig 4.26 Layout of the three pairs of tracking stations. Picture comes from [80].

Each FT station (**Fig 4.26**) is composed of four sets of planar double layers of straw tubes oriented at vertical and stereo angles (0°, +5°, -5°, 0°). Each tube will have a 10 mm inner diameter, a 30 μm thick aluminized Mylar foil as cathode and a 20 μm diameter gold-plated tungsten-rhenium wire as anode. The tubes will be filled with a gas mixture of $ArCO_2$ (90/10) and will be operated at a 2 bar absolute pressure. The tracking stations will be exposed to high local particle fluxes, reaching 10^4 $cm^{-2}s^{-1}$ close to the beam pipe at the maximum interaction rate of $2 \cdot 10^7$ s^{-1} expected in the high luminosity mode of $\bar{P}$ANDA.

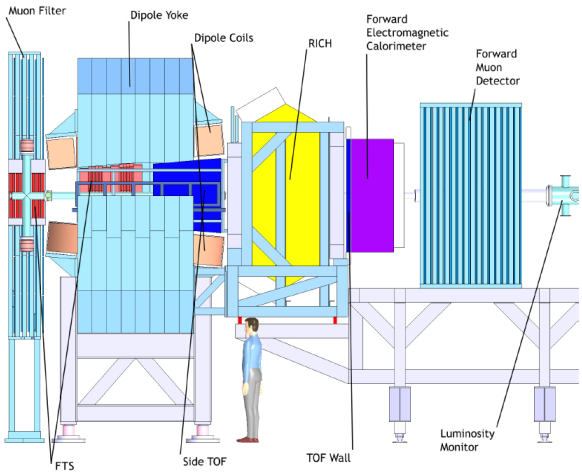

Fig 4.27 Side view of the forward spectrometer. The main components are: TOF Wall, Luminosity Monitor, FS, RICH and Forward Electromagnetic Calorimeter with Muon Detector behind it**.** [80]

The forward spectrometer will also have additional detectors as presented in **Fig 4.27**, brief discussion is presented below.

Dipole Magnet
2 Tm magnet with an entrance of more than 2 m and located 4 m downstream with respect to the target, of a size of 1.6 m along the beam axis.

Ring Imaging Cherenkov Detector (RICH)
The RICH detector for PANDA will consist of two radiator materials which will give the possibility to separate different particles (p/K/π) in a broad momentum range from 2 to 15 GeV/c.

Time-Of-Flight Wall
It will grant the possibility to perform π/K and K/p separation at a 3σ level up to 4.7 GeV/c, with a resolution of 50 ps. The TOF will consist of plastic scintillators, read-out by fast PMTs on both ends. It will be placed in different positions: 7 m downstream and inside the dipole magnet.

Calorimeter
A distance of 7.5 m from the target a Shashlik-type calorimeter will be placed. It will feature 351 Shashlik modules arrange in 13 rows and 27 columns.

Muon System
Absorber layers and rectangular aluminum drift tubes will be used to detect the very forward part of the muons. This system will also give the possibly of preforming the energy measurement of neutrons and antineutrons (for details see section **4.4.6**).

Luminosity Monitor
The elastic scattering events of antiprotons in a range from 3 mrad to 8 mrad with respect to the beam axis will be detected by 4 track planes made of silicon detectors and positioned from 10 m up to 12 m from the target.

4.5 Benchmark studies

The goal of this study is to emphasize the role of the Forward Spectrometer (FS) in the PANDA experiments.

4.5.1 Benchmark channels

Systematic studies of the selected physics channels were performed by means of the PandaROOT software, described in details in [81]. The impact of the acceptance of the Forward Spectrometer for the reconstruction of selected production and decay channels, relevant for the $\bar{P}$ANDA physics program, has been studied.

$$\bar{p}p \rightarrow \Psi(4040) \rightarrow D^{*+}D^{*-} \rightarrow D_0\pi^+\bar{D}_0\pi^- \rightarrow K^+K^-\pi^+\pi^-\pi^+\pi^-$$

$$\bar{p}p \rightarrow \Lambda\bar{\Lambda} \rightarrow p\pi^-\bar{p}\pi^+$$

Each of the channels addresses different physics topics discussed in this thesis, the Ψ(4040) decay is related to the charmonium topic, the $\Lambda\bar{\Lambda}$ refers to the hyperon study. Both studies will justify the significance of the Forward Spectrometer.

4.5.2 Simulation and reconstruction

The $\bar{p} - p \rightarrow \psi(4040) \rightarrow D^{*+}\ D^{*-}$ reaction with the anti-proton beam momentum of 7.71 GeV/c has been simulated and analyzed. The Monte-Carlo simulation in the full solid angle are presented in **Fig 4.28**, showing the polar angle vs momentum distribution for the kaons coming from the $D^0 \rightarrow K\ \pi$ decay (left) and from pions coming from the $D^* \rightarrow D^0\ \pi$ followed by the D^0 decay (right). A "hot spot" in the distribution of pions located at small emission angles and momenta corresponds to events from the D* decays, due to a small excess energy and a small mass differences between the D* - D^0 mesons. **Fig 4.29** presents the same distributions but after the reconstruction in the PANDA spectrometer. In addition, in **Fig 4.30** the analysis results but without the Forward Spectrometer are presented. The respective reconstruction rates for both scenarios are presented in **Table 1.6**.

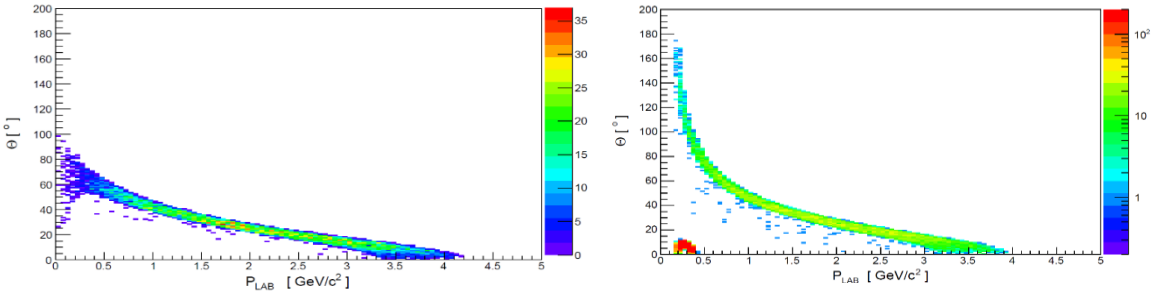

Fig 4.28 Distribution of the polar emission angle vs the momentum for the pions (right) and the kaons (left), coming from the Monte-Carlo simulation in the full solid angle.

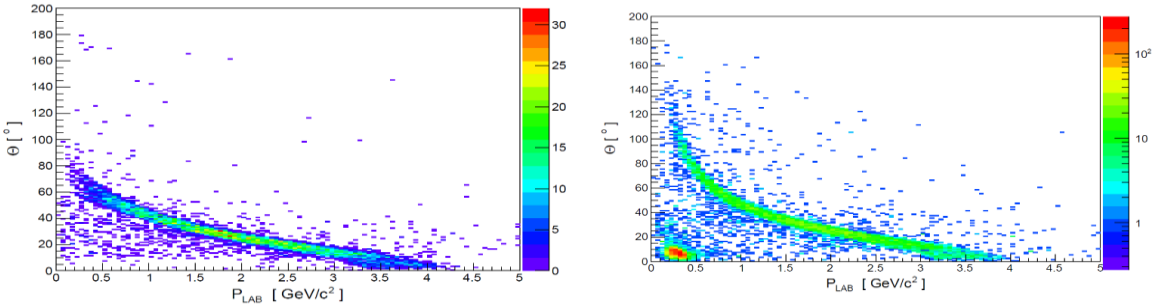

Fig 4.29 Distribution of the polar emission angle vs the momentum for pions (right) and kaons (left), reconstructed in the PANDA spectrometer.

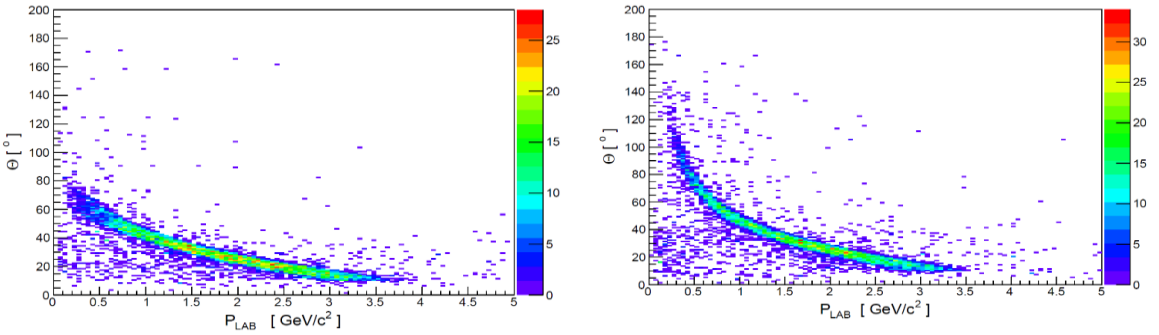

Fig 4.30 Distribution of the polar emission angle vs the momentum for pions (right) and kaons (left), reconstructed in the PANDA spectrometer but with the FS excluded.

Reconstruction efficiency (Forward Spectrometer present)	
Kaons	Pions
78%	67%
Reconstruction efficiency (Forward Spectrometer not present)	
75%	40%

Table 1.6 Reconstruction efficiency of pions and kaons.

A particular feature of the $D^* \rightarrow D^0 \pi$ decay is that due to the low energy excess above the decay threshold, almost all pions are emitted below 10^o therefore reach the Forward Spectrometer (see **Fig 4.29** and **Fig 4.30**). This is also true for a fraction of kaons and pions coming from $D^0 \rightarrow K \pi$ decay. The Forward Spectrometer allows for reconstruction of the D* meson with a good efficiency (see **Table 1.7**).

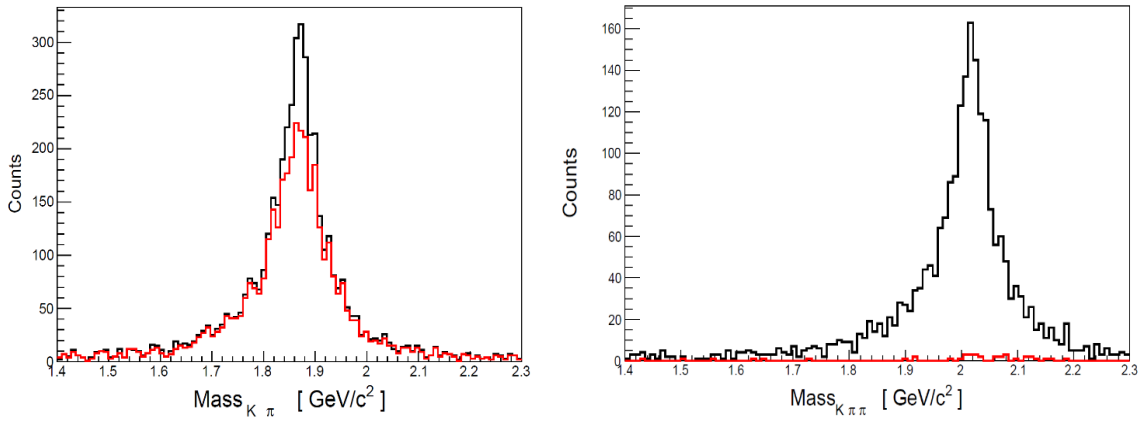

Fig 4.31 Reconstructed invariant mass of the D^0 ($\rightarrow K\pi$) (left) and D* ($\rightarrow K\pi\pi$) meson (right). Black and red curves represent the result of the event reconstruction in the PANDA spectrometer with and without the Forward Spectrometer, respectively.

Reconstruction efficiency (Forward Spectrometer present)	
D^0	D*
51%	25%
Reconstruction efficiency (Forward Spectrometer not present)	
44%	N/A

Table 1.7 Reconstruction efficiency of the D-mesons.

Fig 4.31 (left) presents the D^0 invariant mass in two cases: with (back curve) and without the Forward Spectrometer (red curve). However, the reconstruction of the D* is not possible without the Forward Spectrometer due to lack of pion acceptance from the $D^* \rightarrow D^0 \pi$ decay in the forward region of the PANDA spectrometer (see **Fig 4.30**, **Fig 4.31** right and **Table 1.7**). Also some kaons from the D^0 decay are lost (**Fig 4.30** left). The importance of the Forward Spectrometer has been demonstrated here for a selected reaction but the conclusion is also valid for other decay channels with D-mesons decays.

Finally, **Fig 4.32** shows the reconstructed invariant mass of the ψ(4040) meson from the final state of $K^+ K^- \pi^+ \pi^- \pi^+ \pi^-$ with the efficiency of 8.5%. The red solid curve shows a fit with a Gaussian function: the mean value at 4.039 and $1\sigma = 0.063$. The Ψ(4040) reconstruction is not possible without the Forward Spectrometer due to missing acceptance for the D^{*+} and D^{*-}. This justifies the importance of the Forward Tracking System.

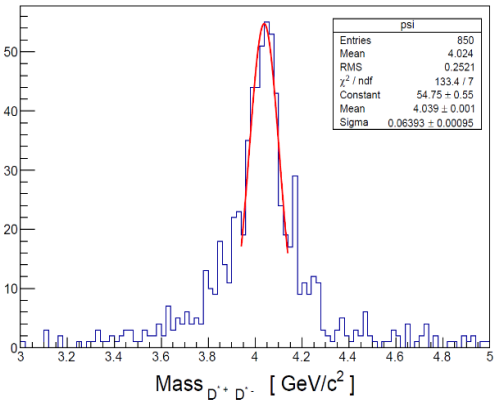

Fig 4.32 D^{*+} and D^{*-} final state: Reconstructed invariant mass of the ψ (4040) meson (Forward Spectrometer present). The red curve presents a Gaussian function fitted to the distribution.

In the second part of the study, a simulation of the $\bar{p}p \rightarrow \Lambda^0\bar{\Lambda}^0 \rightarrow \bar{p}p\pi^+\pi^-$ has been performed with the anti-proton beam momentum of 4 GeV/c. The $\Lambda\bar{\Lambda}$ angular distributions have been modelled according the parametrization measured by the LEAR experiment [82].

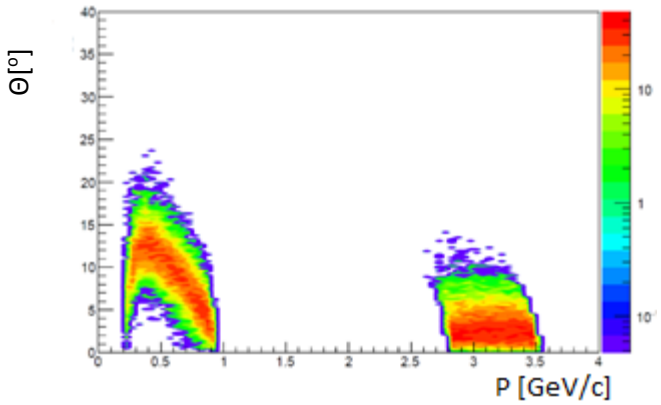

Fig 4.33 $\bar{p}p \rightarrow \Lambda^0\bar{\Lambda}^0 \rightarrow \bar{p}p\pi^+\pi^-$ final state. The polar emission angles vs the momentum of π^+ (up to 1 GeV/c) and high momentum anti-protons from the anti-lambda decay $\bar{\Lambda}^0 \rightarrow \bar{p}\pi^+$.

Fig 4.33 presents the polar angle in a function of the momentum for the pions (0.2 GeV/c to 1 GeV/c) and the anti-protons (2.6 GeV/c to 3.6 GeV/c). The majority of π^+ and the anti-protons coming from the forward going $\bar{\Lambda}$ decay are emitted below 10^o in the polar angle, thus going directly in the forward part of the detector. The respective reconstructed distributions are presented in **Fig 4.34** and the reconstruction rates are presented in **Table 1.8**. The forward tracking system is capable of reconstructing a forward going particles with a good efficiency.

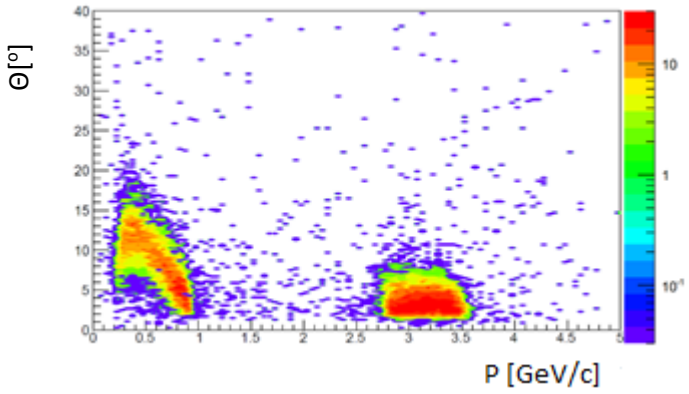

Fig 4.34 $\bar{p}p \to \Lambda^0\bar{\Lambda}^0 \to \bar{p}p\pi^+\pi^-$ final state. Distributions showing the reconstructed π^+ and high momentum forward boosted anti-protons from the anti-lambda decay $\bar{\Lambda}^0 \to \bar{p}\pi^+$.

Reconstruction efficiency (Forward Spectrometer present)	
π^+	$\bar{p}$
53%	65%

Table 1.8 Reconstruction efficiency of pions and anti-protons.

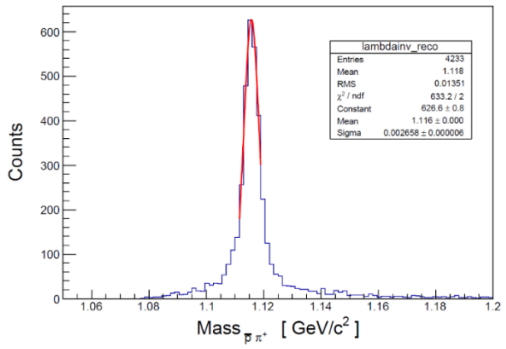

Fig 4.35 Invariant mass spectrum of the reconstructed $\bar{\Lambda}^0 \to \bar{p}\pi^+$ state, red curve represents a Gaussian function fitted to the distribution.

Finally, the invariant mass distributions of the reconstructed anti-lambda state is shown in **Fig 4.35**. The obtained mass resolution ($\sigma/m_{\bar{p}\pi^+}$) amounts to 0.2%.

The presented results of the Monte-Carlo simulations show that the Forward Spectrometer is necessary for the reconstruction of the states above the open charm threshold with a small energy released in a decay (as for example the $D^* \to D^0\pi$, see **Fig 4.32**) and hyperon production with highly anisotropic angular distribution (**Fig 4.35**). Such reactions are also important for the measurement of electromagnetic transition form-factors of hyperons, as it will be discussed in the next section.

4.6 Study of the Λ(1520) → Λ^0 e^+ e^- channel

4.6.1 Reaction and background simulation

To study the possibility of such a measurement with the PANDA spectrometer, a simulation has been performed with the PandaROOT framework [81]. Two channels have been selected for the simulation separately:

- $\bar{p} - p \rightarrow \Lambda(1520)\bar{\Lambda}(1520)(stable) \rightarrow \bar{\Lambda}(1520)\Lambda^0 e^+ e^- \rightarrow \bar{\Lambda}(1520) e^+ e^- \pi^-$p
- $\bar{p} - p \rightarrow \Lambda(1520)\bar{\Lambda}(1520)(stable) \rightarrow \bar{\Lambda}(1520)\Lambda^0 \pi^+ \pi^- \rightarrow \bar{\Lambda}(1520) \pi^+ \pi^- \pi^-$p

In the simulations one of the hyperons was not decayed (assumed "stable") since for the final state identification and reconstruction only one hyperon is sufficient. The momentum of the anti-proton beam is set to 4 GeV/c. The first channel is the main point of interest for this study, the second one is acting as the main source of the background in the signal. The angular distributions of the reaction products have been assumed isotropic in the available phase space.

	Mode	Fraction (Γ_i/Γ)
Γ_1	$N\overline{K}$	45 ± 1%
Γ_2	$\Sigma\pi$	42 ± 1%
Γ_3	$\Lambda\pi\pi$	10 ± 1%
Γ_4	$\Sigma(1385)\pi$	
Γ_5	$\Sigma(1385)\pi(\rightarrow \Lambda\pi\pi)$	
Γ_6	$\Lambda(\pi\pi)_{S\text{-wave}}$	
Γ_7	$\Sigma\pi\pi$	0.9 ± 0.1%
Γ_8	$\Lambda\gamma$	0.85 ± 0.15%
Γ_9	$\Sigma^0\gamma$	

Table 1. 9 Observed possible decay modes for Λ(1520).

As the background channel the $\Lambda^0\pi^+\pi^-$ decay of Λ (1520) with 10% branching ratio has been selected. It presents the most dominant background channel because it contains a Λ^0 and two pions which can be misidentified with electron-positron pair appearing in the $\Lambda^0 e^+ e^-$ final state with much lower branching ratio of $6.8 \cdot 10^{-5}$. The latter one has been estimated from the known Λγ branching ratio. Λ(1520) decay modes are presented in **Table 1.9**.

The results of the simulations are presented in **Fig 4.36** (background) and **Fig 4.37** (signal), showing the distributions of the polar emission angles vs the momentum for various particles species in the full solid angle. The same distributions but after reconstruction are shown in **Fig 4.38**, the respective reconstruction efficiencies are summarized in **Table 1.10**. It is important to note that the reconstructed spectra and the reconstruction efficiency values for particles and anti-particles are symmetric (see **Fig 4.38** top panel and **Table 1.10**). This shows that the spectrometer works properly.

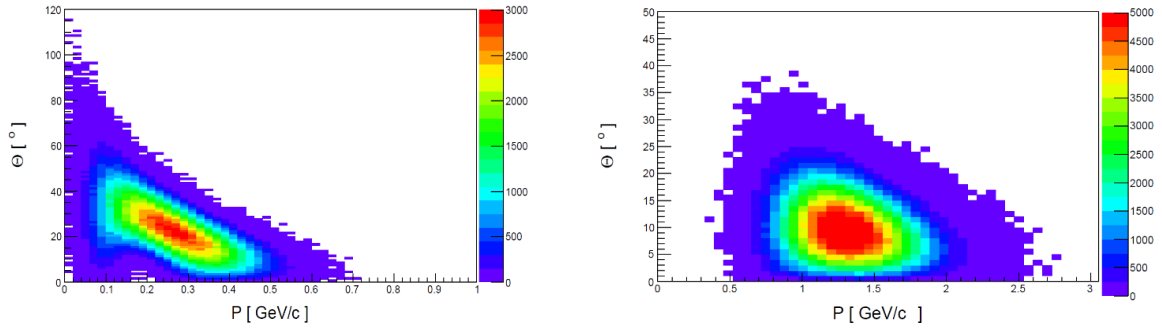

Fig 4.36 Distributions of the polar emission angles vs the momentum for π^-/π^+ (left) and proton/anti-proton (right) from the Λ(1520) decay.

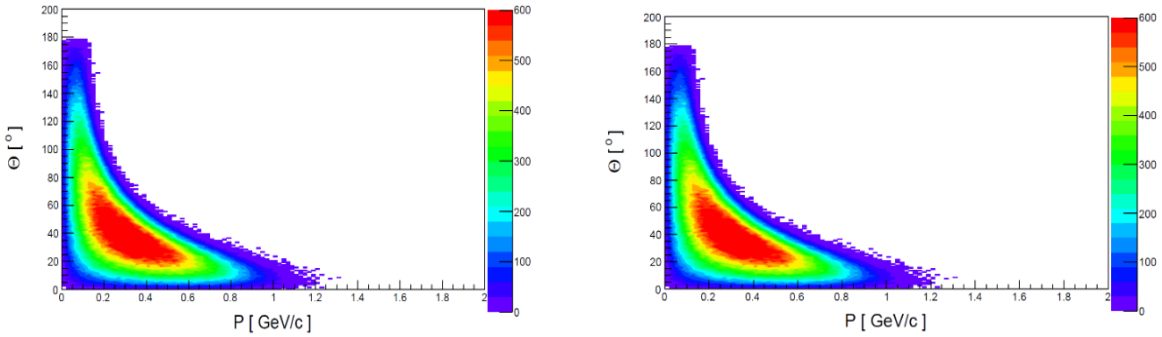

Fig 4.37 Distributions of the polar emission angles vs the momentum for e^+ (left) and e^- (right) from the Λ(1520) decay.

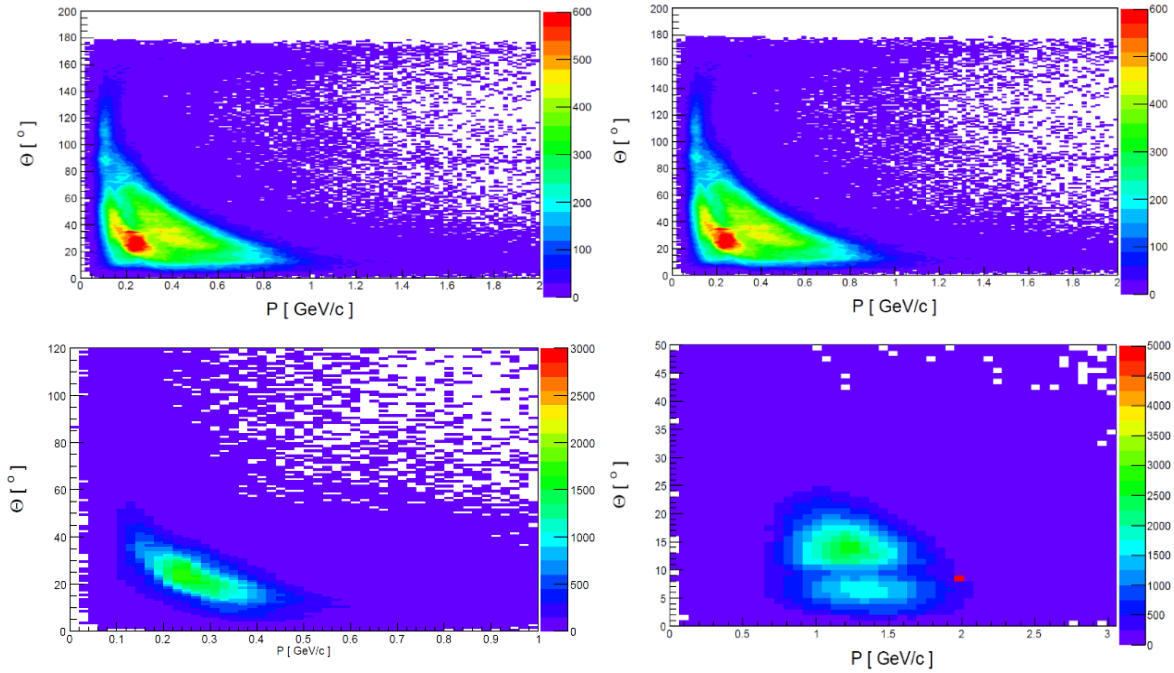

Fig 4.38 Distributions of the polar emission angles vs the momentum for the reconstructed, e^+ (left) and e^- (right) -top panel, and π^-/π^+ (left) and proton/anti-proton (right)-bottom panel.

Particle	Reconstructed [%]
e+/e-	71%
π+/π-	47%
$p/\bar{p}$	49%

Table 1.10 Reconstruction efficiencies of the selected particles from the Λ(1520) decays (see text for more details).

To study the effect of the background coming from the $\Lambda(1520) \rightarrow \Lambda^0\pi^+\pi^-$ and the pions being misidentified as electrons, an emulation of the Particle Identification based on tabularized response of the various PANDA detectors has been performed, as described below.

4.6.2 The global Particle Identification (PID) method

The global PID [83], which combines the information of all sub detectors associated with the reconstruction of one track, has been performed with an likelihood method. Based on the likelihoods obtained from each sub-detector the probability for a track originating from a specific particle type p(k) is calculated from the likelihoods as follows:

$$p(k) = \frac{\prod_i p_i(k)}{\sum_j \prod_i p_i(j)} \qquad (25)$$

where the product with index "i" iterates over all selected sub-detectors and the sum with index "j" over the particle types e, μ, π, K and p. **Fig 4.39** presents the distribution of the efficiency for electron identification as a function of the momentum and the emission angle for the probability for a track to be an electron calculated with equation 25, is larger than 0.5 (left) or 0.8 (right). The following set of detectors with the respective particle separation powers is included in the analysis:

- Straw Tube Tracker (STT) (see **Fig 4.14**)
- Micro Vertex Detector (MVD) (see **Fig 4.21**)
- Barrel DIRC (see **Fig 4.17**)
- Disc DIRC (see **Fig 4.19**)
- Electromagnetic Calorimeter (see **Fig 4.25**)

The particle identification capability of the specific sub-detectors have been already addressed in section **4.4**. For the reconstruction of the Λ(1520) decay especially important is the possibly to separate electrons form pions.

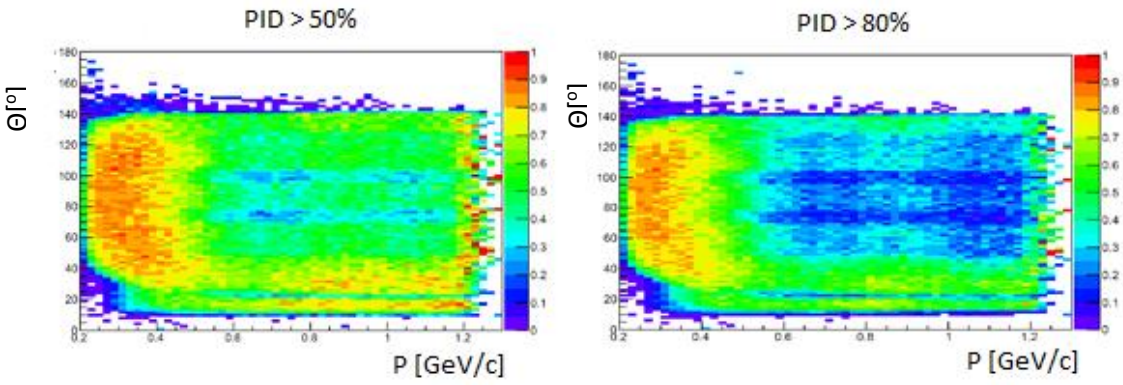

Fig 4.39 Efficiency of an electron identification as a function of the momentum and the emission angle. A cut on the probability for a track being identified as an electron, larger than 50% (left) and 80% (right).

In the first step the Λ^0 has been reconstructed by combining a proton and π^- in the same event.

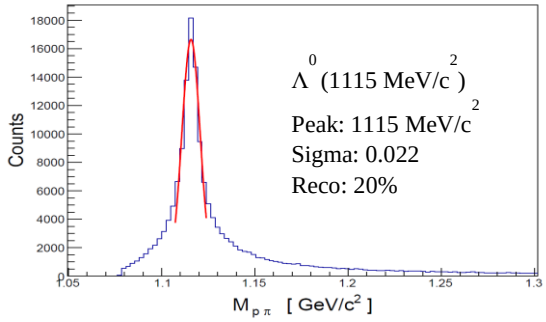

Fig 4.40 Reconstructed Λ^0 mass distributions, reconstruction efficiency is 20%.

Fig 4.40 shows the reconstructed invariant mass of the Λ^0, the peak in the spectrum was fitted by a Gaussian function (red curve). Peak position is consistent with respect to the known PDG values [99]. To perform the reconstruction of the $\Lambda^0(1520)$ the reconstructed four vector of the Λ^0 has been combined with a reconstructed four vector of a pair of electron/positron from the same event.

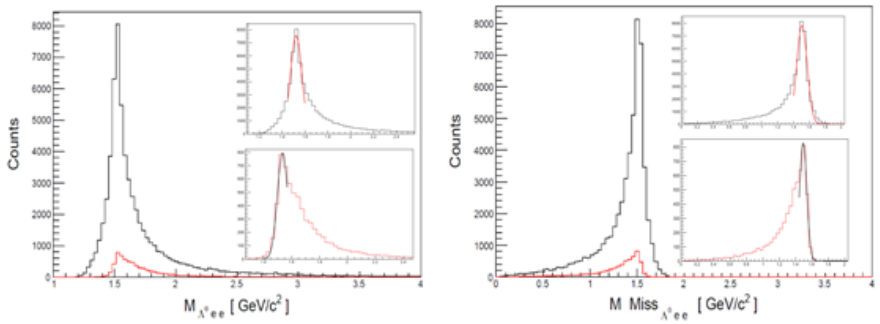

Fig 4.41 The reconstructed $\Lambda(1520)$ invariant mass and the missing mass ($\bar{\Lambda}(1520)$) (black curve), the same distributions but filtered with the PID efficiency matrix (see **Fig 4.39**) (red curve). The small canvases show the same distributions but fitted with Gaussian functions represented by a red and black curves. (for results see text)

particle	peak position	sigma	Fraction form 4π
Λ(1520) Reconstructed	1.522	0.05	7%
Λ(1520) reconstructed & filtered by PID	1.539	0.049	0.7%

Table 1.11 Reconstruction efficiency, peak position and sigma obtained from a fit of the $\Lambda(1520) \rightarrow \Lambda^0 e^+ e^-$ invariant mass reconstructed and reconstructed and filtered with efficiency.

Fig 4.41 shows a distribution of the resulting invariant mass of the Λ(1520) (left) and the missing mas (right) (black solid curve). The distributions are compared to the ones filtered by the efficiency matrix of the PID calculated for 50% probability for a track being and electron/positron (called later 50% electron PID cut) (see **Fig 4.39** -left) shown by red solid curves. The small canvases shows the same distributions but fitted with Gaussian functions. The results of the fit, and the reconstruction efficiencies for both cases are presented in **Table 1.11**. The distributions of the invariant mass shown in **Fig 4.41** has a significant tails due to energy loss of electrons which is not properly corrected for by the Tracking algorithm (Kalman Filter). The Gaussian fit gives therefore only some estimation of the peak position. The total reconstruction efficiency is 7% (see **Table 1.11**) which is quite low, but one has to keep in mind that it is a four particle final state. One should note that, the total reconstruction efficiency drops by a factor of 10 when the PID efficiency is included. What is important to notice is the that shapes of the distribution filtered by the efficiency matrix (red line) is different from the reconstructed one (black line) which is due to dependence of the efficiency on the electron/positron momentum.

The major goal of this study is to obtain an undistorted shape of the invariant mass of the pair of a positron and an electron, which is sensitive to contributions of the vector mesons (discussed in **4.2**). For this purpose the invariant mass spectra of e^+e^- coming from the Λ(1520) Dalitz decay were examined. The distributions are presented in **Fig 4.42** for the two cases: reconstructed (black curve) and reconstructed and filtered with the PID efficiency matrix (red curve). The left plot shows the distributions of the e^+e^- invariant mass, the right plot shows a similar distribution but plotted with a condition on the reconstructed Λ(1520) invariant mass (from 1.5 GeV/c^2 to 1.67 GeV/c^2).

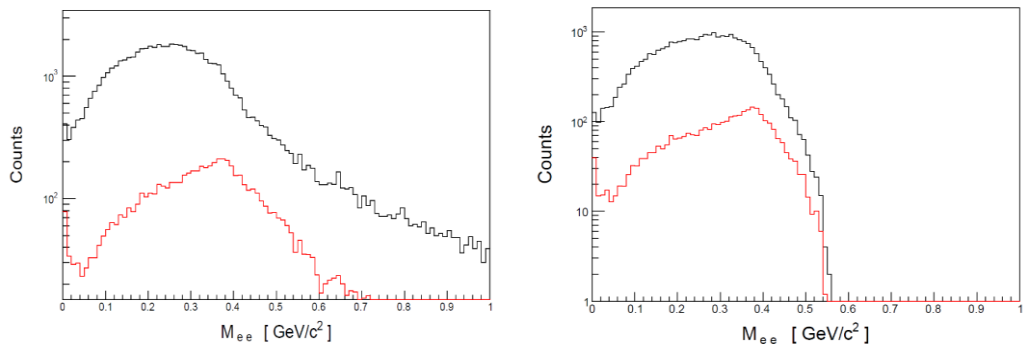

Fig 4.42 $\Lambda^0 e^+ e^-$ final state. Distributions of a e^+e^- invariant mass for the reconstructed electron/positron pairs (black curve) and reconstructed and filtered by the PID efficiency matrices (red curve). The left canvas presents a similar distribution but within the condition on the Λ(1520) invariant mass.

The e^+e^- invariant mass in **Fig 4.42** shows a significant "tail" effect which tail originates from the bremsstrahlung losses appearing when electron is traversing the detector material. Hence, a selection window applied on the Λ(1520) invariant mass (from 1.5 GeV/c^2 to 1.67 GeV/c^2) has been found to be necessary, to reduce this background process.

$\Lambda(1520)\rightarrow\Lambda^0e^+e^-$	Efficiency
Signal reconstructed	2.62%
Signal reconstructed & and filtered by PID	0.33%

Table 1.12 Reconstruction efficiency for the $\Lambda(1520)\rightarrow\Lambda^0e^+e^-$ within the one dimensional mass cut.

Table 1.12 summarizes the respective reconstruction efficiencies. One can see that the effect of PID selections reduce the total reconstruction efficiency by almost order of magnitude. However, such tight selection is needed to reduce the hadronic background with much larger production probability.

The goal of this analysis is to investigate the signal (electron/position pair invariant mass) in terms of the reconstruction efficiency, and the influence of the background coming from the pions misidentified as the electrons. This effect can be a severe problem due to the fact the branching ratio for the hadronic decay is large (~10%) in comparison to the theoretically calculated ratio for leptons ~10^{-5}. Therefore, besides the electron identification PID efficiency one has to calculate also the misidentification of pions as electrons for the two PID electron cuts 50% and 80%, discussed above. The respective maps are presented below.

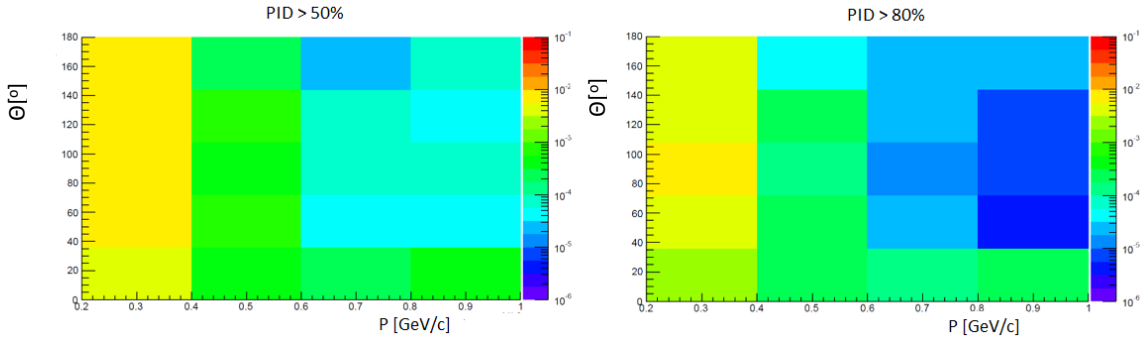

Fig 4.43 Misidentification of the pion being identified as an electron as a function of the momentum and the emission angle for the electron PID cut 50% (left) and 80% (right).

Fig 4.43 presents the respective misidentification in the situation when a pion is misidentified as an electron. The maps have been done in a two-dimensional representation: a polar angle in a function of the momentum. The required electron identification probability has been set to 50% (left) and 80% (right).

To estimate contribution of the background reconstruction of the hadronic channel has extended by the PID electron selection. For this purpose the reconstructed pion tracks have been filtered through the PID misidentification matrix shown in **Fig 4.44**. Comparison of the resulting invariant (left) and the missing mass (right) distributions are shown in

Fig 4.44 for the signal (black) and background (red). Both channels have been simulated with the same number of events. The visible reduction of the background is due to the tight electron PID cut (50%) ($\Lambda(1520)\rightarrow\Lambda^0e^+e^-$ presented by black curve) electron/positron identification PID > 50% (see **Fig 4.39** left) and for the hadronic channel ($\Lambda^0\pi^+\pi^-$ presented by red curve **Fig 4.43** left).

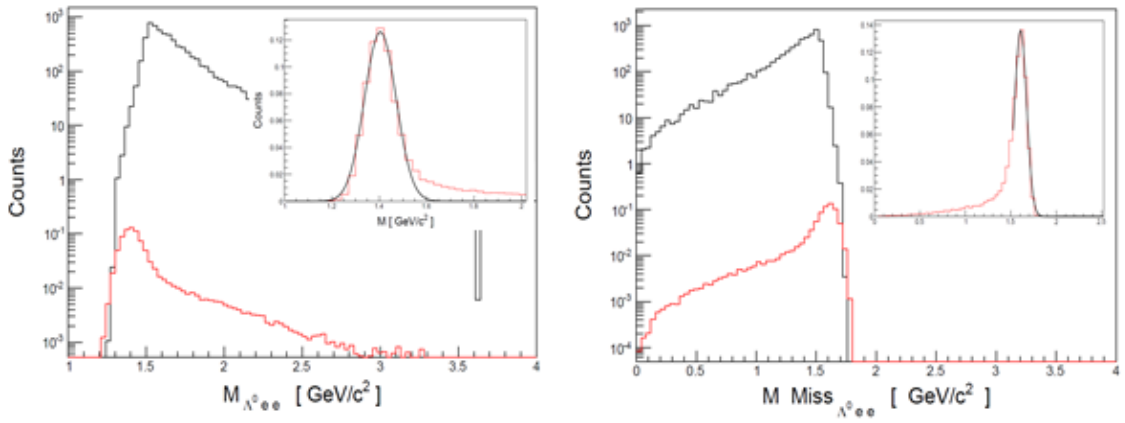

Fig 4.44 $\Lambda^0e^+e^-$ final state. Invariant mass of $\Lambda(1520)$ and the missing mass distributions. The leptonic decay ($(\Lambda(1520)\rightarrow\Lambda^0e^+e^-$) (black curve) and the hadronic ($(\Lambda(1520)\rightarrow\Lambda^0\pi^+\pi^-$) (red curve) all filtered with respective PID matrices (PID > 50%).

The small canvases in both plots (left and right) show the same invariant mass (left) and missing mass (right) fitted with a Gaussian function (black curve). Fit results and reconstruction efficiencies are shown in **Table 1.13**. The distributions of the $\Lambda(1520)$ invariant and missing mass in **Fig 4.44** differ booth in yield and the peak position (see **Table 1.13**). As mentioned above (page 88-89), a selection window is applied on the $\Lambda(1520)$ invariant mass and it is expected that this will remove a lot of contribution coming from the hadronic background ($\Lambda^0\pi^+\pi^-$) as well, the peak in the hadronic channel (red curve) is shifted to a lower mass (~1.4 GeV/c^2 see also **Table 1.13**). The green lines represent the selected range in **Fig 4.45**, showing again the invariants mass (left) and the missing mass distributions (right) within the one dimensional cut imposed on the invariant mas (green lines).

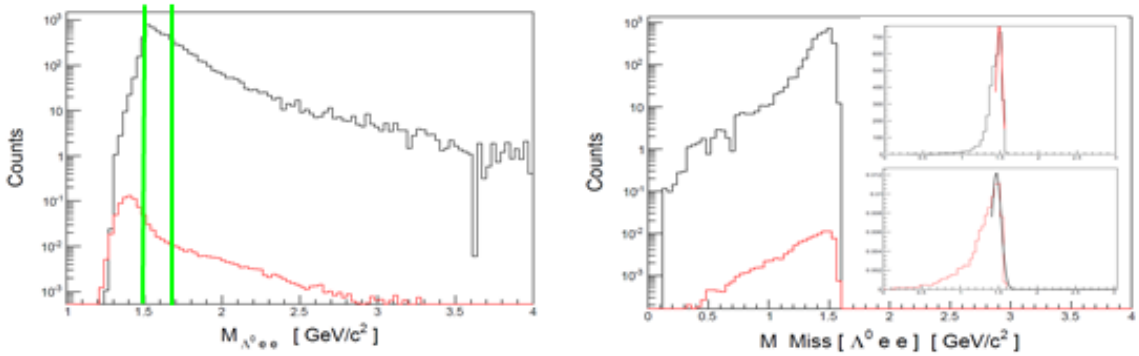

Fig 4.45 Reconstruction of $\Lambda^0e^+e^-$ final state including PID selections on electrons (black) and $\Lambda^0\pi^+\pi^-$ (red). A graphical presentation (green lines) of the selection window set on the $\Lambda(1520)$ invariant mass (left) and missing mass calculated within the cut (right).

Decay channel	Peak position	sigma	Reconstruction efficiency
$\Lambda(1520)\rightarrow\Lambda^0e^+e^-$	1.508	0.060	2.62%
$\Lambda(1520)\rightarrow\Lambda^0\pi^+\pi^-$	1.49	0.23	0.0015%

Table 1.13 Peak positions in the invariant mass of $\Lambda^0e^+e^-$ ($\pi^+\pi^-$) and the reconstruction efficiencies (including the PID) for the leptonic and hadronic channel.

The selection window on the invariant mass is very useful for reducing the background contribution form $\Lambda^0\pi^+\pi^-$, the total reduction factor is in the order of 10^{-4} ~10^{-5}.

4.6.3 Signal to background and production rate study

At this point it is possible to proceed to the final calculations. The differential decay width of the $\Lambda(1520)\rightarrow\Lambda^0e^+e^-$ has been parametrized according to the "QED" prescription described in [72] and scaled by the expected branching ratio (see **Table 1.14**). The hadronic decay has been scaled to the know branching ratio of 10%. The PID efficiencies are defined by 50% (left) and 80% (right) electron identification and PID cut.

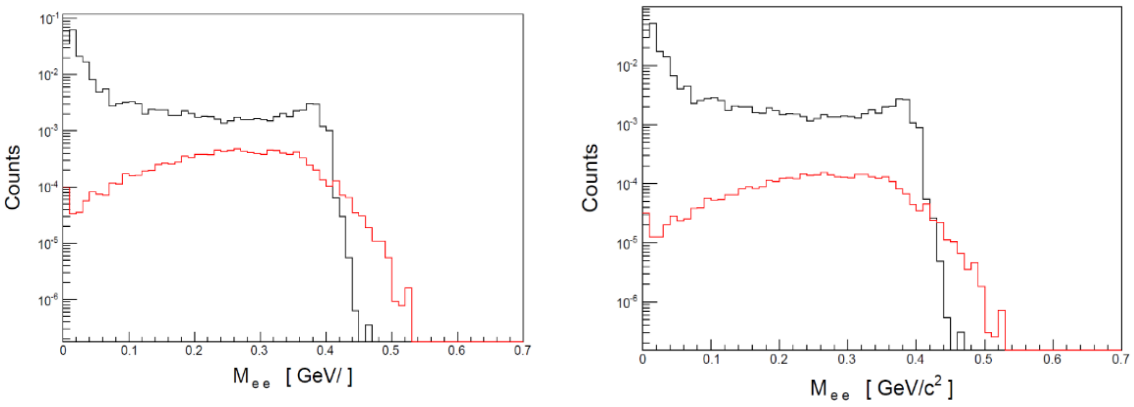

Fig 4.46 $\Lambda^0e^+e^-$ final state. e^+e^- invariant mass distributions parametrized with the function presented in [72] (black curve) and scaled to the corresponding branching ratio ($6.8 \cdot 10^{-5}$) compared with the contributions coming from the hadronic decay (red curve) scaled to the 10% branching ratio. Plots done for 50% (left) and 80% (right) efficiency parametrization.

Fig 4.46 shows the invariant mass distributions for e^+e^- pairs (black curve) with the included electron PID cut (50% electron/positron probability cut left and 80% right) compared with the invariant mass distribution obtained for the hadronic channel (red curve) where pions are partially misidentified as electrons. The comparison in shows that the signal (black curve, e^+e^- originating form $\Lambda(1520)$ Dalitz decay) is higher by about a factor 10 in comparison to the hadronic background. Therefore, it seems to be possible to reconstruct the signal with only a small contribution of the background. Using tighter PID cuts (80%, see **Fig 4.46** right) improves the situation but there is a further loss of about 15% of the e^+e^- signal.

The cross section for the Λ(1520) inclusive production has been deduced from [101]. The total cross section in $\bar{p} - p$ for the inclusive $\bar{\Lambda}^0$ production is 200 μb when taking in to account the channels with $\bar{\Lambda}^0\Lambda$ and $\bar{\Lambda}^0\Sigma^0$ (see **Fig 4.** in [101]). Comparing the spectra presented in **Fig 4.47** one can judge the inclusive production cross section for the Λ(1520) is ~30% of the inclusive production cross section for the $\bar{\Lambda}^0$.

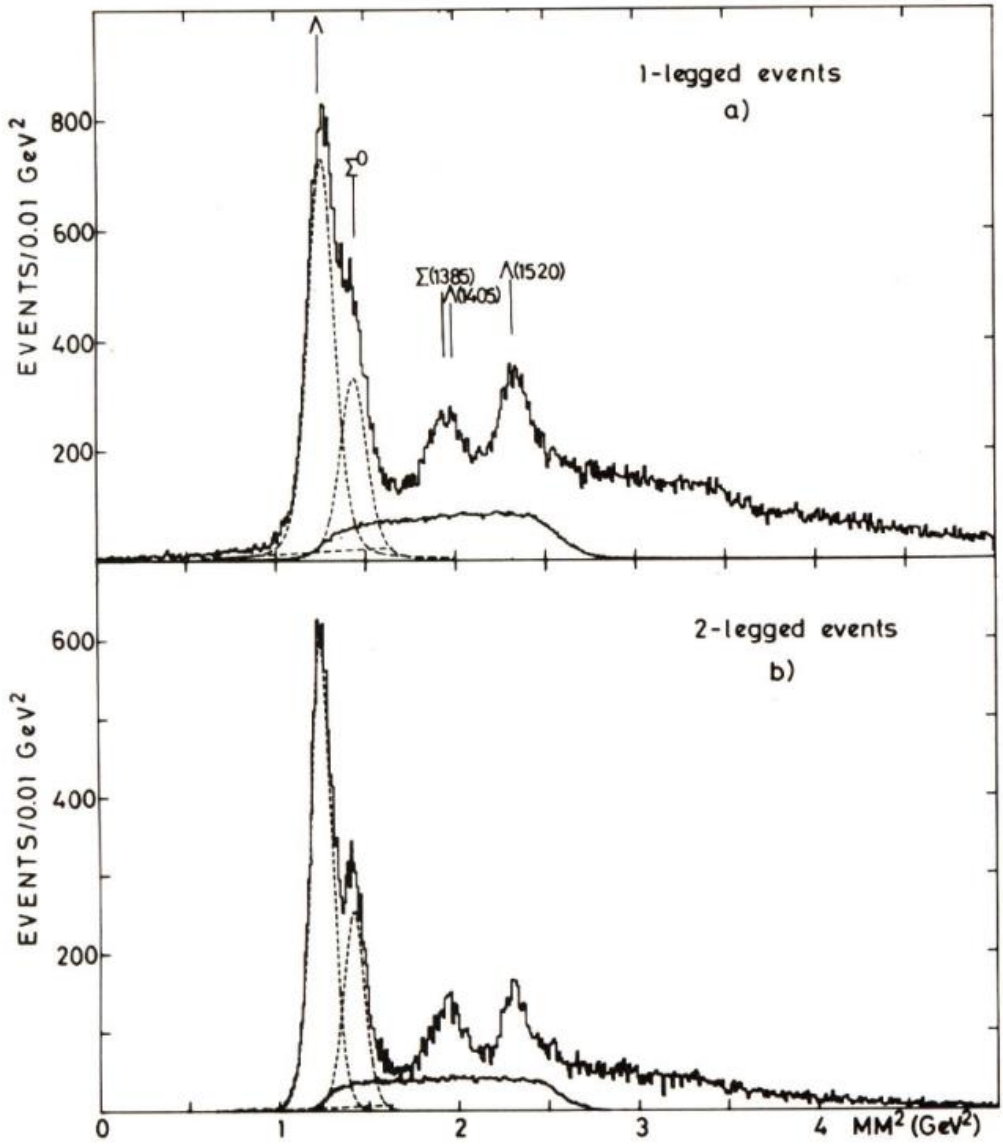

Fig 4.47 Missing mass squared distribution for a) 1- legged evets and b) two legged events. The black dashed curve represents contributions coming form $\bar{p}p \rightarrow \bar{\Lambda}^0\Lambda^0, \bar{p}p \rightarrow \bar{\Lambda}^0\Sigma^0$. The picture is taken form [101].

To conclude the study and present predictions for the future measurement a cross section of 43 μb has been assumed in order to calculate the respective production rates. It is important to notice that the real cross section for this process is not precisely known. The table presented below shows the results for the both luminosity modes and the electron PID cut of 50%.

High luminosity mode	Low luminosity mode
L = 2 *10^{32}/ cm^2 *s	L = 2 *10^{31}/ cm^2 *s
Branching ration 6.8 * 10^{-5}	
σ = 43 μb*	
e+ e- pair reconstruction efficiency (within mass window)	
180 / 24 h	18 / 24 h

Table 1.14 Obtained count rates estimates for the $\Lambda(1520) \rightarrow \Lambda^0 e^+ e^-$ reconstruction in PANDA including efficiency of PID electron cut (50%) Calculations are done for two luminosity modes.

Table 1.14 presents the count rate estimates for the $\Lambda(1520) \rightarrow \Lambda^0 e^+ e^-$ reconstruction. The results for the high luminosity mode are optimistic, a significant advantage of the PANDA spectrometer is the high signal to background ratio in both situations (PID 50% and 80%) leading to a conclusion that the obtained signal will not be distorted by impurities from the pion misidentification.

A similar study has been carried out for the HADES spectrometer using proton-proton reactions and 4.5 GeV kinetic beam energy [85]. The respective count rates estimates are presented in a table below.

	Proton Beam	Pion Beam
HADES only		
Carbon Target	52/day	0.2/day
Hydrogen Target	13.2/day	0.2/day
HADES and FW		
Carbon Target	128.3/day	0.5/day
Hydrogen Target	32.6/day	0.7/day

Table 1.15 Reconstruction efficiency for the HADES spectrometer, the analysis was done for the proton and pion beam, different targets were taken under consideration [85].

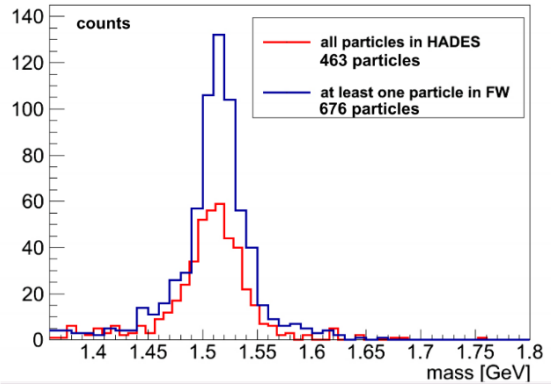

Fig 4. 48 Invariant mas of the Λ(1520) calculated for two scenarios, red curve shows the obtained result for the current HADES setup (discussed in section **2**), the blue curve on the other hand shows results with the included planned Forward Detector (FW).

Table 1.15 shows the reconstruction rates obtained from a similar analysis done for the HADES spectrometer for two scenarios and different targets [85]. **Fig 4.48** shows the invariant mass distribution for the Λ(1520) obtained from particles tagged only in the

HADES spectrometer (red solid), the HADES spectrometer and one particle in the planned Forward Detector (blue solid).

Although the PANDA spectrometer is not a dedicated experiment focused on lepton reconstruction, archived reconstruction efficiencies are similar to ones obtained by the HADES spectrometer (see **Table 1.14** results with FD included see **Fig 4. 48**), but the study done for the PANDA spectrometer does not include yet the FS. The analysis was focused mainly on the central part of the detector (forward part PID functions are not yet included in the simulation package). Simulations done in section **4.5** suggest that inclusion of FS would yield additional acceptance, particularly if $\Lambda(1520)$ production is forward peaked. What is also optimistic is the signal to background ratio of a factor of 10 which points that the PANDA spectrometer can deliver a clear and undistorted signal, this is crucial for the planned study introduced in section **4.2**.

Summary

Part I

In this thesis the results for the quasi-free exclusive pn → pne$^+$e$^-$ channel measured with the HADES detector using a deuterium beam at GSI with a kinetic beam energy T=1.25 GeV/nucleon were shown. The e$^+$e$^-$ mass differential cross section in a function of the invariant mass presents a similar excess with respect to the one measured in the pp → ppe$^+$e$^-$ channel as previously reported in the inclusive e$^+$e$^-$ productions. The excess is due to the baryonic sources related to nucleon-nucleon bremsstrahlung and the Delta resonance Dalitz decay. The detection of the proton provides additional observables (invariant masses, angular distributions) which impose strong constraints on the interpretation of the dielectron excess. Two models, which provided an improved description of the inclusive e$^+$e$^-$ production in the pn reaction, have been confronted with the data. The first one consists of the incoherent sum of dielectron sources including in addition to the π^0, Δ and η Dalitz decays, a contribution from the ρ-meson emission via a double Δ excitation (model of Bashkanov and Clement [32]). The second model derives from the Lagrangian approach by Shyam and Mosel [31] and provides a coherent calculation of the pn → pne$^+$e$^-$ reaction. In both models, the enhancement at large invariant masses is due to an intermediate ρ meson which is introduced for the production of the e$^+$e$^-$ pair from the exchanged of a charged meson. The evolution of the shape of the experimental helicity angle distribution validates the emission via an intermediate virtual ρ at the large invariant masses. Since this process is absent in the reaction pp → ppe$^+$e$^-$, it provides a natural explanation for the observed excess. The different nature of the graphs at the origin of this ρ-meson contribution in the two models is reflected in the pe$^+$e$^-$ and pn invariant masses. A better description of the experimental distributions is obtained with the Shyam and Mosel [31] model, where the effect is related to the nucleon charge exchange graphs. The agreement is also not perfect, pointing to missing contributions. On the other hand, it is clear that the double Δ excitation process is expected to play a role in the e$^+$e$^-$ production. Understanding the e$^+$e$^-$ production in the pn reaction appears indeed as a necessary step towards the description of e$^+$e$^-$ production in heavy-ion collisions where medium effects are investigated. The description of the pn → pne$^+$e$^-$ process is challenging because it implies many graphs with unknown baryon electromagnetic transition form-factors in the time-like region. The exclusive measurement of the quasi-free np → npe$^+$e$^-$ reaction at T=1.25 GeV presented in this thesis is sensitive to the various underlying mechanisms and in particular sheds more light on contributions which are specific to the pn reaction.

Part II

The PANDA experiment will play a key role at the Facility for Antiproton and Ion Research (FAIR) which is under construction in GSI Helmholtzzentrum für Schwerionenforschung in Darmstadt, Germany. The presented calculations based on the simulation within the PandaROOT framework show that the setup fulfils the requirements for the planned physics program. The selected benchmark channels reflecting physics topics addressed in this thesis such as, the Ψ(4040) decay into the double D* mesons, show the importance of the Forward Detector as a necessary component in the planned measurement of states above the open charm production threshold. The $\bar{\Lambda}^0 \rightarrow \bar{p}\pi$ decay mode exhibits the same feature, where both products are forward peaked. A genuine feature of this simulation is the applied measured angular parametrization for such a reaction [82]. This is very important since the angular distribution of the Λ(1520) decay products is expected to be similar. Finally the analysis of the Monte-Carlo simulation of the hyperon Dalitz decay, such as the $\Lambda(1520) \rightarrow \Lambda^0 e^+ e^-$ has been presented. This reaction is connected to the electromagnetic structure of the hyperons, a subject which is an extension of the HADES physics program related to the baryon eTFF. The studies concentrated on signal to background (pion contamination) ratio and production efficiency of lepton pairs (the S/B ratio amounts to 10 – 100 and the production rate is 180 pairs per 24h). Comparison to similar studies performed for the pp reactions by means of HADES has been shown. It demonstrates good capabilities of both detectors for such studies.

The author gratefully acknowledges the support by NCN grant 2013/10/M/ST2/00042 SIP JUC Cracow.

Bibliography:

1. A. Anastasi Phys.Lett. B757 (2016) 362-367
2. R. Arnaldi Phys.Lett. B757 (2016) 437-444
3. Rapp, Hess Eur.Phys.J. A52 (2016) no.8, 257
4. L.G. LANDSBERG "Electromagnetic decays of light mesons" *for* High Energy Physics, Serpukhov, U.S.S.R.
5. B. Pasquini, S. Boffi Phys.Rev.D73:094001,2006
6. Theory of strong interactions, J. J. Sakurai, Ann. Phys., 11 (1960)
7. M. I. Krivoruchenko, A. Faessler, "Remarks on Delta Radiative and Dalitz Decays", Phys.Rev.D65, 2002
8. https://www-hades.gsi.de/?q=node/10
9. G. Eichmann Acta Phys. Pol. B Proc. Suppl. 7 (2014) pp.597-606
10. I. G. Aznauryan and V. D. Burkert, Prog. Part. Nucl. Phys. 67, 1 (2012)
11. I. G.Aznauryuanet al., Int. J. Mod. Phys. E22, 133015(2013)
12. I. G. Aznauryan, V. D. Burkert, the CLAS Collaboration Phys.Rev.C80*:*055203,2009
13. Ian C. et all *Rev. C 90, 045202* (*2014*)
14. G. Ramalho, M. T. Peña, J. Weil, H. van Hees, and U. Mosel Phys. Rev. D 93, 033004 (2016)
15. G. Agakichiev et al. (HADES Collab.), Eur.Phys.J. A48 (2012) 64
16. Daniel Kupelwieser, Wolfgang Schweiger, *arXiv*:*1508.03991*v1
17. "φ Meson production in pp Reactions 3.5 GeV with HADES Detector" M. Palka
18. G. Agakichiev et al., (HADES Collab.), Phys.Rev. C85 (2012) 054005
19. G. Agakichiev et al., Eur. Phys. J. A 50 (2014) 82
20. P. Salabura et al., J.Phys.Conf.Ser. 420 (2013) 012013.
21. G. Agakichiev et al., Phys. Lett. B690 (2010) 118.
22. J. Weil, H. van Hees and U. Mosel, Eur.Phys.J. A48 (2012) 111
23. R. Rapp, J. Wambach, Adv. Nucl. Phys. 25, 1 (2000)
24. W. K. Wilson et al., "Inclusive dielectron cross sections in p+p and p +d interactions at beam energies from 1. 04 to 4.88 GeV ", Phys.Rev.C57: 1865-1878, 199
25. K. Lapidus et al. (HADES Collab.), arXiv:0904.1128
26. M. Lacombe, B. Loiseau, J. M. Richard, R. Vinh Mau et al., "Parametrization of the Paris $N-N$ potential", Phys. Rev. C21, 1980, 861
27. http://www.fz-juelich.de/ikp/COSY-TOF/publikationen/index e.html
28. H. Calen, et al., "Detector setup for a storage ring with an internal target", Nucl.Instrum.Meth.A379:57-75, 1996
29. H. Calen at al., "Measurement of the quasi-free $p\,n \rightarrow p\,n\,\eta$ reaction", Phys. Review C57 (1998) 2667-2670
30. L. P. Kaptari and B. Kampfer, Di-electron bremsstrahlung in intermediate-energy p n and d p collisions, Nucl. Phys. A764 (2006) 338
31. R. Shyam and U. Mosel, Dilepton production in proton-proton and quasifree proton-neutron reactions at 1.25 GeV, Phys. Rev. C82 (2010) 062201
32. M. Bashkanov, H. Clement „On a Possible Explanation of the DLS-Puzzle" Eur.Phys.J. A50 (2014) 107
33. P. Adlarson et al. (WASA-at-COSY Collaboration), Phys. Rev. Lett. 106 (2011) 242302
34. G. Agakichiev et al., "Origin of the low-mass electron pair excess in light nucleus-nucleus collisions" Phys. Lett. B690 (2010) 118.

35. G. Agakichiev et al., Phys.Rev.C 84:014902,2011
36. G. Agakichiev et al., Phys.Rev.Lett. 98 (2007) 052302
37. R.J. Porter et al, PRL 79 (1997) 1229
38. E.L. Bratkovskaya et al. PLB445 (1999) 265
39. Agakishiev et al., PLB 663 (2008) 43
40. G. Agakichiev et al. (HADES Collab.), Eur. Phys. J. A 41 (2009) 243.
41. K. Zeitelhack et al., "The hades rich detector", Nucl. Inst. and Meth., A433:201, 1999
42. C. Muentz et al., "The HADES Tracking System", Nucl. Instrum. Meth., A535:242-246, 2004
43. C. Agodi et al., "The HADES Time-Of-Flight wall", Nucl. Inst. and Meth, A492:14-25, 2002
44. J. Lehnert et al., Nucl.Instrum.Meth. A433 (1999) 268-273
45. R. Trebacz PhD "Investigation of dielectron production in quasi-free $p - n$ scattering at 1.25GeV with HADES"
46. G. Agakichiev et al., "The High-Acceptance Dielectron Spectrometer HADES", Eur.Phys.J. A41:243-277, 2009
47. W.H. Press, Numerical Recipes, 3rd Edition, Cambridge University Press (2007)
48. J. Lehnert et al., "Performance of the HADES ring recognition hardware", Nucl. Instr. Meth. A502 (2003) 261
49. Augustin-Louis Cauchy, "Cours d'analyse de l'École Royale Polytechnique, premier partie, Analyse algébrique", Editrice Clueb Bologna, Paris (1821). and *T. Galatyuk* "Di-electron spectroscopy in HADES and CBM: from p + p and n + p collisions at GSI to Au + Au collisions at FAIR**"**
50. W. Scobel EDDA Collaboration, Nucl.Phys.News 11N4 (2001) 21-26
51. S. Teis at al., "Pion-Production in Heavy-Ion Collisions at SIS energies", Z. Phys. A356 (1997) 421-435
52. I. Froelich et al., J.Phys.Conf.Ser.219:032039,2010
53. P. Moskal at al., "Near-threshold production of the eta meson via the quasi-free $pn \rightarrow pn\eta$ reaction", Phys. Rev. C 79, 015208 (2009)
54. http://geant.cern.ch/
55. E.L. Bratkovskaya, O.V. Teryaev „Anisotropy of Dilepton Emission from NucIear Collisions" Phys.Lett. B348 (1995) 283-289
56. http://www.fair-center.eu/fair-gmbh/eu-project/project-summary.html
57. J.J. Aubert et al. Phys. Rev. Lett. 33 (1974) 1404;
58. PANDA Physics Performance Report, arXiv:0903.3905 and Physics Performance Report for PANDA: Strong Interaction Studies with Antiprotons arXiv:0903.3905 [hep-ex]
59. S.K.Choi et al., Phys. Rev. Lett.91(2003)262001
60. Laura Zotti PhD "Triggerless hybrid pixel detector for the PANDA experiment and benchmark study of a psi(4040) decay"
61. Maiani L, Piccinini F, Polosa AD, Riquer V. Phys. Rev. D 71:014028 (2005)
62. R.L. Jaffe, Phys. Rev. D15, 281 (1977)
63. Ortega et all., Phys.Rev.D81:054023,2010
64. Agnes Lundborg AIP Conf. Proc. 717, 431 (2004)
65. F.-K. Guo, C. Hanhart and U.- G. Meißner, arXiv:0803.1392 [hep-ph].
66. S. Dubynskiy and M.B. Voloshin Phys.Lett.B666:344-346,2008
67. N. Cabibbo and R. Gatto, Phys. Rev. Lett. 4, 313 (1960); Phys. Rev. 124,1577 (1961).

68. S. Dobbs et al., 2014 J. Phys.: Conf. Ser. 556 012009
69. S. Dobbs *et al.* [CLEO Collaboration], Phys. Rev. D 76,112001 (2007).
70. F. Wilczek, "Diquarks as Inspiration and as Objects", in "From Fields to Strings", ed.M. Shifman et al.,World Scientific (Singapore), 2005, vol. 1, p. 77 − 93 [arXiv:hep-ph/0409168]; also A. Selem and F. Wilczek, Proc. Ringberg Workshop on "New Trends in HERA Physics", ed. G. Grindhammer et al., World Scientific (Singapore), 2006, p. 337 − 356; [arXiv:hep-ph/0602128].
71. T. Johansson AIP Conf.Proc. 796 (2005) 95-101
72. M. Zetenyi and G. Wolf Phys.Rev.C67(2003)044002
73. http://arxiv.org/pdf/1307.4537v1.pdf
74. https://panda.gsi.de/oldwww/framework/det_iframe.php?section=Particle%20ID
75. "Technical Design Report for the PANDA Barrel DIRC Detector "
76. https://iopscience.iop.org/article/10.1088/1748-0221/7/01/C01068/pdf
77. http://indico.cern.ch/event/15518/contributions/210901/attachments/166399/234767/poster_rev_6_5.pdf
78. M. Akopov et al., The HERMES Dual-Radiator Ring Imagine Cherenkov Detector, Nucl. Instr. Meth., A479:511-530, 2002
79. PANDA Collaboration, Technical Design Report for the: PANDA Micro Vertex Detector, [arXiv:physics.ins-det:1207.6581v2]
80. https://panda.gsi.de/oldwww/framework/det_iframe.php?section=Forward
81. https://fairroot.gsi.de/
82. Rex L. Tayloe, Ph.D. "A Measurement of the $pp \rightarrow \Lambda\Lambda$ AND $pp \rightarrow \sum^{\circ}\Lambda$ + *c.c.* REACTIONS AT 1.726 GeV/c."
83. Binsong MA "Simulation of electromagnetic channels for PANDA at FAIR"
84. R. Williams et. al. PRC48(1993)1381
85. W. Gawlowski "Evaluation of the production and registration rate of Λ(1520) via $e^{-}e^{+}$ channel"
86. M. Okamoto et al. [CP-PACS Collab.], Phys. Rev. D 65, 094508 (2002).
87. P. Chen, Phys. Rev. D64 , 034509 (2001).
88. X. Liao and T. Manke, arXiv:hep-lat/0210030.
89. "Charged charmonium-like structures and the initial single chiral particle emission mechanism" a talk by Takayuki Matsuki
90. Abulencia D et al. (CDF Collaboration) 2006. "Measurement of the dipion mass spectrum in X(3872)→J/ψπ+π−decays." Phys. Rev. Lett. 96:102002–7
91. Taichi Kawanai, Shoichi Sasaki, Phys. Rev. D 85: 091503(R), 2012
92. "Exotic and Charmonium (-like) states at BESIII" a talk by Peilian Liu
93. R. Williams et. al., Phys.Rev. C48 (1993) 1318-1322
94. Particle Data Group, J. Beringer et al., Phys.Rev. D86 (2012) 010001.
95. "Technical Design Report for PANDA Electromagnetic Calorimeter (EMC)" arXiv:0810.1216 [physics.ins-det]
96. http://www.fair-center.eu/fileadmin/fair/publications_exp/Muon_TDR.pdf
97. J.Pietraszko et. al., NIM A 618 (2010) 121 - 123.
98. F. Dohrmann, et. al., Eur. Phys. J. A 45 (2010) 401
99. http://pdg.lbl.gov/2016/tables/rpp2016-tab-baryons-Lambda.pdf
100. http://pdg.lbl.gov/encoder_listings/m176.pdf
101. H. Becker et. al., Nucl.Phys. B141 (1978) 49-64

List to figures

Part I:

Part II

List of tables

Part I:

Part II: